Scale up and performance enhancement of carbon nanotube/silicon heterojunction solar cell using molybdenum oxide layer

酸化モリブデン層によるカーボンナノチューブ/シリコンヘテロ接合太陽電池 の大面積化と高性能化

October, 2021

Xiaoxu HUANG
黄　暁旭

Scale up and performance enhancement of carbon nanotube/silicon heterojunction solar cell using molybdenum oxide layer

酸化モリブデン層によるカーボンナノチューブ/シリコンヘテロ接合太陽電池 の大面積化と高性能化

October, 2021

Waseda University
Graduate School of Advanced Science and Engineering
Department of Applied Chemistry, Research on Chemical Engineering

Xiaoxu HUANG
黄　晓旭

TABLE OF CONTENTS

Thesis Organization

Solar cell is a device designed to convert solar energy directly into electrical power by the photovoltaic (PV) effect. At present, the crystalline Si (c-Si) solar cells dominate the worldwide PV market owing to their high-power conversion efficiency (PCE, >20%), abundant resources for Si, and superior stability (>20 years). However, manufacturing c-Si solar cells involves high temperature (~900 ℃) diffusion process and toxic boron/phosphorous gas precursor. Carbon nanotube (CNT)/Si heterojunction solar cells have attracted much attention owing to the simple fabrication of heterojunction, which processed by transferring CNT films onto Si substrate at room temperature. This avoids high temperature diffusion processes which are necessary for the traditional c-Si solar cells. However, the CNT/Si heterojunction solar cells have poorer stability and lower power conversion efficiency (PCE) than conventional Si solar cells. Importantly, it is still a challenge to reach industrial production due to the difficulty of scaling up of the active area without decreasing its PCE. In this study, the CNT/Si heterojunction solar cells with designs on the cell structure and the fabrication processes that are compatible with scale up are developed.

Chapter 1 begins with the background of the solar cells, including the type of solar cells and the physical principles of solar cell operation. Then it summarizes the development of the CNT/Si heterojunction solar cells, including previous advancements, current progresses and remaining challenges. And a review of application of MoO_x layer in CNT films and CNT-based devices follows. Finally, the research methods and technical route are proposed for practical fabrication of CNT/Si heterojunction solar cells that integrate simple, quick, and controllable processes including dispersion-filtration-transfer process for CNT layer, introduction of multifunctional MoO_x layer onto CNT films, mask-deposition for metal grid electrode, spin-coating for anti-reflection (AR) layer.

Chapter 2 focuses on coating the CNT films in the CNT/n-Si heterojunction solar cell with MoO_x via simple spin-coating of solution-processable MoO_x precursor. A significant improvement in the performance of the CNT/n-Si solar cell is achieved with the MoO_x layer. The PCE of the cell increased to 10.0% from the pristine value of 7.2%. The MoO_x layer is found to be an efficient p-type dopant for the CNT films in CNT/n-Si solar cell, which results in an increase in charge carrier density of the CNT films for lower series resistance and an improvement in the built-in potential at the CNT/n-Si heterojunction for more efficient separation of electron/hole pairs. The MoO_x layer also serves as an enhancer for the anti-reflection (AR) effect of the MoO_x–CNT layer, which enhances the short-circuit current density of the cell. The device with the MoO_x coating shows considerable stability, maintaining the PCE at 80% of its original value for 1440 h in air without any protective layer. The above experiments are carried out based on the small solar cell (active area of 0.0314 cm^2). For the large-sized solar cell fabrication, it is essential to have a metal grid on the CNT film. But the metal grid directly contacts with n-Si through the pores in the CNT films, which results in severe current leakage in the cell. The MoO_x layer can fill the pores in the CNT films, which is expected to be a blocking layer between the metal grid and n-Si for preventing the current leakage. Therefore, the use of the MoO_x precursor for large active area CNT/n-Si solar cell fabrication is explored. However, a poor PCE value of 1.4% is obtained for the large-sized MoO_x-CNT/n-Si solar cell (active area of 4.0 cm^2) is obtained. This is due to the non-uniform MoO_x layer that is caused by the highly hydrophobic surface of the CNT films, which has limited effect in suppression of current leakage in the cell. Finally, the ethanol solution is explored to improve the wettability of MoO_x precursor solution, targeting uniform MoO_x layer on large area CNT films. However, the ethanol is found to be so poor to fully hydrolyze the MoO_x precursor into MoO_x.

Chapter 3 is about the development of a rapid vapor deposition of MoO_x layer for CNT films in the CNT/n-Si solar cell, targeting more uniform deposition of MoO_x layer on the CNT films directly. Here, the MoO_x layer is deposited onto the CNT films in CNT/n-Si heterojunction using a pre-oxidized-Mo boat as a MoO_x source for vapor deposition. The MoO_x layer enhances the PCE significantly from 7.1% to 11.1% for a small-sized solar cell (active area of 0.0314 cm^2) owing to p-type doping of the CNT films and the enhanced AR effect of the MoO_x–CNT layer. As-deposited MoO_x layer serves as a more efficient blocking layer between the metal grid and CNT/n-Si interface than that by the solution method owing to the improved uniformity of the MoO_x layer on the CNT films. A PCE of 3.6% is achieved for a large-sized MoO_x–CNT/n-Si solar cell (active area of 4.0 cm^2). The rate of MoO_x deposition via rapid vapor deposition is analyzed and it is found that this method is too quick to control the MoO_x thickness carefully in the batch process. But in future, this problem will be solved by integrating the rapid vapor deposition of MoO_x layer with roll-to-roll technology, where the MoO_x thickness will be accurately controlled by the sample carrying speed.

Chapter 4 reports an improved method for the vapor deposition of MoO_x on the CNT films. The MoO_x layer is deposited onto the CNT films in CNT/n-Si heterojunction using a Mo wire via a hot-wire oxidation-sublimation deposition method, which is processed by resistively heating the Mo wire under an oxygen-rich gas mixture at low pressure. This method is simple and controllable. As-deposited MoO_x as a multifunctional layer that enables the size and performance enhancement of solar cells are reported. A 4 cm^2-sized MoO_x–CNT/n-Si solar cell with a PCE of 10.0% is realized by the combination of the multifunctional MoO_x layer with a Ag grid electrode. The MoO_x layer plays an essential role as a blocking layer to prevent direct contact and current leakage between Ag and n-Si. It also serves as a p-type dopant for the CNT film, which enhances the electrical conduction and separation of electron–hole pairs at the

heterojunction, and as an enhancer for the AR effect of the MoO_x–CNT layer. Post-thermally annealing of MoO_x is found to be crucially important, and the role of MoO_x is discussed.

Chapter 5 compares the three processes for MoO_x deposition and the resulting MoO_x structures on PV performance of MoO_x–CNT/n-Si solar cells. Although all devices have almost similar PCE in the small sized solar cells, the dry process is better in the scalability. Then, the conclusion of the thesis is summarized. This thesis discusses the scale-up and performance enhancement of the CNT/n-Si heterojunction solar cells using the MoO_x layer. It adopts three methods for MoO_x layer to achieve this goal. They include the simple spin-coating of MoO_x precursor solution, the rapid vapor deposition (<1 min) using a pre-oxidized Mo boat as the source, and the hot-wire oxidation-sublimation deposition using a Mo wire as the source. A 4 cm^2-sized PMMA–MoO_x–CNT/n-Si solar cell with a PCE of 10.0% is realized by optimizing the process conditions and the solar cell structures. A maximum PCE of about 12% would be expected by simply decreasing the shadow of the grid electrode. Finally, a perspective of plan is presented. The previously developed rapid vapor deposition of 10 μm-thick crystalline Si film will be integrated with the cell structure and fabrication technologies developed in this thesis toward the future flexible Si heterojunction solar cells of high performance/cost ratio.

Chapter 1 Introduction

1.1 Solar cells

1.1.1 Solar cells and Si solar cells

Solar cell is an electrical device designed to convert the solar energy into electricity power directly by photovoltaic (PV) effect [1]. They have some advantages including the minimal operating cost and no CO_2 emission during electric power generation. More importantly, the PV technologies helps the electrification of remote places. Basing on the semiconducting material they are made of, the solar cells can be typically classified into multi-crystalline or mono-crystalline Si (c-Si) solar cells, cadmium telluride (CdTe) thin film solar cells, copper indium gallium selenide (CIGS) solar cells, amorphous silicon (a-Si) solar cells, dye-sensitized solar cells, organic solar cells, perovskite solar cells and other emerging solar cells [1]. At present, Si solar cells dominate the worldwide PV market owing to their high-power conversion efficiency (PCE) (>20%), abundant resources for Si and superior stability (>20 years). However, manufacturing of c-Si solar cells is currently performed via the high temperature (~900 °C) diffusion process and using toxic boron/phosphorous gas precursor for fabrication of junction [2–3]. Si heterojunction (SHJ) solar cells have been developed using hydrogenated amorphous silicon (a-Si:H) that can be fabricated at lower temperature, still using toxic gases [4].

1.1.2 Physical principles of the solar cell operation

The most known solar cell is the p-n junction solar cell that is constructed from a semiconductor material doped in p- and n-types. Two photovoltaic properties are important: voltage and electric current generated in a device when it is exposed to light. The physical

principle operating of the solar cell is generation of voltage or electric current between two semiconducting materials when exposed to light [1]. As illustrated in Fig. 1.1, the photovoltaic energy conversion in solar cell involves two important steps. The semiconductor absorbs photons firstly and generates hole-electron pairs when light illuminates the solar cell. Then, the generated hole-electron pairs diffuse and separated by a built-in electric field E at the p–n junction, where the electron moves to the n-region and hole moves to p-region, thus, generating electric current in external circuit [1].

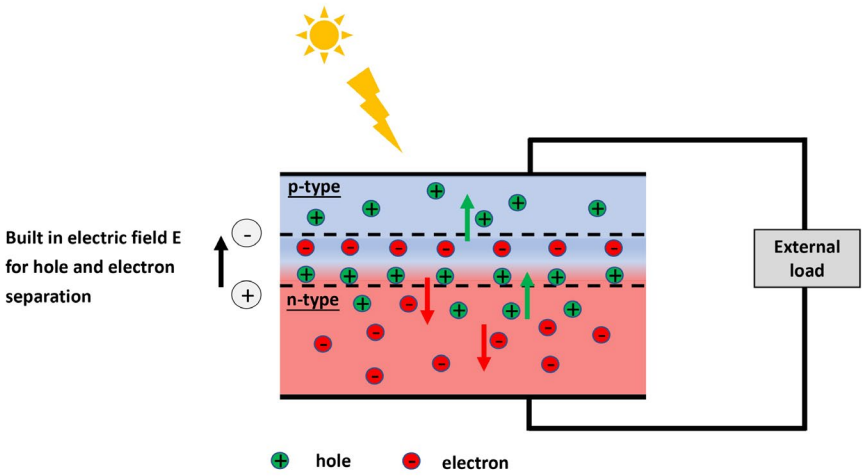

Fig. 1.1 Schematic of physical operating principles of the p-n junction solar cell

The primary parameters of a solar cell are the open-circuit voltage (V_{oc}), the short-circuit current density (I_{sc}), the fill factor (FF) and the power conversion efficiency (PCE) (η). A brief overview of the model relevant to solar cell parameters is provided here. An ideal solar cell can be expressed by an equivalent circuit model. The ideal current source is in proportion to the photo flux when the device is exposed to sun light. There are two conditions for the solar cells and its equivalent circuit: the I_{sc} is the current that flows when the terminals are short-circuited and the V_{oc} is the voltage that appears across the terminals when the leads are left open. The relative I-V characteristic (Fig.1.2) is provided by equation (1) below [1]:

$$I = I_{ph} - I_0\left(e^{\frac{qV}{kT}} - 1\right), \qquad (1)$$

Where k is the Boltzmann constant, T is the absolute temperature, q is the electron charge, and V is the voltage at the terminals of the solar cell. I_0 is the diode saturation current (a solar cell in the dark is simply a semiconductor current rectifier or diode). The I_{ph} is the photogenerated current, which is closely associated with the photo flux incident on the solar cell and its absorbance dependences on the wavelength of light.

For an ideal solar cell, the I_{sc} is equal to the photogenerated current I_{ph}. The V_{oc} is determined by equation (2) below:

$$V_{oc} = \frac{kT}{q}\ln(1 + \frac{I_{ph}}{I_0}) \qquad (2)$$

The maximum power P_{max} of the solar cell is produced at a voltage V_m and current I_m (Fig. 1.2), and it is used to define the FF:

$$FF = \frac{I_m V_m}{I_{sc} V_{oc}} = \frac{P_{max}}{I_{sc} V_{oc}} \qquad (3)$$

The power conversion efficiency η of solar cell is a most commonly used parameter to evaluate the PV performance of solar cell, that is defined as the ratio of power output from the solar cell to input power from the sun. And it is defined by equation (4) below:

$$\eta = \frac{P_{max}}{P_{sun}} = \frac{I_{sc} \times V_{oc} \times FF}{P_{sun}}, \qquad (4)$$

Where P_{sun} is the input power from the sun. And the input power for efficiency calculations is 1 kW/m^2 or 100 mW/cm^2 under air mass (AM1.5) solar spectrum [1].

To improve the solar cell efficiency, considering the parameters discussed above, it is important to increase the carrier concentration for the enhanced light absorption and the current production and to increase the built-in potential for the enhanced separation of the hole-electron pairs.

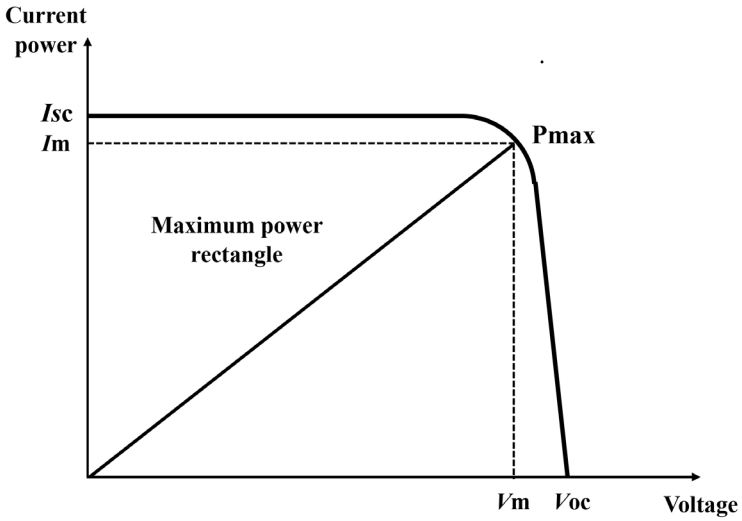

Fig. 1.2 *I-V* characteristic of solar cell.

1.1.3 Limitation of PCE of silicon solar cells

Silicon is an ideal photovoltaic material for solar cells fabrication. It is not only an abundant element in the earth but also an elemental semiconductor whose bandgap (1.12 eV) well matches the solar spectrum. Referring to the parameters discussed above, an important consideration in the improvement of PCE includes the increase of the carrier concentration and the light produced current for higher I_{sc}; the increase in built-in potential that enhances the separation ability of the hole-electron pairs for higher V_{oc}; the reduction of series resistance of cell for high FF. The theoretical limit for the PCE of c-Si solar cell is found to be 30% that can be calculated from the optical absorption edge at the energy gap of c-Si (1.12 eV) and the air mass (AM1.5) solar spectrum based on the Shockley-Queisser theory [5], where the efficiency is calculated as a function of the energy gap. Based on the reported literature and established knowledge of silicon solar cells, the high efficiency of 20% are already well achieved for practice.

1.2 CNT/Si heterojunction solar cells

1.2.1 CNT and CNT films

The report by Sumio lijima in 1991[6] ignited the extensive research on carbon nanotubes (CNTs) owing to their unique nanostructure and properties including large aspect ratio, highly carried mobility and electrical conductivity [7–12]. There are three main methods to produce CNTs currently. They include arc-discharge [13], laser ablation [14], and chemical vapor deposition (CVD) [15–16]. The individual CNTs have been studied for investigating fundamental properties of CNTs including electronic, transport, optical, and mechanical properties. Application of individual CNTs in devices is yet to be fully realized because of the absence of the scalable fabrication processes with precise structure control on the position and chirality of CNTs. Assembling individual CNTs in the form of random networks provides more practical applications because of the scalable production of uniform CNTs films. Furthermore, the CNTs films will have the collective behavior of the individual tubes with additional properties from the tube-tube interaction, which leads to the CNTs films with excellent electrical properties, extremely high electron/hole mobilities and optoelectronic properties [17]. These properties make CNTs films to be useful in various application, including transparent electrical conductors [18–19], thermal interface materials [20–21], energy storage devices [22–24], and heterojunction solar cells [25–26].

Currently, the CNT films can be fabricated by two processes: the dry printing process and the solution-based process. For the dry printing process, the aerosols of CNTs synthesized via floating catalyst CVD are directly collected as a randomly oriented CNTs films on membrane filters or substrates [27]. This direct deposition method produces film with fewer damages and contamination, leading to high-quality CNTs films [28–29]. The CNTs films with high performance of 84 and 86 Ω/sq at 90% optical transmittance at 550 nm after doping with NO_2

and $AuCl_3$ were reported [30–31], thus are expected to replace indium-tin-oxide (ITO) transparent electrodes. However, the CNTs films deposited on substrates via direct grown method may consist of large amount of residual catalyst and difficulty of precise density control. The solution-based CNTs films have demonstrated wide-spread interest in both academia and industry. The CNTs films are often fabricated by a dispersion-filtration-transfer process [32–35]. The solution-based process has several advantages in terms of its ambient process temperature and its applicability to CNTs powders produced from any methods. More importantly, the solution-based process is more suitable for the industrial process for scalable fabrication of the CNTs films because it can be integrated into conventional and popular roll-to-roll technique. For instance, the fabrication of the large scale optically transparent and electrically conducting CNTs films via simple and fast method by combining CNTs ink with rod-coating technique was reported [36], where the purified CNTs powder was dispersed in water at high concentrations with aid of the surfactants and then rod-coated to form uniform thin films.

1.2.2 Advances and current progresses in CNT/Si heterojunction solar cells

CNT/Si heterojunction solar cells have become a potential alternative technology for the commercialized Si solar cells [25]. The CNT/Si heterojunction solar cells are developed with designs on the c-Si solar cell structure but with simpler structure owing to the CNTs films with multiple functions (as shown in Fig.1.3). These includes a transparent conductive layer for transportation of charge carrier, a contact layer for formation of heterojunction with Si, and an effective hole transporting layer [25]. Moreover, the advantage of this type of solar cells is that the simple fabrication of heterojunction, which can be processed by transferring CNTs films onto Si substrate at room temperature. This avoids high temperature diffusion processes (~900 °C) [26], which are need for conversional c-Si solar cells.

The photovoltaic conversion process in CNT/Si heterojunction solar cells is described below. The incident solar light passes through the semitransparent CNTs films, reaches and is absorbed by the Si substrate, and generates electron-hole pairs. The produced electron-hole pairs diffuse to the CNT/Si heterojunction and are separated by an electric field at this region that is set up owing to the built-in potential between the CNTs films and Si wafer. The carrier transport mechanism of CNT/Si heterojunction solar cells is complex and is not yet fully understood. As discussed in previous works, the CNT/Si heterojunction is either p-n or Schottky junction characteristics [37–38]. And related works indicated that the CNTs films do not contribute to the photovoltaic conversion process and the Si plays more important role in photocurrent-generation processes.

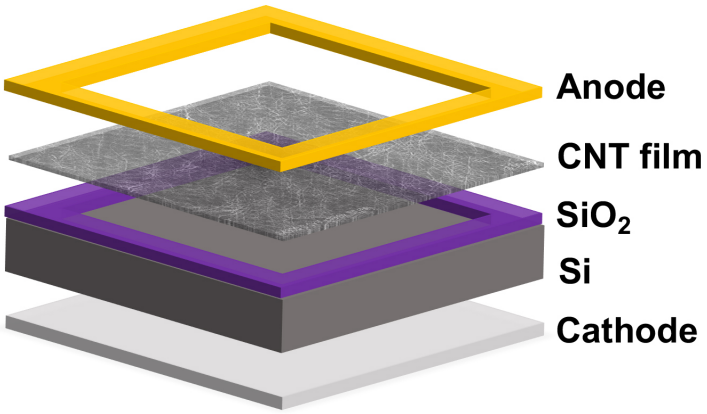

Fig. 1.3 Schematic of the CNT/Si heterojunction solar cell

The CNT/Si heterojunction solar cells were firstly reported in 2007 by Wei and co-workers, with a 1.3% PCE [39]. In Wei's work, the double-walled carbon nanotube (DWNT) films were used for solar cell fabrication. The DWNT films was deposited on n-type silicon (n-Si) substrate via a solution process, by expanding the as-grown DWNT films on water surface and then transferring it onto the n-Si substrate via picking up the floated film from the water with the n-Si wafer. After this report, the PCE of the CNT/Si solar cells have been improved significantly to the range of 4.5%–17%, and 20.1%, as summarized in Table 1.1 [35, 39–52].

These progresses in the CNT/Si heterojunction solar cells have been made by focusing mainly on improving the quality of CNTs films, doping the CNTs films, treatment of the Si surface and addition of anti-reflective coating.

Table 1.1. Summary of literature reports of CNT/Si heterojunction solar cells [35, 39–52].

Year	Active area (cm^2)	PCE (%)	J_{SC} (mA/cm^2)	V_{OC} (V)	FF (-)	Optimization	Ref
2007	0.49	1.3	13.8	0.50	0.19	Double-walled CNT	[39]
2009	0.25	4.5	26.5	0.35	0.49	$SOCl_2$ doping	[40]
2011	0.09	13.8	36.3	0.6	0.72	HNO_3 doping	[41]
2012	-	15.1	32.0	0.61	0.77	TiO_2+ HNO_3 and H_2O_2 doping	[42]
2013	-	11.2	28.6	0.53	0.74	High-quality SWCNT films	[43]
2014	0.09	10.8	29.7	0.54	0.68	Dry transfer CNT films	[44]
2015	0.008	17.0	36.6	0.59	0.78	MoO_x doping	[45]
2016	0.03	10.4	33.1	0.55	0.57	Texture Si	[46]
2017	0.09	14.1	36.1	0.54	0.72	$CuCl_2/Cu(OH)_2$ doping	[47]
2019	0.09	14.4	36.7	0.55	0.71	Nafion doping	[48]
2019	0.03	8.5	26.5	0.55	0.58	Passivation Si wafer	[49]
2019	5	15.1	32.8	0.64	0.73	Nafion + Texture Si+ UV lithography	[50]
2020	16	8.8	34.0	0.6	0.43	Nafion + Texture Si+ Passivation	[51]
2020	245.71	20.1	39.5	0.65	0.79	SiN_x + n^+Si + Texture + Nafion + Back-junction	[52]
2021	0.03	10.2	29.2	0.52	0.67	MoO_x precursor doping	[35]

1.2.3 Remaining challenges for CNT/Si heterojunction solar cells

1.2.3.1 Efficiency and air stability

The efficiency and air stability are two key considerations for solar cells and the CNT/Si heterojunction solar cells are no exception. The pristine CNT/Si heterojunction solar cells show a lower efficiency and a poorer air stability primarily resulting from the nature of CNTs films with porous structure. The CNTs network films cannot form the desirable passivation surface that is essential for the high-quality heterojunction with Si. As a result, the CNT/Si heterojunction solar cells usually show low V_{oc}, leading to low PCE. The oxygen or water reach and oxidize Si surface through the pores in CNT films under ambient air, which results in performance degradation of the device over time.

The carrier doping to the CNTs films is an effective way to enhance the PCE of the CNT/Si heterojunction solar cells, but it also suffers from the doping effect degradation over time. The doping mechanism of CNTs films is that doping can increase the free carrier concentration and reduce the tube-tube junction resistance that allows the carriers more easily move through the CNTs network [53]. There are several useful materials that can dope CNTs films. Acidic liquid dopants are popular that ranges from chloro-sulfonic acid for instance HNO_3 [41], H_2SO_4 [54], $SOCl_2$ [40] to $AuCl_3$ [55]. However, most of them have unstable doping effect in air due to the volatile nature. They also introduce some mobile ions into the CNTs films, which would damage the metal grid electrodes fabricated on top of the CNTs films, thus leads to the performance degradation of the solar cell over time. The CNT/Si solar cells with a record high PCE of 20.1% by integrating various technologies used for the construction of conventional Si solar cells [47] and a record high air stability of about one year (doping with $Cu(OH)_2/CuCl_2$) [52] have been achieved by now. The fabrication of CNT/Si heterojunction solar cells that show high efficiency and long-term stability remains a challenge to explore.

1.2.3.2 Scale up of active area

Until recently, most works are based on small active area (typically in the range of 0.008 to 0.49 cm^2) that is defined by the top metallic electrode of a frame shape. The small active area enables researchers to test various chemical dopants or explore new combinations of materials with CNTs films. However, to meet the practical application, the active area of single solar cells needs to be scaled up to centimeter scale. The PCE degradation with the increase of active area is a common phenomenon in CNT/Si solar cell [56–57]. In commercialized Si-based solar cells, metal grids are applied and deposited on top of the device to efficiently collect charge carriers from the entire device area [58]. However, the metal can penetrate through the CNTs films and reach the Si surface during metal grid deposition because of the loose and porous structure of the CNTs films, which results in severe current leakage in the device. Thus, the fabrication of large-sized CNT/Si solar cell with high efficiency is still a challenging topic to explore. Recently, the CNT/Si solar cell with a PCE of about 10% was realized in active area of 0.49 cm^2 by combining CNT with Ag nanowires and adding TiO_2 layer as an additional antireflection layer, where the Ag nanowires works as grids for the enhanced charge carrier collection [55]. The device with active area of more than 2 cm^2 was reported, in which the CNT strips were used as a replacement of metal grids to avoid the current leakage [59]. The CNT/n-Si solar cells with larger active area of 5, 16, and 245.71 cm^2 with respective PCE of 15.5% [50], 8.8 [51], 20.1 [52], were developed via integrating various technologies applied in the conventional c-Si solar cells. There included the passivating and texturing the Si surface and lithography-based patterning for the contacts and metal grid electrodes. To prevent the metal grid and Si from coming into direct contact, they used the lithographically patterned SiO_2 layer [50], a lithography-less intermixed Nafion-CNT layer that serves also as a passivation, physical blocking and anti-reflective (AR) layer [51], and a Nafion-CNT layer spin-coated on the rear surface that serves also as a hole extraction and passivation layer [52].

1.2.4 Performance outlook of CNT/Si heterojunction solar cells

Table 1.2 lists the main efficiency parameters for CNT/Si heterojunction solar cells including the current best values that have been reported in literatures, and some suggested target values for development in this field. It is predicted that a PCE of 21.6% could be achieved via combining the current best reported values (V_{oc} = 0.66 V, J_{sc} = 39.9 mA/cm^2, FF = 0.82). The target values could be V_{oc} = 0.70 V, J_{sc} = 40 mA/cm^2, and FF = 0.84, that realize a PCE of 23.5%. From the table, while many parameters are already at or near the target values, and there are not any fundamental limitations that prevent CNT/Si heterojunction solar cells from having high PCE. The challenges for the CNT/Si solar cells are in further understanding of the working mechanism of the CNT/Si heterojunction, in improving overall quality of material and fabrication, and in integrating simple, quick and controllable processes into a practical device fabrication process.

Table. 1.2 PV parameters of previously developed CNT/Si solar cells and the limits in their improvement [47, 52, 59]

Parameters	Goal	Target	Best	limit	Ref
V_{oc} [V]	Up	~ 0. 70	0.66	Built-in potential (dominated by work function of CNT films	[52]
J_{sc} [mA/cm^2]	Up	~ 40	39.9	Theoretical max for Egap, Si=42-5% shading by nanotube (90%) films =39	[52]
FF	Up	~ 0.84	0.82	Practical limit around 0.82-0.84 know from silicon cell	[52]
Area [cm^2]	Up	~ 243	245.71	243 (156 mm square wafer)	[52]
Nanotube R_{sheet} [Ω/sq]	Down	< 100	69	Unknow, trade-off with transmittance	[47]
Nanotube T_{550} [%]	Up	> 95	93	< 100, trade-off with resistance	[59]

1.3 Applications of MoO_x layer in CNT films and solar cells.

The MoO_x has wide applications as a useful electronic material owing to ease of deposition from solution or vapor, and their remarkable properties including environmental friendliness, durability, inexpensiveness, low parasitic absorption and high work function [60–61]. There are some reports about the doping of graphene with MoO_x and it had been considered as a weak dopant [62–63]. On the contrary, the MoO_x has been proven to be a strong and stable dopant for CNT films [64–66]. The charge-transfer interaction between MoO_x and CNT network was demonstrated [64], which provides evidence for the stable doping of CNT films by MoO_x. The CNT forests also showed a decrease in resistances after doping by a MoO_x layer [66]. Moreover, doping CNTs films with MoO_x layer as electron-blocking transparent electrodes for highly efficiency flexible organic solar cells was reported [67–69]. A high PCE of about 17% in active area of 0.008 cm^2 of CNT/Si solar cell using MoO_x was also reported [45].

1.4 Research scope and technical route

The potential of CNT/Si heterojunction solar cells for conversion of solar energy to electrical power has attracted much attention. And the CNT/Si heterojunction solar cells can potentially be developed to the level of current high efficiency silicon solar cells. However, the challenges of present insufficient PCE, small active area, and poorer stability need to be solved for their practical application. The small active area is the most core challenge that needs to be solved. Thus, I focus on the scale-up and performance enhancement of CNT/Si heterojunction solar cells using MoO_x layer. The MoO_x layer will expectedly have an essential role as a blocking layer that prevents the metal grid and Si from coming into direct contact and current leakage while allowing the electrical conduction between the top metal grid electrode and CNTs. It also acts as a p-type dopant for the CNTs, which enhanced the electrical conduction and separation of electron–hole pairs at the heterojunction, and as an enhancer for the anti-reflective effect of

the MoO_x–CNT layer. The research objectives include: (1) development of a simple, quick, and controllable process to introduce the MoO_x onto CNTs films, targeting large area uniform MoO_x layer for large-area CNTs films; (2) scalable fabrication of high-efficiency CNT/Si heterojunction solar cells via combination of prepared MoO_x layer with CNTs films. The detail of technical route illustrated in Fig. 1.4 includes: (1) dispersion-filtration-transfer process for CNTs films; (2) introduction of multifunctional MoO_x layer onto the CNT films in the CNT/n-Si solar cell; (3) mask-deposition of Ag top grid electrodes; (4) spin-coating of additional anti-reflective (AR) layer.

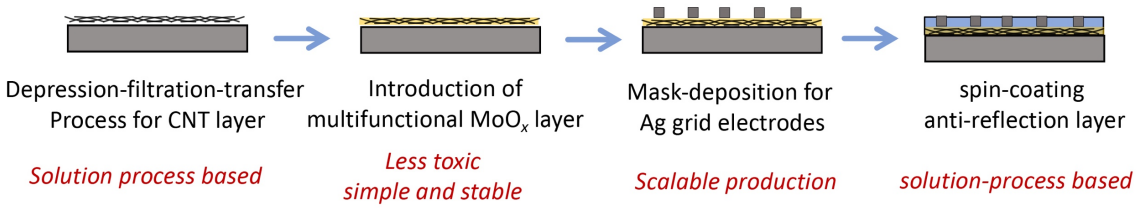

Fig. 1.4 Schematic of the technical route for fabrication of large-sized and high-performance CNT/n-Si heterojunction solar cells using the MoO_x layer.

References

[1] McEvoy A, C. L., Markvart T. , Solar Cells: Materials, Manufacture and Operation, 2nd Edition. *Solar Cells: Materials, Manufacture and Operation, 2nd Edition* **2013**, 1–641.

[2] Ranjan, S.; Balaji, S.; Panella, R. A.; Ydstie, B. E., Silicon solar cell production. *Comput Chem Eng* **2011,** *35*, 1439–1453.

[3] Allen, T. G.; Bullock, J.; Yang, X. B.; Javey, A.; De Wolf, S., Passivating contacts for crystalline silicon solar cells. *Nat Energy* **2019,** *4*, 914–928.

[4] Chen D, Kim M, Shi J, Vicari Stefani B, Yu Z, Liu S, Einhaus R, Wenham S, Holman Z, Hallam B. Defect engineering of p-type silicon heterojunction solar cells fabricated using commercial-grade low-lifetime silicon wafers. *Prog.Photovolt*. **2019**, 1, 1–15.

[5] Shockley W, Queisser HJ. Detailed balance limit of efficiency of p-n junction solar cells. *J. Appl. Phys*. **1961**, 32, 510–519.

[6] Iijima, S., Helical Microtubules of Graphitic Carbon. *Nature* **1991,** *354*, 56-58.

[7] Appenzeller, J.; Knoch, J.; Derycke, V.; Martel, R.; Wind, S.; Avouris, P., Field-modulated carrier transport in carbon nanotube transistors. *Phys Rev Lett* **2002,** *89*, 126801.

[8] Miyauchi, Y., Photoluminescence studies on exciton photophysics in carbon nanotubes. *J. Mater. Chem. C* **2013,** *1*, 6499–6521.

[9] Miyauchi, Y.; Iwamura, M.; Mouri, S.; Kawazoe, T.; Ohtsu, M.; Matsuda, K., Brightening of excitons in carbon nanotubes on dimensionality modification. *Nat. Photonics* **2013,** *7*, 715–719.

[10] Saito, R.; Fujita, M.; Dresselhaus, G.; Dresselhaus, M. S., Electronic structure of chiral graphene tubules. *Appl. Phys. Lett* **1992,** *60*, 2204–2206.

[11] Chen, C.; Lee, M; Clark, S. J., Band gap modification of single-walled carbon nanotube and boron nitride nanotube under a transverse electric field. *Nanotechnology* **2004,** *15*, 1837–1843.

[12] Dukovic, G.; Wang, F.; Song, D. H.; Sfeir, M. Y.; Heinz, T. F.; Brus, L. E., Structural dependence of excitonic optical transitions and band-gap energies in carbon nanotubes. *Nano Lett* **2005,** *5*, 2314–2318.

[13] Arora, N.; Sharma, N. N., Arc discharge synthesis of carbon nanotubes: Comprehensive review. *Diam Relat Mater* **2014,** *50*, 135–150.

[14] Scott, C. D.; Arepalli, S.; Nikolaev, P.; Smalley, R. E., Growth mechanisms for single-wall carbon nanotubes in a laser-ablation process. *Appl. Phys. Mater* **2001,** *72*, 573–580.

[15] Jing Kong, A. M. C., Hongjie Dai, Chemical vapor deposition of methane for single-walled carbon nanotubes. *Chem. Phys. Lett* **1998,** *292*, 567–574.

[16] Li, Y.; Kinloch, I. A.; Windle, A. H., Direct spinning of carbon nanotube fibers from chemical vapor deposition synthesis. *Science* **2004,** *304*, 276–278.

[17] Hu, L.; Hecht, D. S.; Gruner, G.; Carbon nanotube Thin film: Fabrication, Properties, and Applications. *Chem. Rev*. **2010**, 110, 5790–5844.

[18] Mirri, F.; Ma, A. W. K.; Hsu, T. T.; Behabtu, N.; Eichmann, S. L.; Young, C. C.; Tsentalovich, D. E.; Pasquali, M., High-Performance Carbon Nanotube Transparent Conductive Films by Scalable Dip Coating. *ACS Nano* **2012,** *6*, 9737–9744.

[19] Yu, L.; Shearer, C.; Shapter, J., Recent Development of Carbon Nanotube Transparent Conductive Films. *Chem Rev* **2016,** *116*, 13413–13453.

[20] Cross, R.; Cola, B. A.; Fisher, T.; Xu, X.; Gall, K.; Graham, S.A Metallization and Bonding Approach for High Performance Carbon Nanotube Thermal Interface Materials. *Nanotechnology*. **2010**, 21,445705.

[21] Hamdan, A.; Cho, J.; Johnson, R.; Jiao, J.; Bahr, D.; Richards, R.; Richards, C. Evaluation of a Thermal Interface Material Fabricated Using Thermocompression Bonding of Carbon Nanotube Turf. *Nanotechnology* **2010**, 21, 015702.

[22] Futaba, D. N.; Hata, K.; Yamada, T.; Hiraoka, T.; Hayamizu, Y.; Kakudate, Y.; Tanaike, O.; Hatori, H.; Yumura, M.; Iijima, S., Shape-engineerable and highly densely packed single-walled carbon nanotubes and their application as super-capacitor electrodes. *Nat Mater* **2006,** *5*, 987–994.

[23] Cui, L. F.; Hu, L. B.; Choi, J. W.; Cui, Y., Light-Weight Free-Standing Carbon Nanotube-Silicon Films for Anodes of Lithium Ion Batteries. *ACS Nano* **2010,** *4*, 3671–3678.

[24] Quintero, R.; Kim, D. Y.; Hasegawa, K.; Yamada, Y.; Yamada, A.; Noda, S., Carbon nanotube 3D current collectors for lightweight, high performance and low cost supercapacitor electrodes. *RSC Adv.* **2014,** *4*, 8230–8237.

[25] Tune, D. D.; Flavel, B. S., Advances in Carbon Nanotube-Silicon Heterojunction Solar Cells. *Adv. Energy Mater.* **2018,** *8*, 1703241.

[26] Yang, X.; Bi, Q.; Ali, H.; Davis, K.; Schoenfeld, W. V.; Weber, K., High-Performance TiO_2-Based Electron-Selective Contacts for Crystalline Silicon Solar Cells. *Adv. Mater* **2016,** *28*, 5891–5897.

[27] Li, Z.; Jia, Y.; Wei, J.; Wang, K.; Shu, Q.; Gui, X.; Zhu, H.; Cao, A.; Wu, D., Large area, highly transparent carbon nanotube spiderwebs for energy harvesting. *J. Mater. Chem.* **2010,** *20*, 7236–7240.

[28] Ma, W.; Song, L.; Yang, R.; Zhang, T.; Zhao, Y.; Sun, L.; Ren, Y.; Liu, D.; Liu, L.; Shen, J.; Zhang, Z.; Xiang, Y.; Zhou, W.; Xie, S., Directly synthesized strong, highly conducting, transparent single-walled carbon nanotube films. *Nano Lett* **2007,** *7*, 2307–2311.

[29] Kaskela, A.; Nasibulin, A. G.; Timmermans, M. Y.; Aitchison, B.; Papadimitratos, A.; Tian, Y.; Zhu, Z.; Jiang, H.; Brown, D. P.; Zakhidov, A.; Kauppinen, E. I., Aerosol-Synthesized

SWCNT Networks with Tunable Conductivity and Transparency by a Dry Transfer Technique. *Nano Lett* **2010,** *10*, 4349–4355.

[30] Nasibulin, A. G.; Kaskela, A.; Mustonen, K.; Anisimov, A. S.; Ruiz, V.; Kivisto, S.; Rackauskas, S.; Timmermans, M. Y.; Pudas, M.; Aitchison, B.; Kauppinen, M.; Brown, D. P.; Okhotnikov, O. G.; Kauppinen, E. I., Multifunctional Free-Standing Single-Walled Carbon Nanotube Films. *ACS Nano* **2011,** *5*, 3214–3221.

[31] Reynaud, O.; Nasibulin, A. G.; Anisimov, A. S.; Anoshkin, I. V.; Jiang, H.; Kauppinen, E. I., Aerosol feeding of catalyst precursor for CNT synthesis and highly conductive and transparent film fabrication. *Chem Eng J* **2014,** *255*, 134–140.

[32] Hecht, D. S.; Heintz, A. M.; Lee, R.; Hu, L.; Moore, B.; Cucksey, C.; Risser, S., High conductivity transparent carbon nanotube films deposited from superacid. *Nanotechnology* **2011,** *22*, 075201.

[33] Saran, N.; Parikh, K.; Suh, D.; Munoz, E.; Kolla, H.; Manohar, S. K., Fabrication and characterization of thin films of single-walled carbon nanotube bundles on flexible plastic substrates. *J. Am. Chem. Soc* **2004,** *126*, 4462–4463.

[34] Wu, Z.; Chen, Z.; Du, X.; Logan, J. M.; Sippe, J.; Nikolou, M.; Kamaras, K.; Reynolds, J. R.; Tanner, D. B.; Hebard, A. F; Rinzler1, A. G, Transparent, Conductive Carbon Nanotube Films. *Science* **2004**, 305, 1273–1276.

[35] Huang, X.; Xie, R.; Sugime, H.; Noda, S., Performance enhancement of carbon nanotube/silicon solar cell by solution processable MoO_x. *Appl. Sur. Sci* **2021,** *542*, 148682.

[36] Dan, B.; Irvin, G. C.; Pasquali, M., Continuous and Scalable Fabrication of Transparent Conducting Carbon Nanotube Films. *ACS Nano* **2009,** *3*, 835–843.

[37] Tune, D. D.; Hennrich, F.; Dehm, S.; Klein, M. F. G.; Glaser, K.; Colsmann, A.; Shapter, J. G.; Lemmer, U.; Kappes, M. M.; Krupke, R.; Flavel, B. S.; The role of nanatubes in carbon nanotube-silicon solar cells, *Adv. Energy Matter.* **2013**, 3, 1091–1097.

[38] Kozawa, D.; Hiraoka, K.; Miyauchi, Y.; Mouri, S,; Matsuda, K.; Analysis of the photovoltaic properties of single-walled carbon annotube/silicon heterojunction solar cells. *Appl. Phy. Express.* **2012**, 5, 042304

[39] Wei, J.; Jia, Y.; Shu, Q.; Gu, Z.; Wang, K.; Zhuang, D.; Zhang, G.; Wang, Z.; Luo, J.; Cao, A.; Wu, D., Double-walled carbon nanotube solar cells. *Nano Letters* **2007,** *7*, 2317–2321.

[40] Li, Z., Kunets, V.P., Saini, V., Xu, Y., Dervishi, E., Salamo, G.J., Biris, A.R. and Biris, A.S., Light-harvesting using high density p-type single wall carbon nanotube/n-type silicon heterojunctions. *ACS nano* **2009**, 3, 1407–1414.

[41] Jia, Y.; Cao, A.; Bai, X.; Li, Z.; Zhang, L.; Guo, N.; Wei, J.; Wang, K.; Zhu, H.; Wu, D.; Ajayan, P. M., Achieving high efficiency silicon-carbon nanotube heterojunction solar cells by acid doping. *Nano Lett* **2011,** *11*, 1901–1905.

[42] Shi, E.; Zhang, L.; Li, Z.; Li, P.; Shang, Y.; Jia, Y.; Wei, J.; Wang, K.; Zhu, H.; Wu, D.; Zhang, S.; Cao, A., TiO(2)-coated carbon nanotube-silicon solar cells with efficiency of 15%. *Sci Rep* **2012,** *2*, 884.

[43] Jung, Y.; Li, X..; Rajan, N. K.; Tayor, A. D.; Reed, M. A., Record High Efficiency Single-Walled Carbon Nanotube/Silicon p-n Junction Solar Cells. *Nano Lett* **2013,** *13*, 95–99.

[44] Cui, K.; Anisimov, A. S.; Chiba, T.; Fujii, S.; Kataura, H.; Nasibulin, A. G.; Chiashi, S.; Kauppinen, E. I.; Maruyama, S., Air-stable high-efficiency solar cells with dry-transferred single-walled carbon nanotube films. *J. Mater. Chem. A* **2014,** *2*, 11311–11318.

[45] Wang, F.; Kozawa, D.; Miyauchi, Y.; Hiraoka, K.; Mouri, S.; Ohno, Y.; Matsuda, K., Considerably improved photovoltaic performance of carbon nanotube-based solar cells using metal oxide layers. *Nat Commun* **2015,** *6*, 6305.

[46] Muramoto, E.; Yamasaki, Y.; Wang, F.; Hasegawa, K.; Matsuda, K.; Noda, S., Carbon nanotube–silicon heterojunction solar cells with surface-textured cfr cfrSi and solution-processed carbon nanotube films. *RSC Adv.* **2016,** *6*, 93575–93581.

[47] Cui, K.; Qian, Y.; Jeon, I.; Anisimov, A.; Matsuo, Y.; Kauppinen, E. I.; Maruyama, S., Scalable and Solid-State Redox Functionalization of Transparent Single-Walled Carbon Nanotube Films for Highly Efficient and Stable Solar Cells. *Adv. Energy Mater.* **2017,** *7*, 1700449.

[48] Qian, Y.; Jeon, I.; Ho, Y. L.; Lee, C.; Jeong, S.; Delacou, C.; Seo, S.; Anisimov, A.; Kaupinnen, E. I.; Matsuo, Y.; Kang, Y.; Lee, H. S.; Kim, D.; Delaunay, J. J.; Maruyama, S., Multifunctional Effect of p-Doping, Antireflection, and Encapsulation by Polymeric Acid for High Efficiency and Stable Carbon Nanotube-Based Silicon Solar Cells. *Adv. Energy Mater.* **2019,** *10*, 1902389.

[49] Xie, R.; Ishijima, N.; Sugime, H.; Noda, S., Enhancing the photovoltaic performance of hybrid heterojunction solar cells by passivation of silicon surface via a simple 1-min annealing process. *Sci Rep* **2019,** *9*, 1–7.

[50] Tune, D. D.; Mallik, N.; Fornasier, H.; Flavel, B. S., Breakthrough Carbon Nanotube-Silicon Heterojunction Solar Cells. *Adv. Energy Mater.* **2019,** *10*, 1903261.

[51] Chen, J.; Tune, D. D.; Ge, K.; Li, H.; Flavel, B. S., Front and Back-Junction Carbon Nanotube-Silicon Solar Cells with an Industrial Architecture. *Adv. Funct. Mater.* **2020,** *30*, 2000484.

[52] Chen, J.; Wan, L.; Li, H.; Yan, J.; Ma, J.; Sun, B.; Li, F.; Flavel, B. M.; A Polymer/Carbon-Nanotube Ink as a Boron-Dopant/Inorganic-Passivation Free Carrier Selective Contact for Silicon Solar cells over 21% Efficiency. *Adv. Funct. Mater*. **2020**, 30, 2004476.

[53] Havu, P.; Hashemi, M. J.; Kaukonen, M.; Seppala, E. T.; Nieminen, R. M., Effect of gating and pressure on the electronic transport properties of crossed nanotube junctions: formation of a Schottky barrier. *J Phys-Condens Mat* **2011,** *23*, 112203.

[54] Mohammed, M.; Li, Z.; Cui, J.; Chen, T., Acid-doped multi-wall carbon nanotube/n-Si heterojunctions for enhanced light harvesting. *Sol. Energy* **2014,** *106*, 171–176.

[55] I Lee, I.H., Kim, U.J., Son, H.B., Yoon, S.M., Yao, F., Yu, W.J., Duong, D.L., Choi, J.Y., Kim, J.M., Lee, E.H. and Lee, Y.H., Hygroscopic effects on $AuCl_3$-doped carbon nanotubes. *J. Phy. Chem. C* **2010** *114*, 11618–11622.

[56] Li, X.; Jung, Y.; Huang, J.; Goh, T.; Taylor, A. D., Device Area Scale-Up and Improvement of SWNT/Si Solar Cells Using Silver Nanowires. *Adv. Energy Mater.* **2014,** *4*, 1400186.

[57] Wang, F.; Kozawa, D.; Miyauchi, Y.; Hiraoka, K.; Mouri, S.; Ohno, Y.; Matsuda, K., Fabrication of Single-Walled Carbon Nanotube/Si Heterojunction Solar Cells with High Photovoltaic Performance. *Acs Photonics* **2014,** *1*, 360–364

[58] Miyadera, T.; Ogo, H.; Taima, T.; Yamanari, T.; Yoshida, Y., Analytical model for the design principle of large-area solar cells. *Sol. Energy Mater Sol. Cells* **2012,** *97*, 127–131.

[59] Xu, W.; Wu, S.; Li, X.; Zou, M.; Yang, L.; Zhang, Z.; Wei, J.; Hu, S.; Li, Y.; Cao, A., High-Efficiency Large-Area Carbon Nanotube-Silicon Solar Cells. *Adv. Energy Mater.* **2016,** *6*, 1600095.

[60] Greiner, M. T.; Chai, L.; Helander, M. G.; Tang, W.; Lu, Z., Transition Metal Oxide Work Functions: The Influence of Cation Oxidation State and Oxygen Vacancies. *Adv. Funct. Mater.* **2012,** *22*, 4557–4568.

[61] Bullock, J.; Cuevas, A.; Allen, T.; Battaglia, C., Molybdenum oxide MoO_x: A versatile hole contact for silicon solar cells. *Appl. Phy. Lett* **2014,** *105*, 232109.

[62] Meyer, J.; Kidambi, P. R.; Bayer, B. C.; Weijtens, C.; Kuhn, A.; Centeno, A.; Pesquera, A.; Zurutuza, A.; Robertson, J.; Hofmann, S., Metal oxide induced charge transfer doping and band alignment of graphene electrodes for efficient organic light emitting diodes. *Sci Rep* **2014,** *4*, 5380.

[63] Sanders, S.; Cabrero-Vilatela, A.; Kidambi, P. R.; Alexander-Webber, J. A.; Weijtens, C.; Braeuninger-Weimer, P.; Aria, A. I.; Qasim, M. M.; Wilkinson, T. D.; Robertson, J.; Hofmann,

S.; Meyer, J., Engineering high charge transfer n-doping of graphene electrodes and its application to organic electronics. *Nanoscale* **2015,** *7*, 13135–42.

[64] Hellstrom, S. L.; Vosgueritchian, M.; Stoltenberg, R. M.; Irfan, I.; Hammock, M.; Wang, Y. B.; Jia, C.; Guo, X.; Gao, Y.; Bao, Z., Strong and stable doping of carbon nanotubes and graphene by MoO_x for transparent electrodes. *Nano Lett* **2012,** *12*, 3574–80.

[65] Park, R. S.; Kim, H. J.; Pitner, G.; Neumann, C.; Mitra, S.; Wong, H. S.; Molybdenum oxide on carbon nanotube: Doping stability and correlation with work function. *J. Appl. Phys*. **2020**, 128. 045111.

[66] Esconjauregui, S.; D'Arsie, L.; Guo, Y.; Yang, J.; Sugime, H.; Caneva, S.; Cepek, C.; Robertson, J., Efficient Transfer Doping of Carbon Nanotube Forests by MoO_3. *ACS Nano* **2015,** *9*, 10422–10430.

[67] Jeon, I.; Cui, K.; Chiba, T.; Anisimov, A.; Nasibulin, A. G.; Kauppinen, E. I.; Maruyama, S.; Matsuo, Y., Direct and Dry Deposited Single-Walled Carbon Nanotube Films Doped with MoOx as Electron-Blocking Transparent Electrodes for Flexible Organic Solar Cells. *J. Am. Chem. Soc* **2015,** *137*, 7982–7985.

[68] Jeon, I.; Yoon, J.; Ahn, N.; Atwa, M.; Delacou, C.; Anisimov, A.; Carbon nanotues versus graphene as flexible transparent electrodes on inverted pervekite solar cells. J. Phys. Chem. Lett. **2017**, 8, 5395–5401.

[69] Yoon, J.; Kim, U.; Yoo, Y.; Byeon, J.; Lee, S. K.; Nam, Foldable Perovskite Solar Cells Using Carbon Nanotube-Embedded Ultrathin Polyimide Conductor. Adv. Sci. **2021**, 8, 2004092.

Chapter 2 Performance enhancement of carbon nanotube/silicon heterojunction solar cell by solution processable MoO_x

The part of the content of this Chapter has been published by Xiaoxu HUANG, et al., Performance enhancement of carbon nanotube/silicon solar cell by solution processable MoO_x, Appl. Surf. Sci. 542, 148682 (2021).

2.1 Introduction

Previous research [1–3] focused on using MoO_3 powders as the source for deposition of MoO_3 by thermal evaporation on carbon nanotubes (CNTs) films and CNTs forests. But this method usually requires high vacuum and long process time and is not suitable for large-scale and low-cost scalable production. On the other hand, MoO_x was found to be an effective hole selectivity layer in organic solar cells [4–6], where the MoO_x layer was prepared via spin-coating. Noticeably, there are few reports in applying the spin-coating for doping the CNTs films by MoO_x in CNT/Si heterojunction solar cells. This chapter demonstrates that the MoO_x precursor solution can significantly improve the power conversion efficiency (PCE) and enhance the air stability of the CNT/Si heterojunction solar cells. The influence of MoO_x on CNT/Si heterojunction solar cells was studied. It is found that the MoO_x worked as both an efficient p-type dopant and an enhancer for antireflective effect for CNTs films, which benefited to reduce the series resistance and enhance short-circuit current density of the solar cell. As a result, a high PCE of 10.0 % was achieved for the MoO_x–CNT/n-Si heterojunction solar cell, which is a 39% improvement from the pristine value of 7.2%. Moreover, the device exhibits a considerable enhancement in air stability, maintain the PCE at 80% of its original values for 1400 h under ambient environment without any protective layer. Application of

MoO_x layer by spin-coating for large-sized MoO_x–CNT/n-Si heterojunction solar cells was also explored.

2.2 Experiments

2.2.1 Preparation of CNT films and MoO_x precursor solution

CNT films were prepared using a solution method [7], whole preparation process was provided in Fig. 2.1. CNT powder (1–3 mg; MEIJO eDIPS, Meijo Nano Carbon Co., Ltd., Nagoya, Japan), which mainly consisted of single-walled CNTs with small amount of double- and triple-walled CNTs, was dispersed in 25 ~ 30 mL of a 0.5 wt% aqueous solution of sodium dodecylbenzene sulfonate (SDBS, Sigma Aidrich, St. Luouis, Mo, USA) via ultrasonication (VS-50R, VELVO-CLEAR, Tokyo Japan) while being cooled with an ice-bath process for 3 min. Then the dispersed CNTs solution was centrifugated at 4,000 rpm for 30 ~ 60 min to remove any undispersed CNTs bundles, and all the suspension was collected for CNTs films fabrication. The dispersion and centrifugation processes were repeated several times (3~4 times). The CNTs suspension was diluted and then poured into a vacuum filtration system, where a hydrophilic membrane filter (pore size 0.1 μm, VCWP, Merck Millipore, Darmstadt, Germany) was used to correct CNTs as a film. The CNT-membrane filter was slowly immersed in water to allow the CNTs films to separate and float on the water surface. Then the water was heated to ~ 100 °C to remove the surfactant (SDBS) from CNT film [8]. Finally, the CNTs films can be readily transferred onto a Si wafer by carefully picking up it from the water with the wafer. CNTs films on polyethylene terephthalate (PET) substrate with various optical transmittances (at 550 nm) and sheet resistances are shown in Fig. S2.1 and Table. S2.1 (Appendix). The MoO_x precursor solution was prepared by dissolving the ammonium hepta-molybdate ($(NH_4)_6Mo_7O_{24}\cdot 4H_2O$) powder (99.9%, Aldrich) in deionized water, then a 30% H_2O_2 solution was added to modify the solution [6]. As shown in Appendix, Table S2.2, the

MoO_x–CNT thin film fabricated with MoO_x precursor solution showed a lower sheet resistance of 172 Ω/sq than that fabricated with the ammonium hepta-molybdate aqueous solution without modification by H_2O_2 (214 Ω/sq). The addition of 30% H_2O_2 solution probably yielded per-oxo derivatives of poly-molybdates [9] that has superior doping effect compared to MoO_x. For improving the wettability of MoO_x precursor, the precursor solution was examined using water-ethanol (10%, 50%, 99% ethanol) mixed solution (Wako, Tokyo, Japan) instead of pure water.

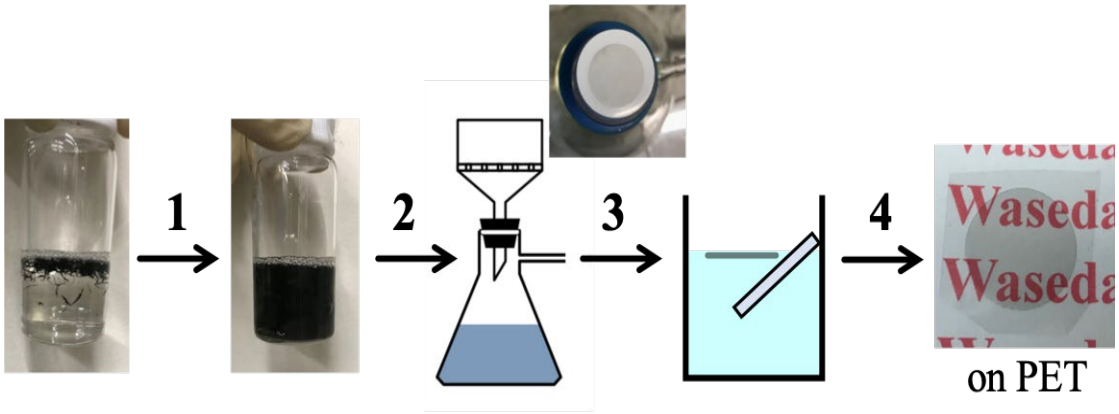

Fig. 2.1. The dispersion-filtration-transfer process of the carbon nanotube (CNT) film. (Step1: Dispersion of CNT powders in aqueous solution of a sodium dodecylbenzene sulfonate (SDBS). Step 2: Vacuum-filtration of the CNT dispersion via a membrane filter. Step 3: Releasing CNT film from the membrane filter and floating it onto water surface. Step 4: Transferring the CNT film onto a polyethylene terephthalate (PET) substrate by carefully removing it from the water with the PET substrate.)

2.2.2 Fabrication of solar cells and characterization

n-Type Si (n-Si) (100) wafers (1–5 Ω cm) with a circular opening (diameter of 2 mm, defined by 500 nm SiO_2 layer) were used to fabricate the small-sized solar cells. n-Type Si (100) wafers (1–2 Ω cm) with thickness of 625 ± 10 μm were used to fabricate the large-sized solar cells. The native SiO_2 layer on n-Si wafer was removed using 4.7 wt% hydrofluoric (HF) acid aqueous solution. The CNT/n-Si heterojunction was formed by carefully picking up the floated CNTs films from the water with the n-Si substate, and then drying it in a vacuum oven (100 °C,

3 min). Subsequently, the MoO_x was introduced onto CNTs films in the CNT/n-Si heterojunction by spin-coating the MoO_x precursor solution at 2,000 rpm for 60 s. For the small-sized solar cells, a rear In cathode was formed via welding an In wire by hand, which yields ohmic junction (Appendix), while a top Au electrode (100 nm in thickness) was deposited by using DC magnetron sputtering. For the large-sized solar cells, a full contact rear Al cathode (500 nm in thickness) was deposited using DC magnetron sputtering, while a top Au anode (300 nm in thickness, 9 fingers connected to a busbar, Appendix, Fig. S2.2a) was made by DC magnetron sputtering using a lithography-made Ni foil mask. The illumination area (4.0 cm^2) of solar cells was precisely determined (Appendix, Fig. S2.2b). The PEDOT: PSS–CNT/n-Si solar cell was fabricated for comparison by spin-coating the ploy(3,4-ethylenedioxythiophene):ploy(styrenesulfonate) (PEDOT:PSS) solution.

The optical transmittance (550 nm) and the sheet resistance of CNTs films on quartz glass substrate (0.5 mm in thickness) were evaluated by using ultraviolet-visible spectrophotometry (UV-Vis; V-630 JASCO, Tokyo, Japan) and four-point probe measurement, respectively. Four solar cells were fabricated for each condition and their photovoltaic (PV) performance was measured by a solar cell evaluation system (JASCO YQ–2000, Tokyo, Japan) under AM1.5 (P_{input}= 100 mW/cm^2) at 25 ℃. The top-view microstructure of the pristine CNT films and MoO_x–CNT films were observed by scanning electron microscopy (SEM, Hitachi S-4800, Tokyo, Japan). The chemical state of the MoO_x–CNT films and CNT films were analyzed by using X-ray photoelectron spectroscopy (XPS, JSP-9010TR) with Al Kα source (1486.6 eV). The binding energy was calibrated by fixing the binding energy value of C 1s to 284.6 eV. The work function of CNT films with/without MoO_x were measured using the ultraviolet photoelectron spectrometer (UPS, ULVAC–PHI, VersaProbe2) with a resolution of ~0.1 eV. He I (hν = 21.22 eV) and a negative bias of 5.00 V were used in normal emission geometry. The external quantum efficiency (EQE) measurements were performed using a CEP-2000

integrated system (Bunko-Keiki, Tokyo, Japan) with a Xe lamp attached to a monochromator (300–1200 nm). The CNT films with/without doping with MoO_x were characterized by using a Raman measurement (HR–800, Horiba, Kyoto, Japan) with an excitation wavelength of 488 nm. The surface reflectivity of the bare n-Si, the CNT/n-Si, and the MoO_x–CNT/n-Si were measured using a UV-Vis spectrophotometer (PerkinElmer, Lambda 650, USA). The crystal structure of the as-prepared MoO_x thin film on SiO_2/Si substrate was analyzed by X-ray diffraction (XRD; Rigaku RINT-Ultima III, Akishima, Japan) with a Cu Kα source.

2.3 Results and discussion

2.3.1 Characterization of the CNT films with and without doping with MoO_x

Fig. 2.2a shows the schematic of the preparation process of MoO_x–CNT/n-Si heterojunction solar cell. The CNT film was transferred onto n-Si substrate, followed by casting and spin-coating the MoO_x precursor solution. The XPS and UPS measurements were performed to analyze the doping mechanism of CNT films with MoO_x. The Mo peak (red line) was observed in CNT film after MoO_x coating (Fig. 2.2b). In the pristine CNT films, the O 1s core level peaks (Fig. 2.2c) indicate the presence of carbon-oxygen bonds; C–O–C, C–O–OH, and C–OH at the binding energy of 533.2 – 533.4 eV, and C=O and O–C=O at 532.2 eV [10]. In the MoO_x–CNT composite film, an additional peak at 530.6 eV was observed, suggesting the Mo–O bond [11]. Four peaks were detected in pristine CNT film and MoO_x–CNT film (Appendix, Fig. S2.3); C–C (sp^2) at 284.6 eV, C–C (sp^3) at 285.1–285.5 eV, C–O at 286.2 eV, and C=O at 287.7 – 287.8 eV [12–13]. An extra peak at 283.2 – 283.3 eV (Appendix, Fig. S 2.3b, c) was observed in the MoO_x–CNT film, which is associated with the C–Mo interaction indicating the p-doping of CNT [1]. The enhanced C–Mo peak was observed in CNT film doped with the MoO_x precursor solution of 4 wt% (Appendix, Fig. S2.3c), showing stronger p-doping than that with the MoO_x precursor solution of 0.4 wt%. The Mo 3d spectra of the MoO_x–CNT films

resulted a Mo $3d_{5/2}$ peak at 232.7 eV and a Mo $3d_{3/2}$ peak at 236.0 eV, which are attributed to the Mo^{6+} (Fig. 2.2e) [14]. Previous research suggested that the p-doping of CNT film by MoO_x can be effectively enhanced by post-annealing the MoO_x–CNT film at about 450 ℃ for 3 h in N_2 gas, which is evidenced by an appearance of Mo^{4+} at around 230 eV [2]. However, the Mo^{4+} did not observed in the Mo 3d spectrum of the MoO_x–CNT films fabricated with 0.4 wt% and 4 wt% MoO_x precursor solutions (Fig. S2.4a, c) possibly due to lack of a post-annealing process. Post-annealing of the MoO_x–CNT/n-Si heterojunction at the moderate annealing temperature of 300 ℃ for 1 h led to a degraded PV performance owing to the obvious increase in series resistance. The previous work [3] reported that the MoO_x can dope the CNT film without thermally annealing. The cutoff down-shifted by ~ 0.2 eV in UPS spectra (Fig. 2.2f), indicating the increased work function due to the p-type doping of CNT film by MoO_x [1]. The peak position of G-band blue-shifted by 2 cm^{-1} in Raman spectra (Fig. 2.2g), which provides further evidence of p-type doping of the CNT films by MoO_x [15]. The XRD pattern showed only broad halo pattern, suggesting that the as-prepared MoO_x thin film fabricated using the MoO_x precursor solution is amorphous (red line, Appendix, Fig. S2.5). And the 30% H_2O_2 solution has no effect on the crystal phase of MoO_x thin film (black line, Appendix, Fig. S2.5). Doping of the CNT film with MoO_x via spin-coting of the 0.4 wt% MoO_x precursor solution slightly reduced the optical transmittance ((88.6%)/ (90.8%)=0.976) and significantly decreased sheet resistance ((172 Ω/sq)/(228 Ω/sq)=0.754) (Fig. S2.6).

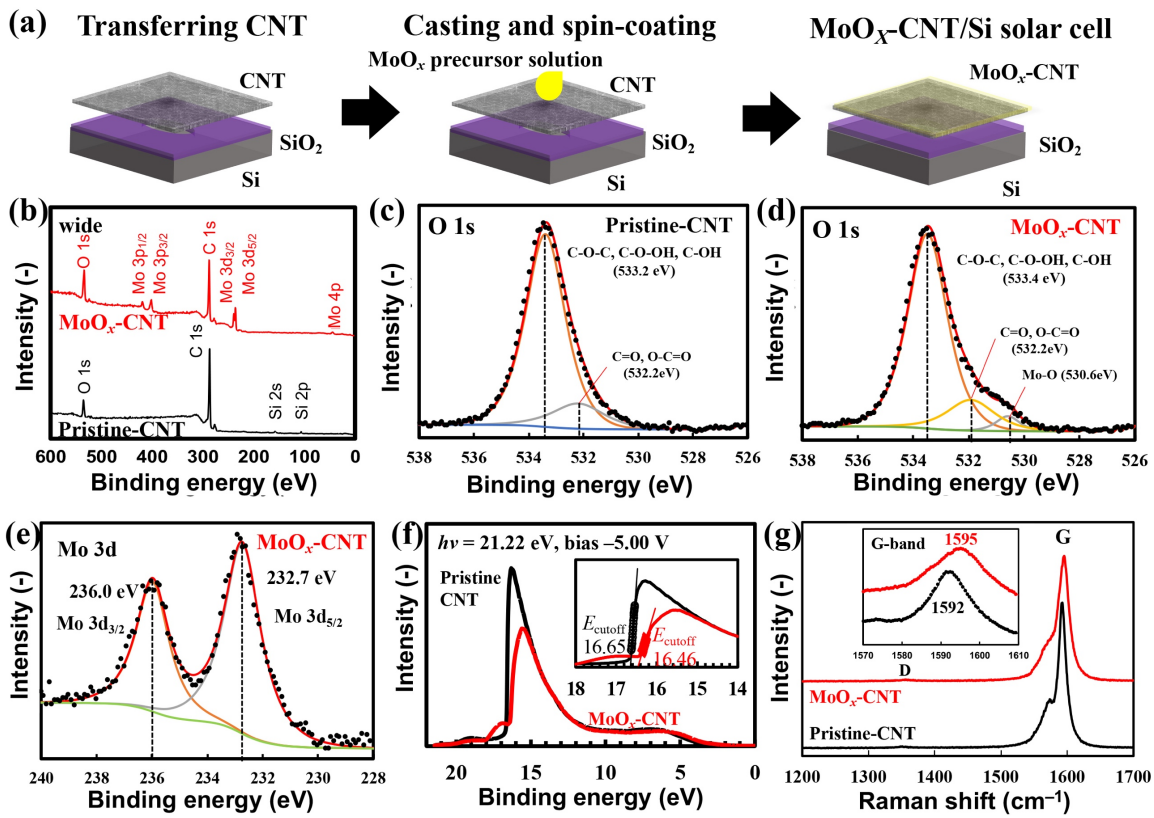

Fig. 2.2 (a) Schematics of the preparation process of the MoO_x–CNT/n-Si solar cells. (b) Wide-scan X-ray photoelectron spectroscopy (XPS) spectra of the CNT and MoO_x–CNT films. (c,d) O1s core level XPS spectra of the CNT film (c) and the MoO_x–CNT film (d). (e) Mo 3d core level XPS spectrum of the MoO_x–CNT films. (f) Ultraviolet photoelectron spectrometer (UPS) spectra of the CNT film (black line) and the MoO_x–CNT film (red line) with binding energy relative to the sample stage potential. (g) Raman spectra of the CNT films with and without the MoO_x. The samples were the CNTs films with ~90% transmittance at 550 nm and that treated with the 0.4 wt% MoO_x precursor solution.

2.3.2 Microstructure of CNT films with and without MoO_x

Fig. 2.3a, b shows the top-view SEM images of the CNT films (~ 90% transmittance at 550 nm) with and without spin-coating the MoO_x precursor solution on SiO_2/Si substrates. The pristine CNT films presented a spider-like network structure (Fig. 2.3a). The void space of the CNT films was fully filled by MoO_x after spin-coating the MoO_x precursor solution (Fig. 2.3b), which could help in reducing the tube–tube junction resistance and making the charge carrier

move more easily through the CNT network [16]. There effects are evidenced by the lower sheet resistance of the MoO_x–CNT film than the pristine CNT film (Appendix, Fig. S2.6).

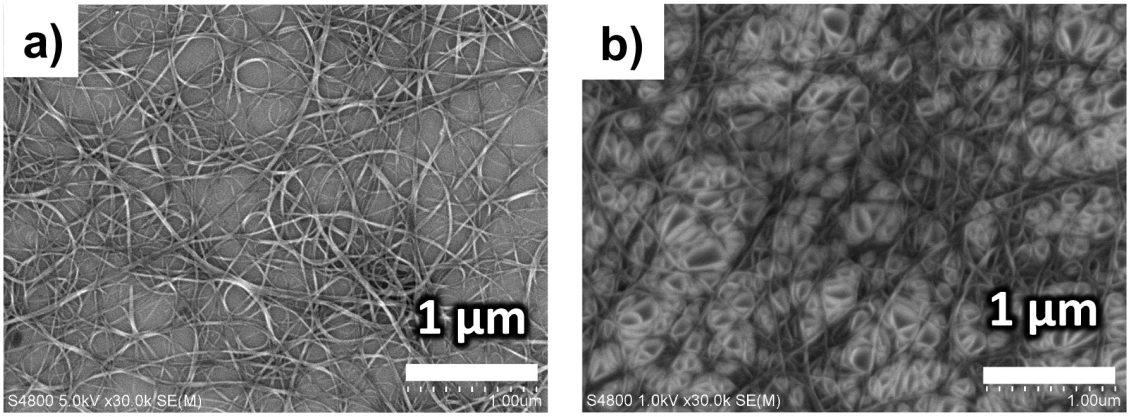

Fig. 2.3 Scanning electron microscopy (SEM) images of the pristine CNT film (a) and the MoO_x–CNT film (b) on the SiO_2/Si substrate. The MoO_x precursor solution of optimum concentration (0.4 wt%) was used.

2.3.3 PV performance of small-sized (0.0314cm^2) solar cells

The influence of the MoO_x precursor concentration on PV performance of MoO_x–CNT/n-Si solar cells was investigated, and the results were summarized in Fig. 2.4. Four solar cells were fabricated for each condition under identical conditions (Appendix, Fig. S2.7 and Table. S2.4). The optimized MoO_x precursor concentration was 0.4 wt%, this resulted in a high PCE of 10.0% of MoO_x–CNT/n-Si solar cell. The increased MoO_x precursor concentration improved the J_{sc} value from 28.1 to 30.4 mA/cm^2 and the FF value from 0.51 to 0.62 (Fig. 2.4b), indicating that a thicker MoO_x–CNT composite layer improved the anti-reflective effect and decreased the series resistance. However, when the MoO_x precursor concentration further increased to 4 wt%, the J_{sc} value decreased to 27.4 mA/cm^2 possibly due to the higher absorption of the incident light and/or the inhibition of the charge transfer through the CNT film by the thick and electrically resistive MoO_x [17].

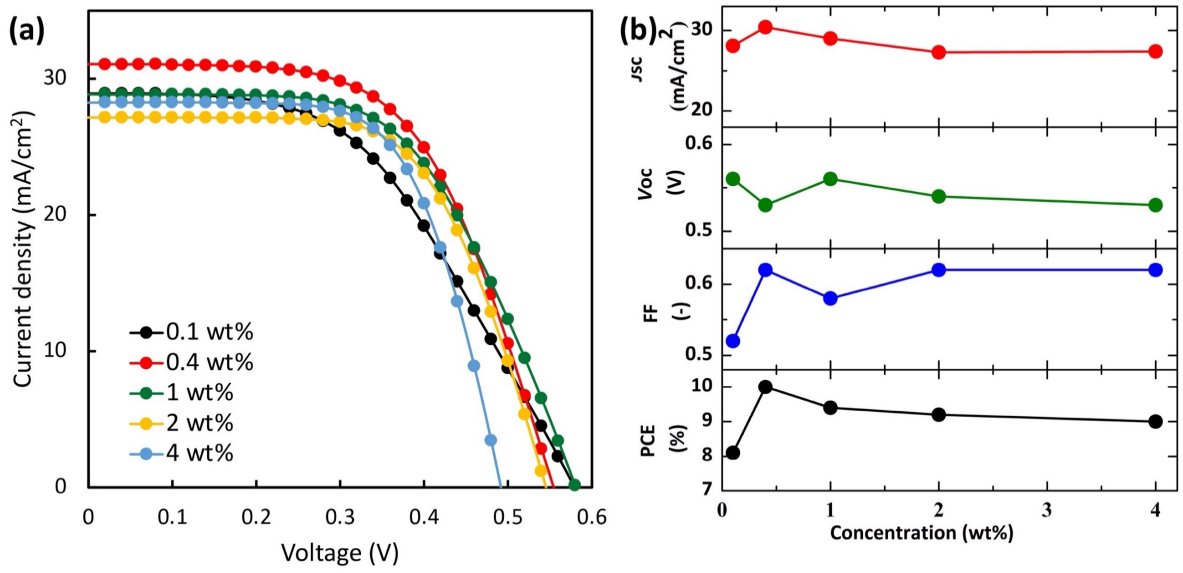

Fig. 2.4. *J–V* curves (a) and photovoltaic (PV) parameters (b) of MoO_x–CNT/n-Si solar cells fabricated using various MoO_x precursor solution concentrations.

Fig. 2.5a shows the comparison of the PV performance of the CNT/n-Si solar cells with and without MoO_x. The pristine CNT/n-Si solar cell showed a PCE of 7.4%, which results from the short-circuit current density (J_{sc}) value of 28.9 mA/cm^2, the open-circuit voltage (V_{oc}) value of 0.58 V and the fill factor (FF) value of 0.44 (Fig. 2.5a). The average PCE of four solar cells was 7.2% with a standard deviation of 0.5 % (Appendix, Fig. S2.7 and Table. S2.4). Compared with the pristine CNT/n-Si solar cell, the MoO_x–CNT/n-Si solar cell presented a higher J_{sc} of 31.1 mA/cm^2 and FF of 0.58. Consequently, the solar cell with the best PCE of 10.2% was realized. The average PCE of four solar cells was 10.0% with a standard deviation of 0.2% (Appendix, Fig. S2.7 and Table. S2.4), which is about 39% improvement from pristine value. The CNT/n-Si solar cell with MoO_x showed a larger EQE value in the wavelength range of 400-800 nm (Fig. 2.5b) and lower surface reflectivity that decreased from 31.3 to 28.5% (Fig. 2.5c), indicating that the MoO_x enhanced the AR effect and reduced the reflection of the incident light, increasing J_{sc}.

The dark ln *J–V* curves were analyzed to understand the carriers transport mechanism at the CNT/n-Si interface before and after spin-coating MoO_x precursor solution (Fig. 2.5d.). As

discussion previously, the CNT/Si heterojunction is complex and remains not understood well [18–20]. Here, thermionic emission theory is applied to evaluate the diode ideality factor (n) using the Equation below [21]:

$$\frac{\mathrm{d}V}{\mathrm{d}(\ln J)} = R_S * A_{eff}J + \frac{n}{\beta},$$

where R_s and A_{eff} are the series resistance and the effective diode area of the solar cell, respectively. n is the diode ideality factor, β is q/kT, q and k are the elementary charge and the Boltzmann constant, and T is temperature, Generally, the value of q/kT is obtained by plotting of $\mathrm{d}V/\mathrm{d}(\ln J)$ vs J using the dark ln *J-V* data. The ideal p-n junction shows a diode ideality factor of $1 < n < 2$, while the CNT/Si junction tends to exhibit $n > 2$, suggesting the mixed nature of the p-n and Schottky junctions due to the mixture of metallic and semiconducting CNTs [19–20]. The cells in this study also showed $n > 2$; 2.79 for the CNT/n-Si solar cell and 2.27 for the MoO_x–CNT/n-Si solar cell, respectively. The MoO_x–CNT/n-Si heterojunction has smaller n that enables more efficient separation of the hole-electron pairs from the heterojunction and lower diffusion recombination [22], leading to the FF value increasing from 0.44 to 0.58 (Fig. 2.5).

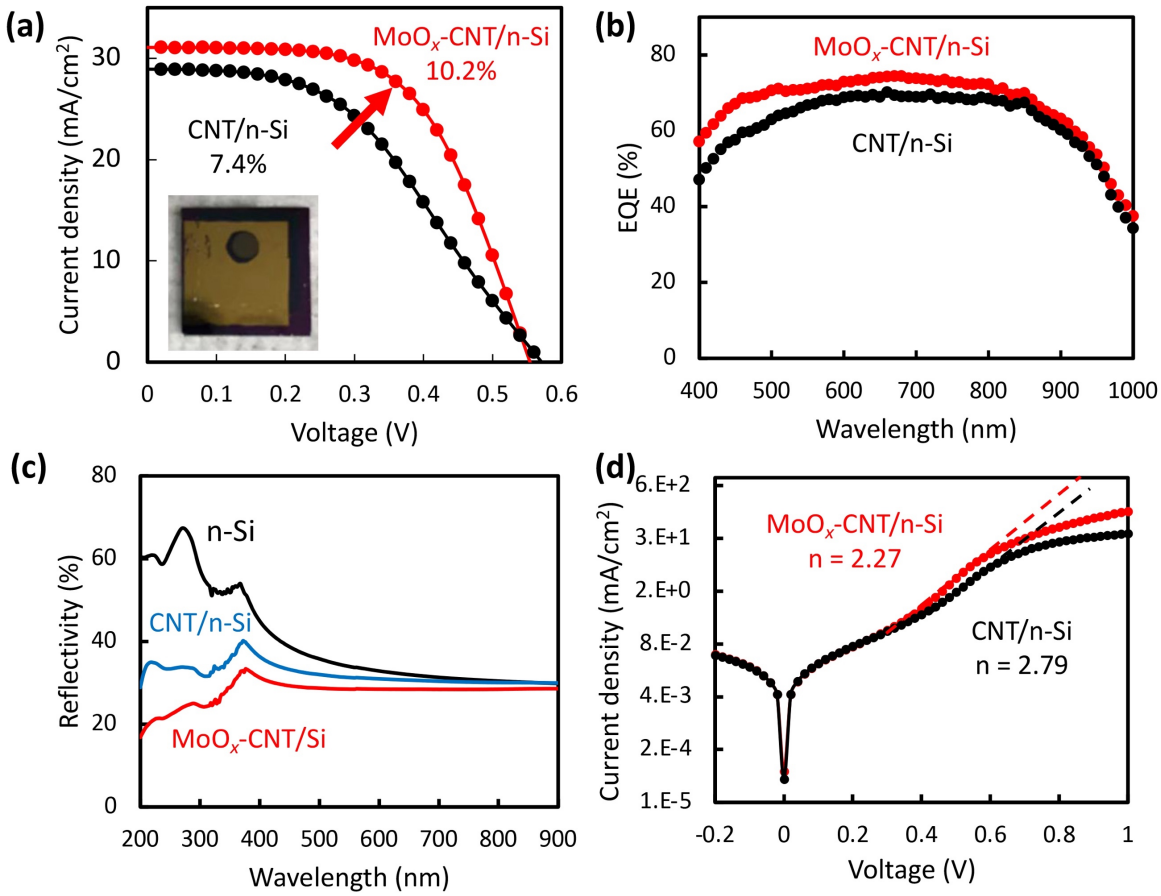

Fig. 2.5 (a) Comparison of the *J–V* characteristics of the pristine CNT/n-Si solar cell (black line) and the MoO_x–CNT/n-Si solar cell (red line). (b) External quantum efficiency (EQE) spectra of the CNT/n-Si solar cell (black line) and the MoO_x–CNT/n-Si solar cell (red line). (c) Optical surface reflectance spectra of the bare n-Si wafer, CNT/n-Si, and MoO_x–CNT/n-Si. (d) Dark ln *J–V* curves of the pristine CNT/n-Si solar cell and the MoO_x–CNT/n-Si solar cell. The CNT film with ~ 90% transmittance in 550 nm and the MoO_x precursor solution of 0.4 wt% were used.

The air stability is a key consideration for solar cells and the CNT/n-Si solar cells are no exception. Here, the air stability of the MoO_x–CNT/n-Si solar cells under ambient environment is tested and compared with that of the pristine CNT/n-Si solar cells and the PEDOT: PSS–CNT/n-Si solar cells. The MoO_x–CNT/n-Si solar cell maintained 80% of its original value when it was exposed to the air without any protection layer for 1440 h (red plots and line in Fig. 2.6, see also Appendix, Fig. S2.8a and Table. S2.5), indicating the device has a considerable stability in ambient environment. This is likely because the dense MoO_x–CNT

composite layer prevented the oxygen and water from penetration through porous CNT film and oxidizing the n-Si surface. Besides, it's noticed that the PCE of CNT/n-Si solar cell with MoO_x increased from 9.5% to 10.1% during the initial 360 h and then degraded to 8.1% when the device was exposed to the air (Fig. 2.6d). The enhanced PCE at the initial stage is possibly owing to the further oxidation of MoO_x in air and/ or the charge transfer between the CNT and MoO_x [1,23]. The finial decrease of the PCE is probably due to the oxidation of the n-Si surface, which can be explained by the increased series resistance and the reduced FF of the solar cell (Fig. 2.6b). In contrast, the CNT/n-Si solar cells dramatically decreased its PCE from 7.4% to 1.2% after storing in the air for 1440 h (black plots and line in Fig. 2.6, see also Appendix, Fig. S2.8b and Table. S2.4) and the PEDOT: PSS–CNT/n-Si solar cells presented the most severe degradation (green plots and lines in Fig. 2.6, see also Appendix, Fig. S2.8c and Table. S2.4). This is because the degradation in conductivity of the PEDOT: PSS when it is exposed in ambient environment [24]. The degraded PEDOT: PSS layer will severely increase the series resistance and recombination of the solar cell, thus, reducing the FF, J_{sc} and V_{oc} (Fig. 2.6a, b,c).

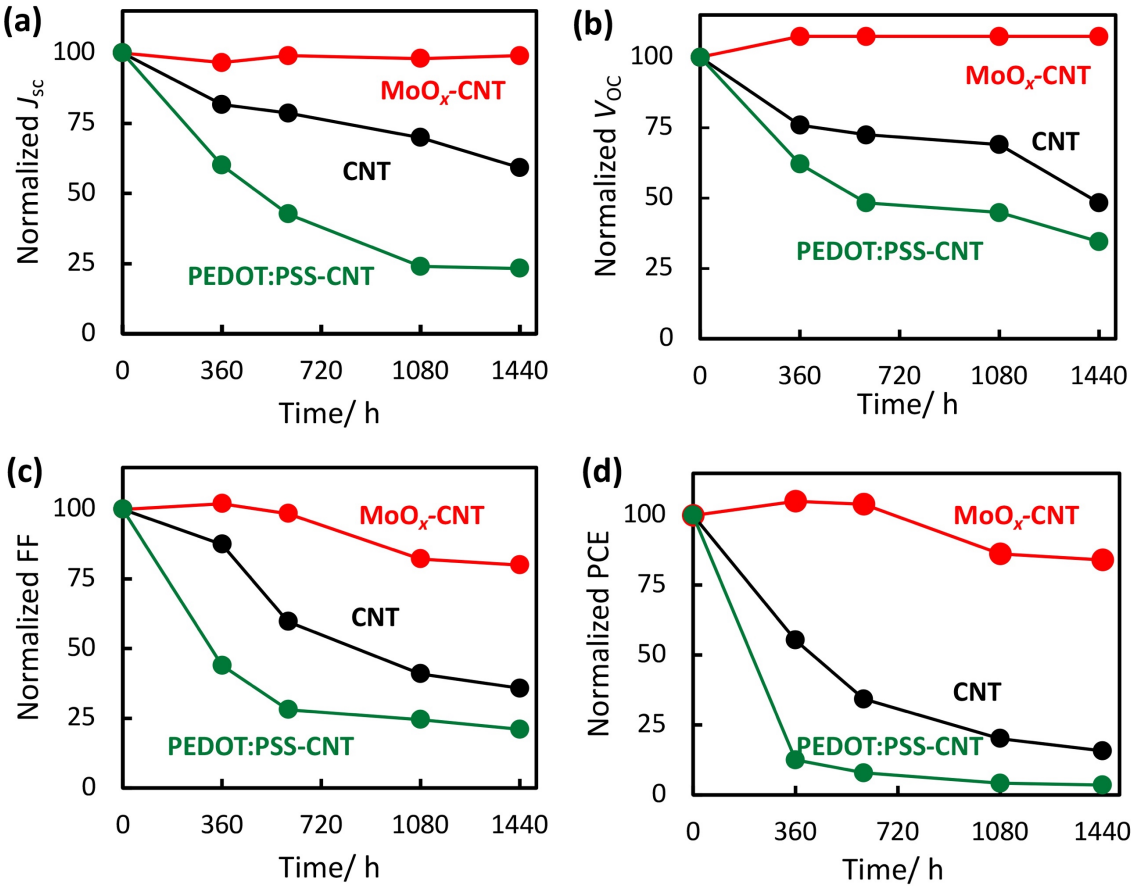

Fig. 2.6. Stability test of the solar cells in the ambient environments without any protective layer. (a) Short-circuit current-density (J_{sc}), (b) open circuit voltage (V_{oc}), (c) fill factor (FF), and (d) (Power conversion efficiency (PCE). The stability of the MoO_x–CNT/n-Si solar cell is compared with those of the pristine CNT/n-Si solar cell and the ploy(3,4-ethylenedioxythiophene):ploy(styrenesulfonate) (PEDOT:PSS)–CNT/n-Si solar cell.

2.3.4 PV performance of large-sized (4.0 cm^2) solar cells

2.3.4.1 Effect of active area on PV performance of CNT/Si solar cells

The CNT/Si solar cells with small and large active areas were fabricated to investigate the effect of active area on its PV performance (Fig. 2.7a). The PCE degradation of the CNT/Si solar cells upon the increase of active area is a common phenomenon [25–26]. The metal-grid based structure is compatible with scalable production for solar cells owing to their ability in facilitating carrier collection across the entire cell area [27]. For the current CNT/Si solar cells, the metal-grids can penetrate through the CNT film and reach the Si surface during metal grid

deposition due to the loose and porous structure of CNT film, resulting in severe current leakage in the device. As shown in Fig. 2.7a, the PCE of the pristine CNT/n-Si solar cells dramatically decreased from 7.2% to 1.3% with its active area increased from 0.0314 to 4.0 cm^2, which is attributed to the lower V_{oc} of 0.33 V, FF of 0.22 and J_{sc} of 17.94 mA/cm^2. Making CNT film dense via simple spin-coating MoO_x precursor solution onto the CNT film is expected to solve the current leakage by preventing the direct contact between metal grids and Si wafer. However, compared with the small-sized MoO_x–CNT/n-Si solar cells of PCE of 10.2%, the PCE of the large-sized cells MoO_x-CNT/n-Si solar cells is only of 1.4 % (Fig. 2.7 b). By further analyzing of the surface of the MoO_x–CNT composite thin films, it was found that the MoO_x was non-uniformly distributed on the large area CNT films due to the high hydrophobic property of CNT film surface. The non-uniform MoO_x–CNT composite film could not effectively prevent the metal grids and Si from coming into direct contact.

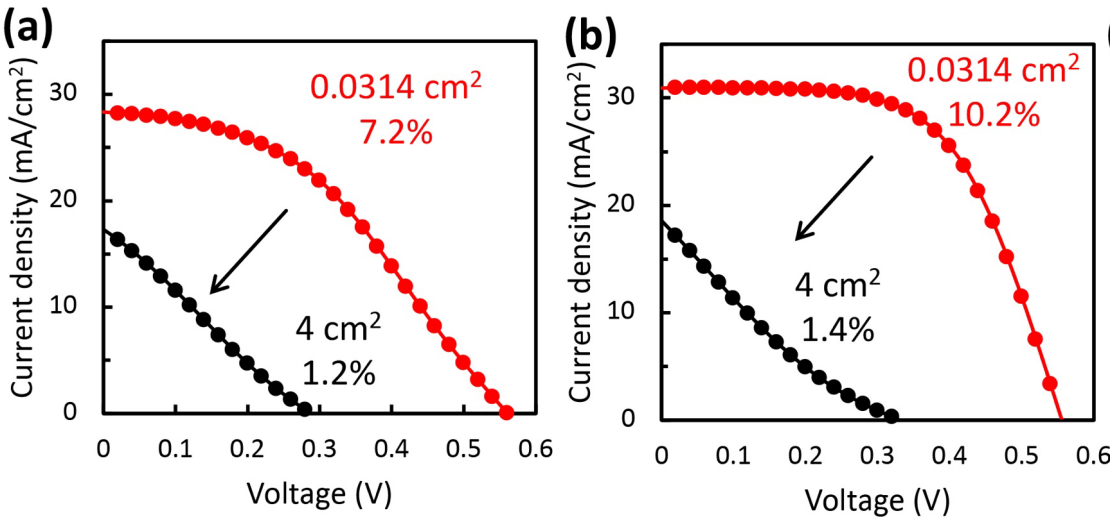

Fig. 2.7 (a) *J–V* curves of the (a) CNT/n-Si solar cells and (b) MoO_x-CNT/n-Si solar cells with active area of 0.0314 and 4.0 cm^2, respectively.

2.3.4.2 Improvement of wettability of MoO_x precursor solution.

Ethanol having smaller surface tension than water [28] will help improving the wettability of MoO_x precursor solution. Therefore, the ethanol-water mixed solution was used as the

solvent to prepare the MoO_x precursor solution instead of pure water. As expected, the ethanol-water based MoO_x precursor solution yielded more uniform MoO_x layer on the CNT film. However, the PV performance of the MoO_x–CNT/n-Si solar cells degraded compared with the pristine cells (Fig. 2.8) with poorer PV performance with ethanol of higher concentrations. This probably because the MoO_x precursor has a poor solubility in ethanol solution and the MoO_x precursor was not fully hydrolyzed into MoO_x in ethanol solution.

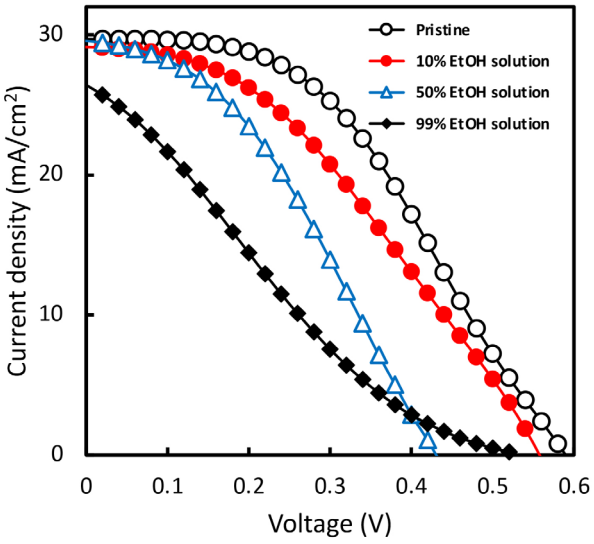

Fig. 2.8. *J–V* characteristics of the CNT/n-Si solar cells doped with the MoO_x precursor solution prepared using ethanol-water mixed solution of various ethanol concentrations.

2.4 Conclusions

In this chapter, a solution processable MoO_x that enhances the PV performance of the CNT/n-Si solar cells was reported. Simple spin-coating of the MoO_x precursor solution onto the CNT film significantly improved the PCE from 7.2% to 10.0% and air stability (efficiency after 1440 h from 1.2% to 8.1%) for the small-sized cell (active area of 0.0314 cm^2). The MoO_x was demonstrated to have multiple functions for improvement of PV performance of the CNT/n-Si solar cells. It works as a p-type dopant for the CNT film for lower series resistance, an enhancer for the anti-reflection effect of the MoO_x–CNT layer, and a protective layer for the

CNT/n-Si interface. For the large-sized solar cell fabrication, the solution-processable MoO_x did not effectively prevent the current leakage owing to the non-uniform distribution of the MoO_x thin layer on the CNT film that was caused by the high hydrophobic properties of the surface of the CNT films. The PCE of the large-sized CNT/n-Si solar cell was not obviously enhanced by coating with MoO_x. The wettability of MoO_x precursor solution was improved by adding ethanol to the MoO_x precursor solution. As a result, a more uniform MoO_x layer on large-area CNT film was achieved. However, the PCE of the solar cell decreased with ethanol of higher concentrations probably due to the MoO_x precursor being not fully hydrolyzed into MoO_x in the ethanol-water mixed solution.

Appendix

Evaluation of the work function of n-Si and the junction type of n-Si/In.

Dopant (P) concentration is estimated as n_D = 1–5×10^{15} cm^{-3} from its resistivity (ρ = 1–5 Ω cm) and reference [A]. The intrinsic carrier concentration is n_i = 1.07×10^{10} cm^{-3} at 300 K from reference [B]. The Fermi level of the intrinsic Si is $E_i \approx \frac{E_V+E_D}{2} = -4.61$ (eV) relative to vacuum level where E_v and E_D are the valence band energy (–5.17 eV) and the conduction band energy (–4.05 eV), respectively [C, D]. The Fermi level of n-Si is estimated to be –4.31 ≤ E_F ≤ –4.27 eV using the equation $E_F = E_i + kT\ln(\frac{n_D}{n_i})$.

When a metal and semiconductor are brought into contact, two types of junction form depending on the work function of the semiconductor (Φ_s) and that of the metal (Φ_m). In case of the junction between a metal and n-type semiconductor,

1. Schottky junction - $\Phi_m > \Phi_s$
2. Ohmic junction - $\Phi_m < \Phi_s$

Here In has Φ_m = 4.09 eV [E] and the n-Si (1–5 Ω cm) has 4.27 ≤ Φ_s ≤ 4.31 eV. Because of $\Phi_m < \Phi_s$, the n-Si/In junction is ohmic.

References

[A] F. Mousty, P. Ostoja, L. Passari, Relationship between resistivity and phosphorus concentration in silicon, J. Appl. Phys. 45 (1974) 4576-4580.

[B] J. L. Gray, The physics of the solar cell, in: A. Luque, S. Hegedus (Eds.), Handbook of Photovoltaic Science and Engineering, 2nd Edition, Wiley, 2011, pp. 89–91.

[C] V. P. Ulin, N. V. Ulin, F. Yu. Soldatenkov, Anodic processes in the chemical and electrochemical etching of Si crystals in acid-fluoride solutions: Pore formation mechanism, Semiconductors 51 (2017) 458-472.

[D] M. A. Green, Intrinsic concentration, effective densities of states, and effective mass in silicon, J. Appl. Phys. 67 (1990) 2944-2954

[E] D. R. Lide (Ed), CRC Handbook of Chemistry and Physics, CRC Press, 2004. p. 12-124.

Table S2.1. The detail of the sheet resistance of the CNT films with various optical transmittances.

Sample	Transmittance (%)	Sheet resistance (Ω/sq)
T1	90	225
T2	85	136
T3	80	95
T4	75	70

Table S2.2. The detail of the sheet resistance of CNT film on a quartz glass substrate before and after doping. Three different dopants were applied: (i) 0.4 wt% MoO_x precursor solution modified with and without 30% H_2O_2 solution; (ii) 30% H_2O_2 solution.

Doping	Transmittance (550 nm) %	Sheet resistance (Ω/sq) Pristine CNT film	Sheet resistance (Ω/sq) Doped CNT film	Ratio
MoO_x precursor w/o H_2O_2	91.4	237 ± 2	214 ± 1	(214)/(237)= **0.90**
H_2O_2	91.6	233 ± 4	219 ± 2	(219)/(233)= **0.93**
MoO_x precursor w/ H_2O_2	90.8	228 ± 3	172 ± 5	(172)/(228)= **0.76**

Table S2.3. Fraction of each component in XPS O 1s spectra of the CNT films in Fig. S2.3.

MoO_x precursor solution	533.2±0.2 eV (C–O–C) (%)	532.3±0.2 eV (H_2O) (%)	531.2±0.2 eV (–OH) (%)	530.2±0.2 eV (Mo–O) (%)
0.4 wt%	84.3	2.6	10.2	2.9
4 wt%	19.7	7.9	30.6	41.8

Table S2.4. The detail of the photovoltaic parameters of the MoO_x–CNT/n-Si solar cells fabricated using the various MoO_x precursor concentrations.

Concentration (wt%)	J_{SC} (mA/cm^2)	V_{OC} (V)	FF (-)	PCE (%)
pristine	28.5 ± 1.1	0.55 ± 0.04	0.45 ± 0.04	**7.2 ± 0.5**
0.1	28.1 ±1.0	0.56 ±0.02	0.51 ±0.04	**8.1 ±0.1**
0.4	30.4 ±2.0	0.53 ±0.02	0.62 ±0.06	**10.0 ±0.2**
1	29.0 ±1.1	0.56 ±0.02	0.58 ±0.01	**9.4 ±0.1**
2	27.3 ±0.6	0.54 ±0.00	0.62 ±0.01	**9.2 ±0.1**
4	27.4 ±0.6	0.53 ±0.02	0.62 ±0.01	**9.0 ±0.1**

Table S2.5. The detail of the photovoltaic parameters of the MoO_x–CNT/n-Si solar cells stored in ambient air for different periods of time without any protect layer.

Time (h)	J_{SC} (mA/cm^2)	V_{OC} (V)	FF (-)	PCE (%)
0	29.5	0.54	0.60	9.5
360	28.5	0.58	0.61	10.1
480	29.2	0.58	0.59	9.9
1080	28.9	0.58	0.49	8.2
1440	29.2	0.58	0.48	8.1

Table S2.6. The detail of the photovoltaic parameters of CNT/n-Si solar cells stored in ambient air for different periods of time without any protect layer.

Time (h)	J_{SC} (mA/cm^2)	V_{OC} (V)	FF (-)	PCE (%)
0	28.9	0.58	0.44	7.4
360	23.6	0.44	0.38	4.1
480	22.7	0.42	0.26	2.5
1080	20.2	0.4	0.18	1.5
1440	17.1	0.28	0.25	1.2

Table S2.7. The detail of the photovoltaic parameters of PEDOT:PSS–CNT/n-Si solar cells stored in ambient air for different periods of time without any protect layer.

Time (h)	J_{SC} (mA/cm^2)	V_{OC} (V)	FF (-)	PCE (%)
0	28.8	0.58	0.57	9.6
360	17.4	0.36	0.25	1.2
480	12.3	0.28	0.16	0.7
1080	6.9	0.26	0.14	0.4
1440	6.7	0.20	0.12	0.3

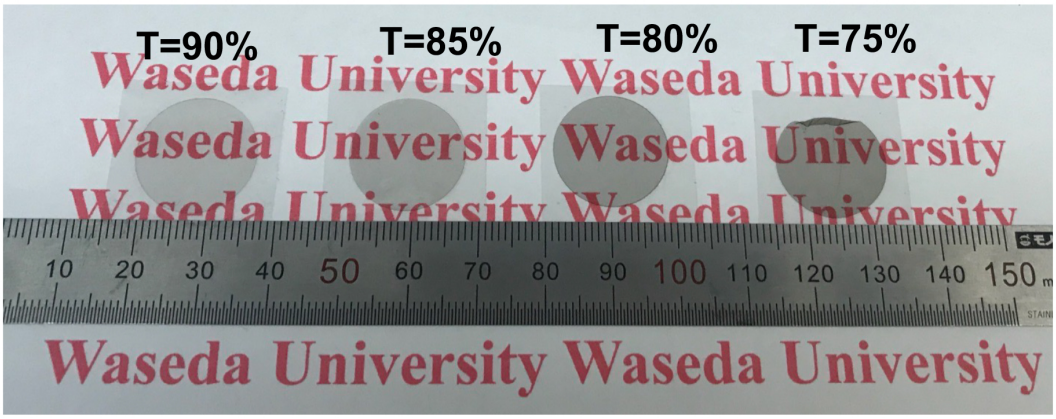

Fig. S2.1. Photographs of the filtrated CNT films on polyethylene terephthalate (PET) substrates with various optical transmittances.

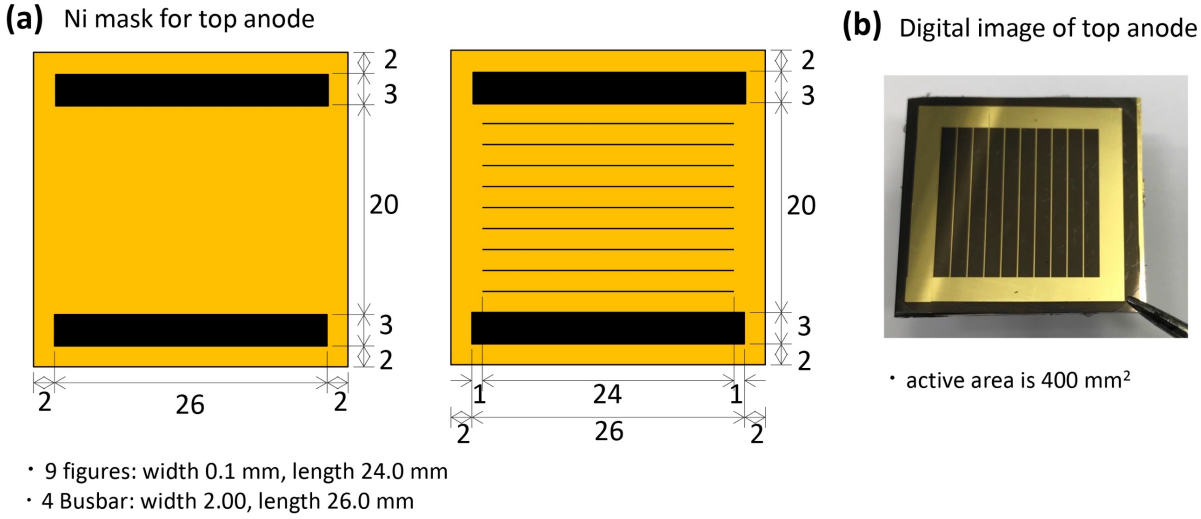

Fig. S2.2 Design of the mask used in fabricating the large-sized solar cells. (a) The lithography-based Ni foil mask for the top anode (thickness of 50 μm; fingers of 0.1 mm in width, 9 lines at 2 mm pitch, 20.0 × 20.0 mm^2 region was determined by 4 busbar of 26 × 3 mm^2). (b) digital image of a large-sized solar cells with Au grid top anode.

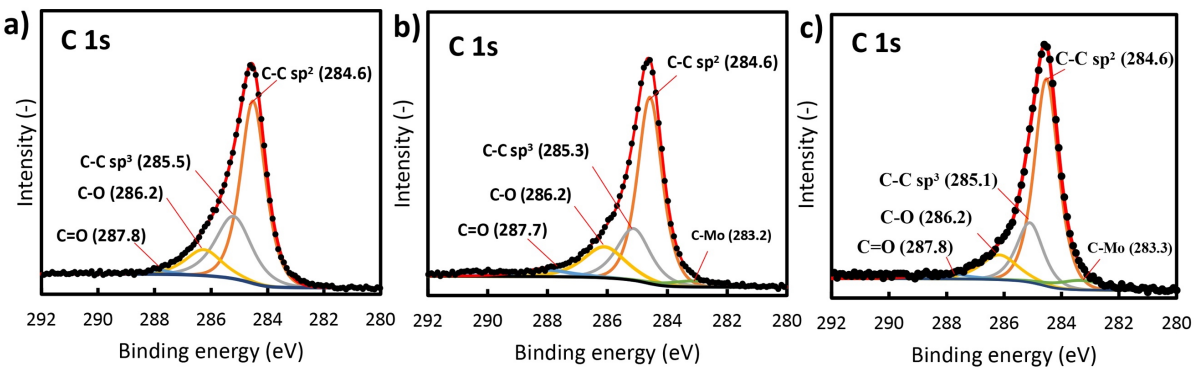

Fig. S2.3. C 1s core level spectra in (a) pristine CNT, (b) 0.4 wt% MoO_x–CNT films and (c) 4 wt% MoO_x–CNT films. The transmittance of CNT film is ~90% for (a–c).

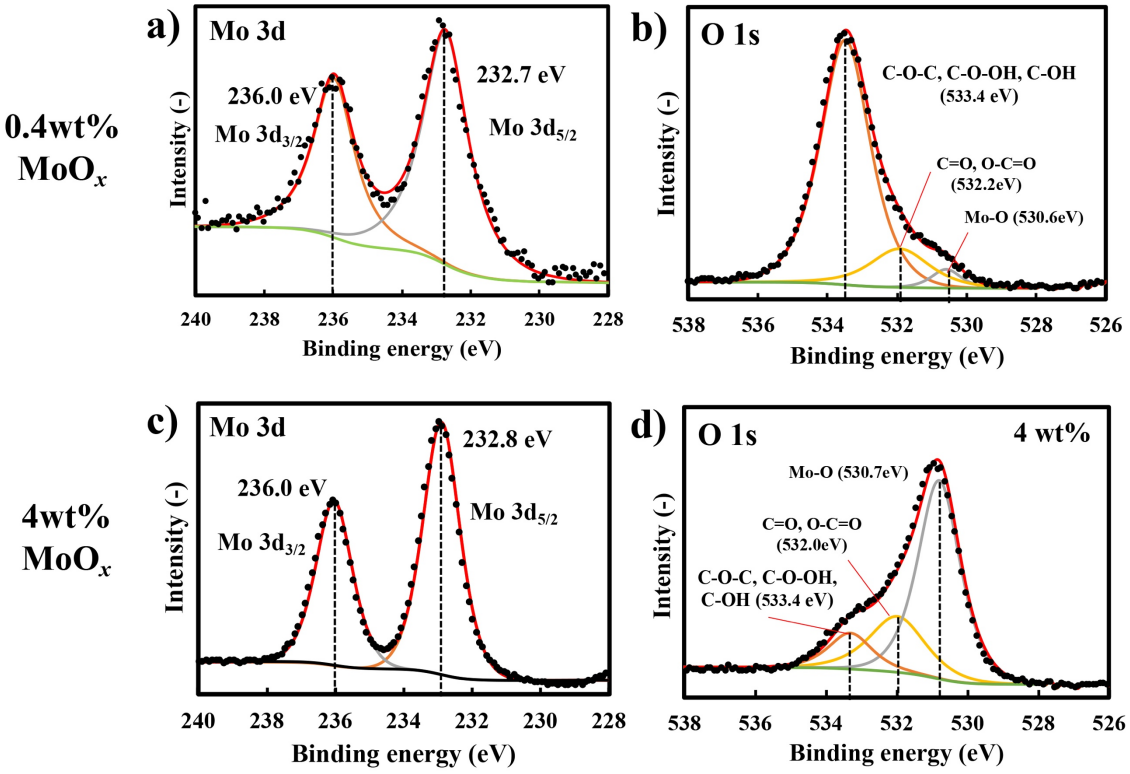

Fig. S2.4. C 1s core level spectra in (a) pristine CNT, (b) 0.4 wt% MoO_x–CNT films and (c) 4 wt% MoO_x–CNT films. The transmittance of CNT film is ~90% for (a–c).

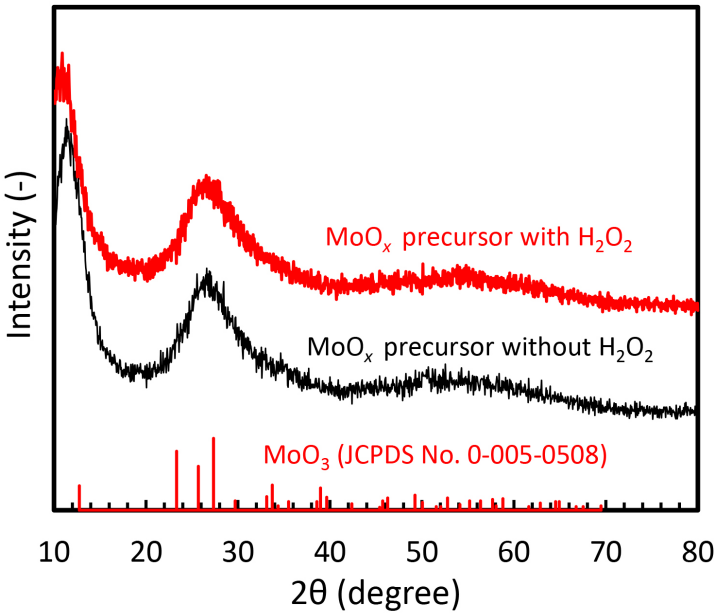

Fig. S2.5. X-ray diffraction (XRD) spectrum of MoO_x layer fabricated via spin-coating 0.4 wt% MoO_x precursor solution. Ammonium heptamolybdate aqueous solusion with (red line) and without (black line) modifying with 30% H_2O_2 solution.

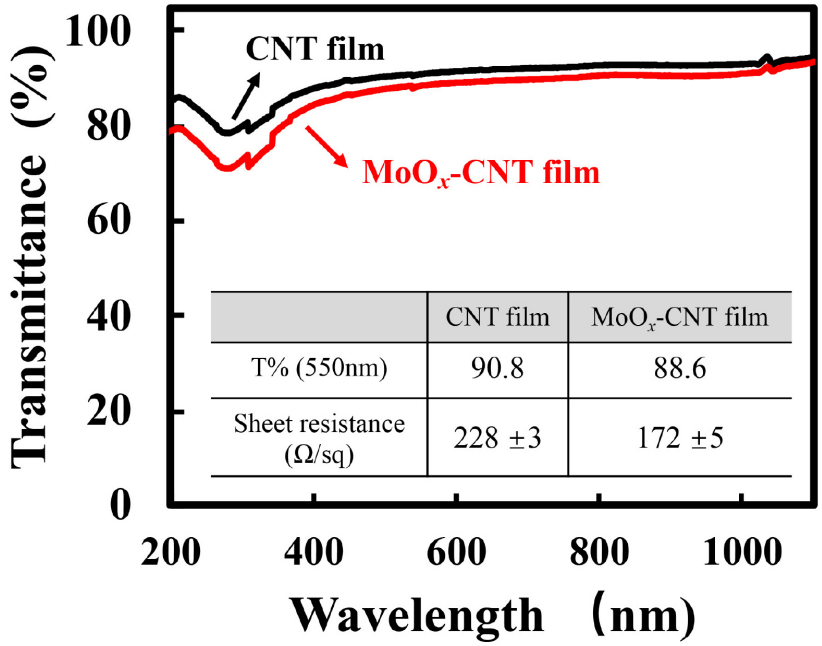

	CNT film	MoO$_x$-CNT film
T% (550nm)	90.8	88.6
Sheet resistance (Ω/sq)	228 ±3	172 ±5

Fig. S2.6. The transmittance spectra of the CNT film on a quartz glass substrate before and after doping with 0.4 wt% MoO_x precursor solution. Inset table shows the transmittance at 550 nm and sheet resistance with standard deviation of the CNT film.

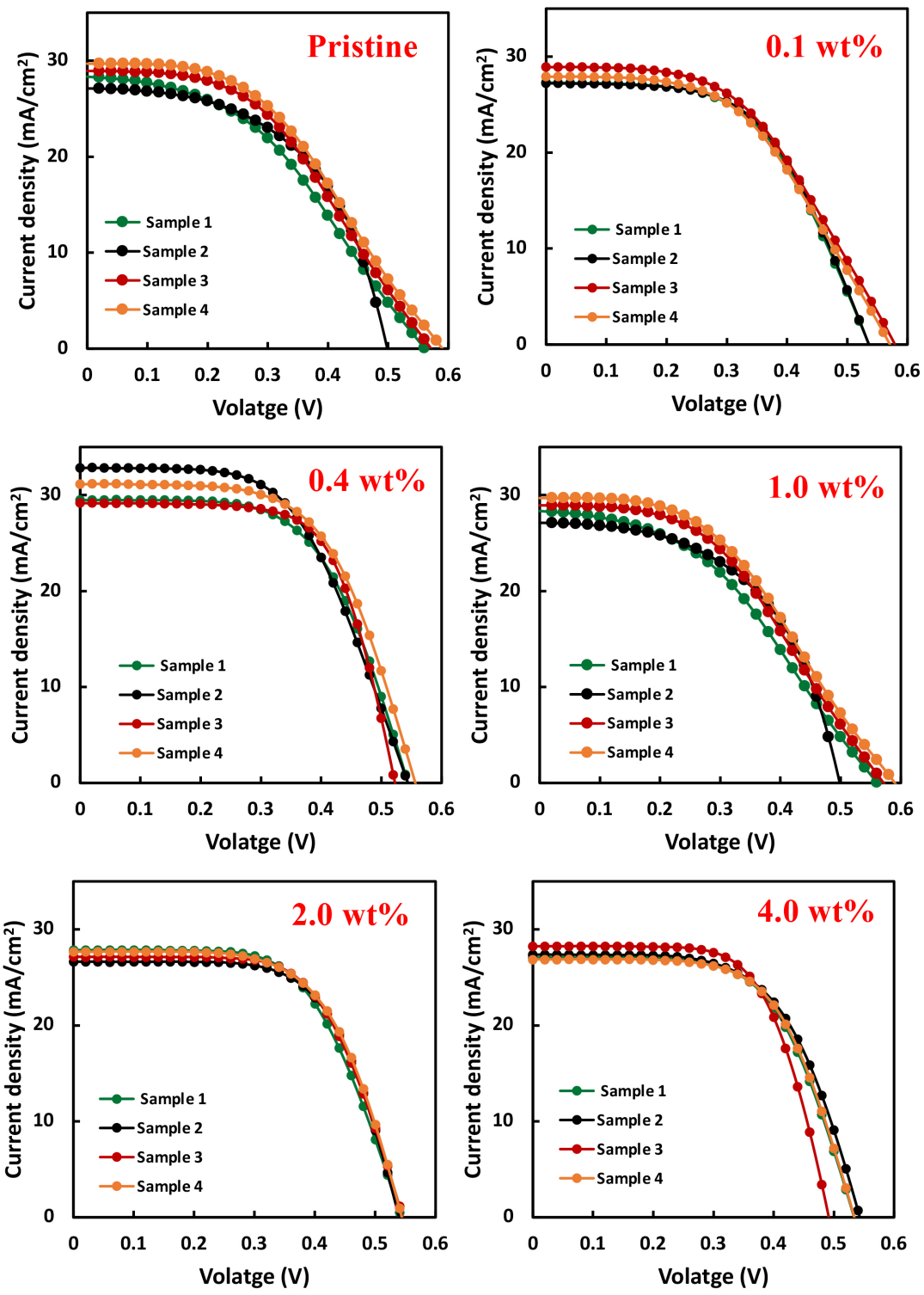

Fig. S2.7. (a) *J–V* characteristics of the MoO_x–CNT/n-Si solar cells fabricated using the MoO_x precursor solution of various concentrations.

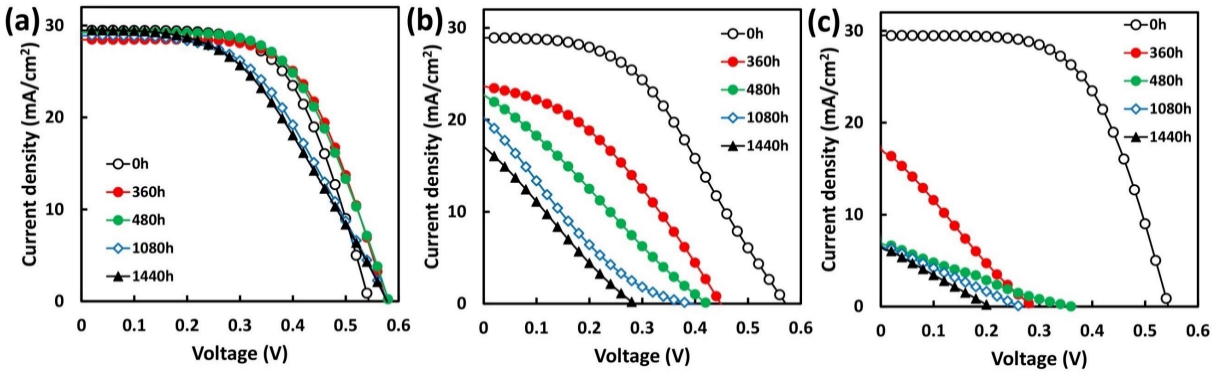

Fig. S2.8. *J–V* characteristics of (a) MoO_x–CNT/n-Si solar cells, (b) CNT/n-Si solar cells and (c) PEDOT: PSS–CNT/n-Si solar cells stored in ambient air for different periods of time without any protective layer.

References

[1] Hellstrom, S. L.; Vosgueritchian, M.; Stoltenberg, R. M.; Irfan, I.; Hammock, M.; Wang, Y.; Jia, C.; Guo, X.; Gao, Y.; Bao, Z., Strong and stable doping of carbon nanotubes and graphene by MoO_x for transparent electrodes. *Nano Lett* **2012,** *12*, 3574–3580.

[2] Esconjauregui, S.; D'Arsie, L.; Guo, Y.; Yang, J.; Sugime, H.; Caneva, S.; Cepek, C.; Robertson, J., Efficient Transfer Doping of Carbon Nanotube Forests by MoO_3. *ACS Nano* **2015,** *9*, 10422–10430.

[3] Wang, F.; Kozawa, D.; Miyauchi, Y.; Hiraoka, K.; Mouri, S.; Ohno, Y.; Matsuda, K., Considerably improved photovoltaic performance of carbon nanotube-based solar cells using metal oxide layers. *Nat Commun* **2015,** *6*, 6305.

[4] Zilberberg, K.; Gharbi, H.; Behrendt, A.; Trost, S.; Riedl, T., Low-temperature, solution-processed MoO(x) for efficient and stable organic solar cells. *ACS Appl. Mater. Interfaces* **2012,** *4*, 1164–1168.

[5] Liu, F.; Shao, S.; Guo, X.; Zhao, Y., Efficient polymer photovoltaic cells using solution-processed MoO3 as anode buffer layer. *Sol. Energy Mater Sol. Cells* **2010,** *94*, 842–845.

[6] Qiu, W.; Hadipour, A.; Muller, R.; Conings, B.; Boyen, H. G.; Heremans, P.; Froyen, L., Ultrathin ammonium heptamolybdate films as efficient room-temperature hole transport layers for organic solar cells. *ACS Appl. Mater. Interfaces* **2014,** *6*, 16335–16343.

[7] Shirae, H.; Kim, D. Y.; Hasegawa, K.; Takenobu, T.; Ohno, Y.; Noda, S., Overcoming the quality–quantity tradeoff in dispersion and printing of carbon nanotubes by a repetitive dispersion–extraction process. *Carbon* **2015,** *91*, 20–29.

[8] Muramoto, E.; Yamasaki, Y.; Wang, F.; Hasegawa, K.; Matsuda, K.; Noda, S.; Carbon nanotube–silicon heterojunction solar cells with surface-textured Si and solution-processed carbon nanotube films, *RSC Adv*. **2016,** 6, 93575–93581.

[9] Csányi, L J., Peroxide derivatives of molybdenum (VI) in acidic solution. *Transit. Met.*

Chem. **1989**, 14, 298–302.

[10] Datsyuk, V.; Kalyva, M.; Papagelis, K.; Parthenios, J.; Tasis, D.; Siokou, A.; Kallitsis, I.; Galiotis, C., Chemical oxidation of multiwalled carbon nanotubes. *Carbon* **2008,** *46*, 833–840.

[11] Dupin, J.C.; Gonbeau, D.; Vinatier, P.; Levasseur, A., Systematic XPS studies of metal oxides, hydroxides and peroxides. *Phys. Chem. Chem. Phys* **2000,** *2*, 1319–1324.

[12] Nina I. Kovtyukhova, T. E. M., Ling Pan, and Elizabeth C. Dickey, Individual Single-Walled Nanotubes and Hydrogels Made by Oxidative Exfoliation of Carbon Nanotube Ropes. *J. Am. Chem. Soc* **2003**, *125*, 9761-9769.

[13] Pirlot, C.; Willems, I.; Fonseca, A.; Nagy, J. B.; Delhalle, J., Preparation and characterization of carbon nanotube/polyacrylonitrile composites. *Adv Eng Mater* **2002,** *4*, 109–114.

[14] Chastain, J.; King Jr, R. C., Handbook of X-ray photoelectron spectroscopy. *Perkin-Elmer Corporation* **1992,** *40*, 221.

[15] Cui, K.; Qian, Y.; Jeon, I.; Anisimov, A.; Matsuo, Y.; Kauppinen, E. I.; Maruyama, S., Scalable and Solid-State Redox Functionalization of Transparent Single-Walled Carbon Nanotube Films for Highly Efficient and Stable Solar Cells. *Adv. Energy Mater.* **2017,** *7*, 1700449.

[16] Havu, P.; Hashemi, M. J.; Kaukonen, M.; Seppala, E. T.; Nieminen, R. M., Effect of gating and pressure on the electronic transport properties of crossed nanotube junctions: formation of a Schottky barrier. *J Phys Condens Matter* **2011,** *23*, 112203.

[17] Zhao, H.; Xie, J.; Mao, A.; Wang, A.; Chen, Y.; Liang, T.; Ma, D., Effects of Heating Mode and Temperature on the Microstructures, Electrical and Optical Properties of Molybdenum Thin Films. *Materials* **2018,** *11*, 1634.

[18] Tune, D. D.; Flavel, B. S., Advances in Carbon Nanotube-Silicon Heterojunction Solar Cells. *Adv. Energy Mater.* **2018,** *8*, 1703241.

[19] Harris, J. M.; Semler, M. R.; May, S.; Fagan, J. A.; Hobbie, E. K., Nature of Record Efficiency Fluid-Processed Nanotube-Silicon Heterojunctions. *J Phys Chem C* **2015,** *119*, 10295–10303.

[20] Harris, J. M.; Headrick, R. J.; Semler, M. R.; Fagan, J. A.; Pasquali, M.; Hobbie, E. K., Impact of SWCNT processing on nanotube-silicon heterojunctions. *Nanoscale* **2016,** *8*, 7969–7977.

[21] Cheung, S. K.; Cheung, N. W., Extraction of Schottky Diode Parameters from Forward Current-Voltage Characteristics. *Appl. Phys. Lett.* **1986,** *49*, 85–87.

[22] Rakhshani, A. E., Heterojunction properties of electrodeposited CdTe/CdS solar cells. *J. Appl. Phys* **2001,** *90*, 4265–4271.

[23] Han, B.; Gao, M.; Wan, Y.; Li, Y.; Song, W.; Ma, Z., Effect of post-annealing on the properties of thermally evaporated molybdenum oxide films: Interdependence of work function and oxygen to molybdenum ratio. *Mater Sci Semicond Process* **2018,** *75*, 166–172.

[24] Voroshazi, E.; Verreet, B.; Buri, A.; Müller, R.; Di Nuzzo, D.; Heremans, P., Influence of cathode oxidation via the hole extraction layer in polymer:fullerene solar cells. *Org. Electron* **2011,** *12*, 736–744.

[25] Li, X.; Jung, Y.; Goh, T.; Taylor, A. D., Device area scale-up and improvement of SWNT/Si solar cells using silver nanowires, *Adv. Energy Mater*. **2014**, 4, 1400186.

[26] Wang, F.; Kozawa, D.; Miyauchi, Y.; Hiraoka, K.; Mouri, S.; Ohno, Y.; Matsuda, K.; Fabrication of single-walled carbon nanotube/Si heterojunction solar cells with high photovoltaic performance, *ACS Photonics*, **2014**, 1, 360–364

[27] Miyadera, T.; Ogo, H.; Taima, T.; Yamanari, T.; Yoshida, Y., Analytical model for the design principle of large-area solar cells. *Sol. Energy Mater Sol. Cells* **2012,** *97*, 127–131.

[28] Gonzalo, V., A. Estrella, and M. Jose. "surface tension of alcohol+ water from 20 to 50 ºC." *J. Chem. Eng. Data* **1995**, 40, 611–614.

Chapter 3 Carbon nanotube/silicon heterojunction solar cell with the enhanced performance using MoO_x via rapid vapor deposition process

3.1 Introduction

As described in Chapter 2, the highly hydrophobic property of the carbon nanotube (CNT) film surface does not allow the MoO_x layer to form uniformly on the large area CNT film via simple spin-coating of a MoO_x precursor solution. Targeting uniform MoO_x layer onto large area CNT film, it is important to develop a simple, quick method for preparing MoO_x layer. Previous works [1–3] applied MoO_x powder as a source for the MoO_x deposition by thermal evaporation, but such method is unsuitable for scalable production because the uncontrollable surface area of the powder. In this chapter, this problem was solved while keeping things simple by rapid vapor deposition of MoO_x by using a pre-oxidated Mo boat as the source for MoO_x, where the Mo boat was thermally annealed in an oxidation-rich gas (air). As-deposited MoO_x layer significantly enhanced the power conversion efficiency (PCE) of the small-sized CNT/n-Si solar cell (active area of 0.0314 cm^2) from 7.1% to 9.2%, and then further improved to 11.1% by heating the CNT/n-Si substrate during the deposition process. For the large cell fabrication (active area of 4.0 cm^2), as-deposited MoO_x layer helps in preventing the metal grid and Si from coming into direct contact. As a result, a PCE of 3.6% of the large-sized cell was realized, which was 177% improvement from the original value (1.3%).

3.2 Experiments

3.2.1 Preparation of CNT films and MoO_x layer

CNT films were prepared following the method described in experimental section in Chapter 2. The MoO_x layer deposited on the substrate following the method below (Fig. 3.1). The boat (99.95%, Nilaco, Japan) was first thermally annealed in air at 600 ℃ for 1~3 min for oxidation (Appendix, Fig. 3.1 a). And then the pre-oxidized Mo boat was resistively heated at 1200 ℃ under vacuum of 10^{-4} Pa for depositing MoO_x layer on target substrate (Appendix, Fig. 3.1b). The whole deposition process will be finished in 10 –15 s. The color of the surface of the Mo boat changed from shiny to dark black after thermally annealing, and then recovered to shiny again after rapid vapor deposition process (Appendix, Fig. S3.1). The as-deposited MoO_x layer on the SiO_2/Si substrate showed uniform color within each sample (Appendix, Fig. S3.2). The weight of the synthesized MoO_x on the Mo boat was proportional to the thermally annealing time (Appendix, Fig. S3.3a). And the MoO_x thickness was roughly controlled by the weight of the deposited MoO_x from the pre-oxidized Mo boat (Appendix, Fig. S3.3b).

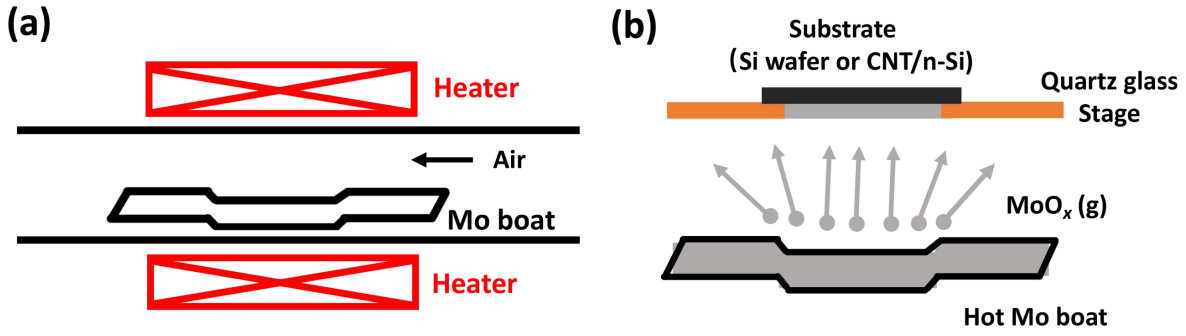

Fig. 3.1. Schematic representing (a) the thermally annealing process of the Mo boat in air and (b) the rapid vapor deposition process of the pre-oxidized Mo boat for MoO_x layer under vacuum of 10^{-4} Pa.

3.2.2 Fabrication of solar cells and characterization

n-Type Si (n-Si) (100) wafers of resistance (1–5 Ω cm) with a circular opening (diameter of 2 mm, defined by 500 nm SiO_2 layer) were used to fabricate the small-sized solar cells. n-Si (100) wafers of resistance (1–2 Ω cm) were applied to fabricate the large-sized solar cells. The native SiO_2 layer was removed away by 4.7wt% hydrofluoric (HF) aqueous acid solution. The CNT/n-Si heterojunction was formed by carefully picking up the CNT film from the water with n-Si wafer and then drying it in a vacuum oven (100 ℃) for 3 min. The MoO_x layer was deposited onto the CNT film in the CNT/n-Si heterojunction using the pre-oxidated Mo boat via the rapid vapor deposition method, which was processed by resistively heating the pre-oxidated Mo boat at 1200 ℃ and 10^{-4} Pa. For the small-sized solar cells, a rear Al full contact cathode was sputter-deposited using DC magnetron sputtering apparatus, while a top Au electrode (100 nm in thickness) was deposited by using DC magnetron sputtering. For the large-sized solar cells, a full contact rear Al cathode (500 nm in thickness) was deposited using DC magnetron sputtering, while a top Ag anode (300 nm in thickness, 9 figures connected to a busbar, Chapter 2, Appendix, Fig. S2.2a) was made by thermal evaporation using a lithography-made Ni foil mask. The illumination area (4.0 cm^2) of solar cells was precisely determined (Chapter 2, Appendix, Fig. S2.2b).

The weight of the Mo boat was measured using electronic scales. Four solar cells were fabricated under identical conditions. The photovoltaic (PV) performance of solar cells was evaluated using a solar cell evaluation system (JASCO YQ-2000, Japan) under AM 1.5 (P_{input}= 100 mW cm^{-2}) at 25 ℃. X-ray photoelectron spectroscopy (XPS, JPS-9010TR) with Al Kα source (1486.6 eV) was applied to analyze the as-prepared MoO_x layer on SiO_2/Si substrate. The binding energy was calibrated by fixing C 1s binding energy at 284.6 eV. The surface morphologies of the as-prepared MoO_x layer on SiO_2/Si substrate was observed using the scanning electron microscopy (SEM, Hitachi S-4800, Tokyo, Japan). The atomic force

microscopy (AFM; SPM-9600, Shimadzu, Japan) using Si cantilever with a sharpened tetrahedral tip (tip radius of 7±3 nm) (Olympus OMCL-AC240TS-C3, Tokyo, Japan) with resonant frequency of 70 kHz and spring constant of 2 N/m was used to evaluate the surface microstructure of as-prepared MoO_x layer on SiO_2/Si substrate. The crystal structure of the as-prepared MoO_x thin film on SiO_2/Si substrate was analyzed by X-ray diffraction (XRD; Rigaku RINT-Ultima III, Akishima, Japan) with a Cu Kα source.

3.3 Results and discussion

3.3.1 Characterization of deposited MoO_x layer

The Mo 3d core level XPS data of the prepared MoO_x film showed two oxidation states for Mo (Fig. 3.2a), where the major components, Mo^{6+} $3d_{5/2}$ and Mo^{6+} $3d_{3/2}$, were observed at 232.8 eV and 235.8 eV, and the minor components, Mo^{5+} $3d_{5/2}$ and Mo^{5+} $3d_{3/2}$, were observed at 231.5 eV at 234.3 eV [4]. The as-prepared MoO_x thin film showed an O/Mo atomic ratio of 2.84, which demonstrated that the as-prepared MoO_x thin film was a sub-stoichiometric molybdenum trioxide (MoO_x, $x<3$). Thus, I used MoO_x ($x<3$) as the as-prepared molybdenum oxides in this chapter. The XRD pattern showed the broad halo patterns, and some MoO_x peaks at (170) (221) (112), which indicates the deposited MoO_x was almost amorphous and partially crystallized (Fig. 3.2b). The SEM and AFM were used to analyze the surface microstructure of the as-prepared MoO_x thin film on the SiO_2/Si substrate. The as-prepared MoO_x layer with a uniform distribution on the SiO_2/Si substrate was observed (Fig. 3.2c). The root-mean-square (RMS) roughness of the MoO_x film surface was estimated to 0.71 nm (Fig. 3.2d), indicating the obtained MoO_x film was smooth.

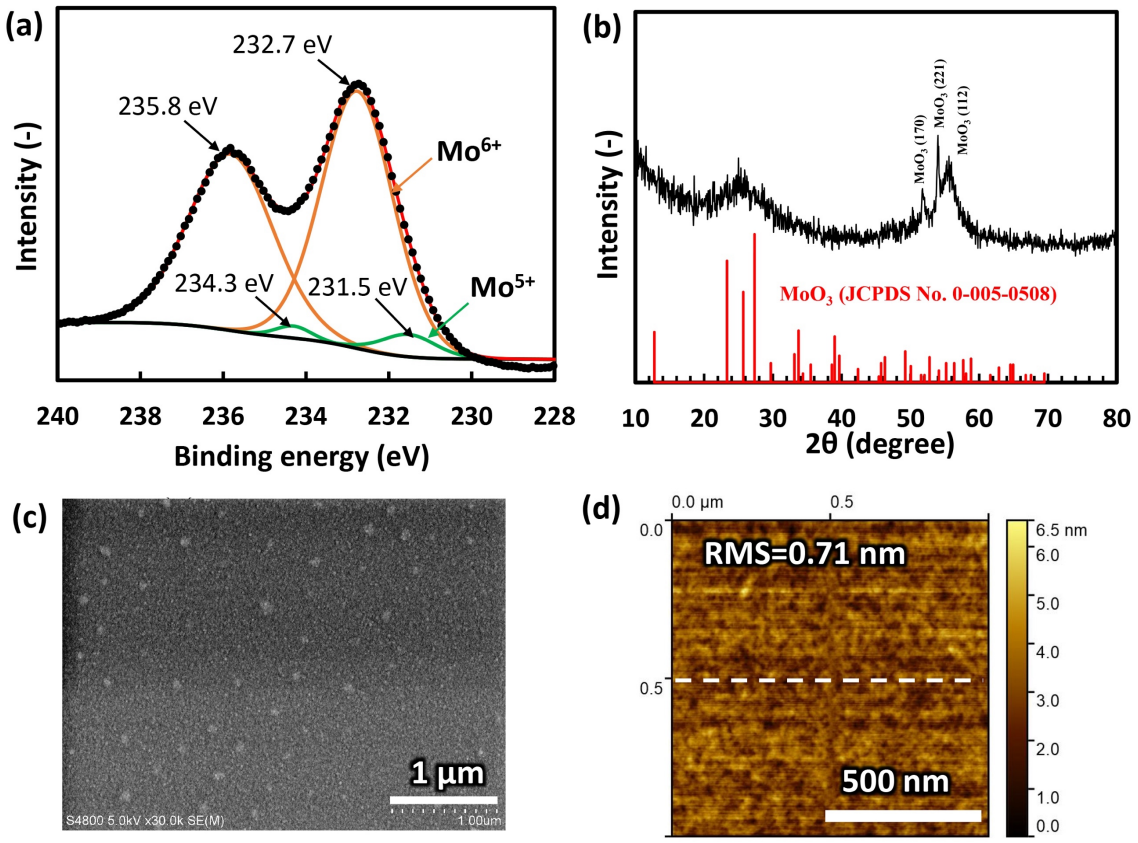

Fig. 3.2. (a) The Mo 3d core level X-ray photoelectron spectroscopy (XPS) spectrum in the deposited MoO_x film. (b) X-ray diffraction (XRD) pattern of the as-prepared MoO_x layer on a SiO_2/Si substrate. (c) Top-view scanning electron microscopy (SEM) image of the deposited MoO_x film on a SiO_2/Si substrate. (c) Atomic force microscopy (AFM) image of the deposited MoO_x film on SiO_2/Si substrate. The MoO_x layer with a thickness ~ 30 nm was used in each measurement.

3.3.2 PV performance of the small-sized (0.0314 cm^2) solar cells

The influence of the MoO_x thickness on PV performance of the MoO_x–CNT/n-Si solar cell was first investigated. The optimized MoO_x thickness was 30 nm (Fig. 3.3a, b). The MoO_x–CNT/n-Si solar cell with the best PCE of 9.3% was achieved (Fig. 3.3a). The average PCE of four solar cells was 9.2% with a standard deviation of 0.2% (Appendix, Fig. S3.4 and Table. S3.1). Using thicker MoO_x layer for solar cell fabrication led to the decreased short circuit current density (J_{sc}) and fill factor (FF) (Fig. 3.3b). This is probably due to the higher absorption of the incident light and/or inhibition of the electric transport in the CNT film with top electrode

by thicker and highly resistive MoO_x. Because the overall PV performance of the MoO_x–CNT/n-Si is still undesirable, further enhancement for its PCE is needed. Then further improvement of the PCE of MoO_x–CNT/n-Si solar cell was explored by heating the CNT/n-Si substrate during MoO_x deposition process. The optimized substrate temperature was 300 °C. This resulted in the PCE improved dramatically from 9.2% to 11.1% (Fig. 3.3c, d), which is attributed to the enhanced J_{sc} value from 27.4 to 34.8 mA/cm^2, and FF value from 0.62 to 0.64. (Appendix, Fig. S3.5 and Table. S3.2). The higher substrate temperature resulted in the decrease in PCE of the cells because of the reduced FF, J_{sc} and open circuit voltage (V_{oc}) (Fig. 3.3d), which are probably due to the increased oxygen vacancy in the as-deposited MoO_x [5-8].

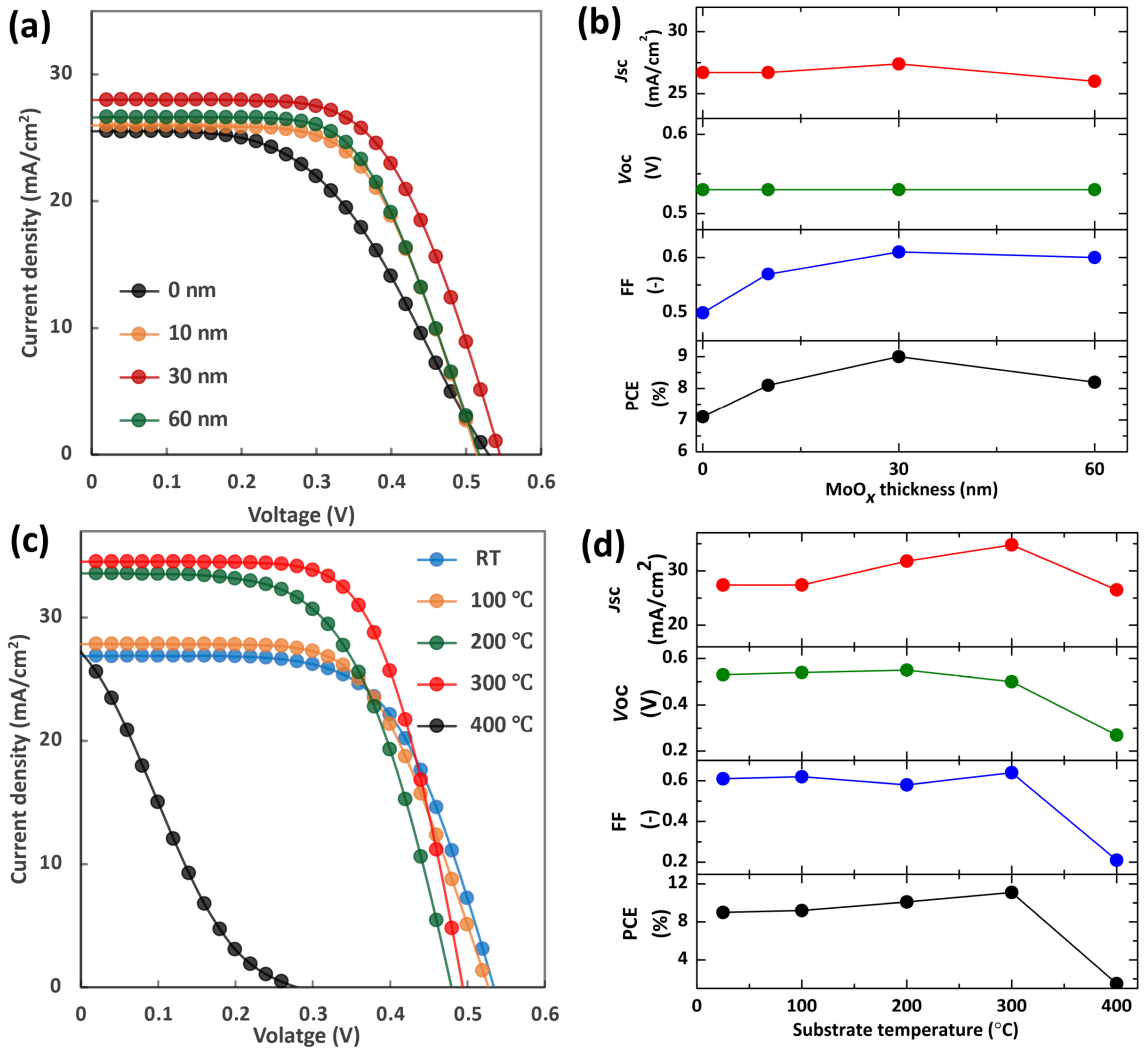

Fig. 3.3. (a) *J–V* curves and (b) PV parameters as a function of MoO_x thickness. (c) *J–V* curves and (d) PV parameters as a function of substrate temperature.

Then, the small-sized CNT/n-Si solar cells (0.0314 cm^2) fabricated with/without MoO_x layer was compared (Fig. 3.4). The pristine CNT/n-Si solar cells showed a poor PV performance (J_{sc}: 26.7 mA/cm^2, V_{oc}: 0.53 V, FF: 0.50, PCE: 7.1%) (black line, Fig. 3.4b). The schematic diagram of the MoO_x–CNT/n-Si solar cells was presented in Fig. 3.4a. Based on such structure and the optimized experiment conditions, the PCE of the cell was significantly improved from 7.1 % to 11.1% (red line, Fig. 3.4b), which is 56% improvement from the original value. The enhanced PCE is mainly contributed from higher J_{sc} value of 34.8 mA/cm^2, V_{oc} value of 0.5 V and FF value of 0.64 (Fig. 3.4b), indicating that the MoO_x acted as an enhancer for anti-reflection effect of CNT film for increasing the absorption of incident light and as an efficient

dopant for reducing the sheet resistance of the CNT film. Moreover, the color of the active area of solar cell changing from blight gray to dark gray after depositing the MoO_x (Fig. 3.4c) also evidenced the enhanced anti-reflection effect by the MoO_x–CNT composite layer.

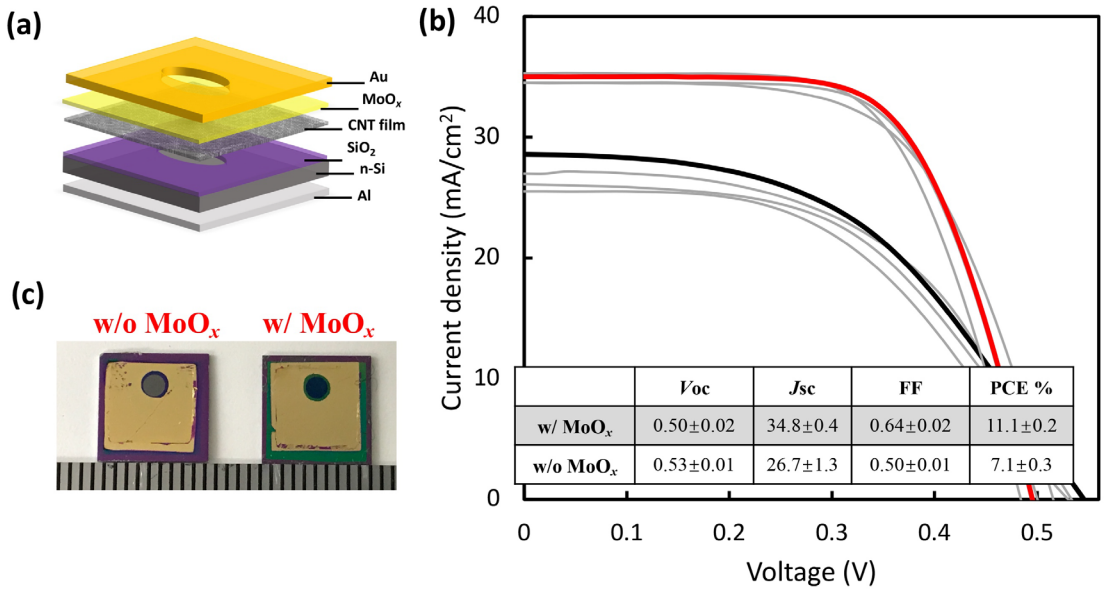

	Voc	*Jsc*	FF	PCE %
w/ MoO_x	0.50±0.02	34.8±0.4	0.64±0.02	11.1±0.2
w/o MoO_x	0.53±0.01	26.7±1.3	0.50±0.01	7.1±0.3

Fig. 3.4. (a) Schematic diagram of the structure of the MoO_x–CNT/n-Si solar cell (0.0314 cm^2). (b) *J–V* curves of CNT/n-Si solar cells with and without MoO_x layer; inset table shows the detailed parameters of pristine CNT/n-Si solar cells and MoO_x–CNT/n-Si solar cells with standard deviation. (c) Digital image of CNT/n-Si solar cells with and without MoO_x.

3.3.3 PV performance of large-sized (4.0 cm^2) solar cells

For fabrication of the large-sized CNT/Si solar cells, it is important to deposit a metal grid on the CNT film to collect the generated charge carriers over long distance and decrease the power loss caused by the sheet resistance of the CNT film. However, the metal grid can directly contact with Si through the pores in the CNT film, which leads to severe current leakage. Therefore, depositing a MoO_x layer onto the CNT film in CNT/Si heterojunction is expected to suppress the current leakage by preventing the metal grid and Si coming into contact (Fig. 3.5a). The large-sized MoO_x–CNT/n-Si solar cells were fabricated following the same optimized experimental conditions in the small-sized solar cell. The pristine CNT/n-Si solar

cell (J_{sc}: 18.1 mA/cm^2; V_{oc}: 0.34 V; FF: 0.21; PCE: 1.3%) was considerably worse than the MoO_x-CNT/n-Si solar cell (J_{sc}: 24.3 mA/cm^2; V_{oc}: 0.40 V; FF: 0.38; PCE: 3.7%) (Fig. 3.5c). This is due to the severe current leakage that is caused by the directly contact between the Ag grid and n-Si substrate. The current leakage was suppressed after deposition of MoO_x because the MoO_x layer could work as a physical blocking layer that prevents the direct contact between the Ag grid and n-Si. The color of the solar cell changed to dark bule after depositing MoO_x, which evidences that the MoO_x acted as an enhancer for antireflection effect of the CNT film. This is consistent with the J_{sc} increased from 17.9 to 25.0 mA/cm^2.

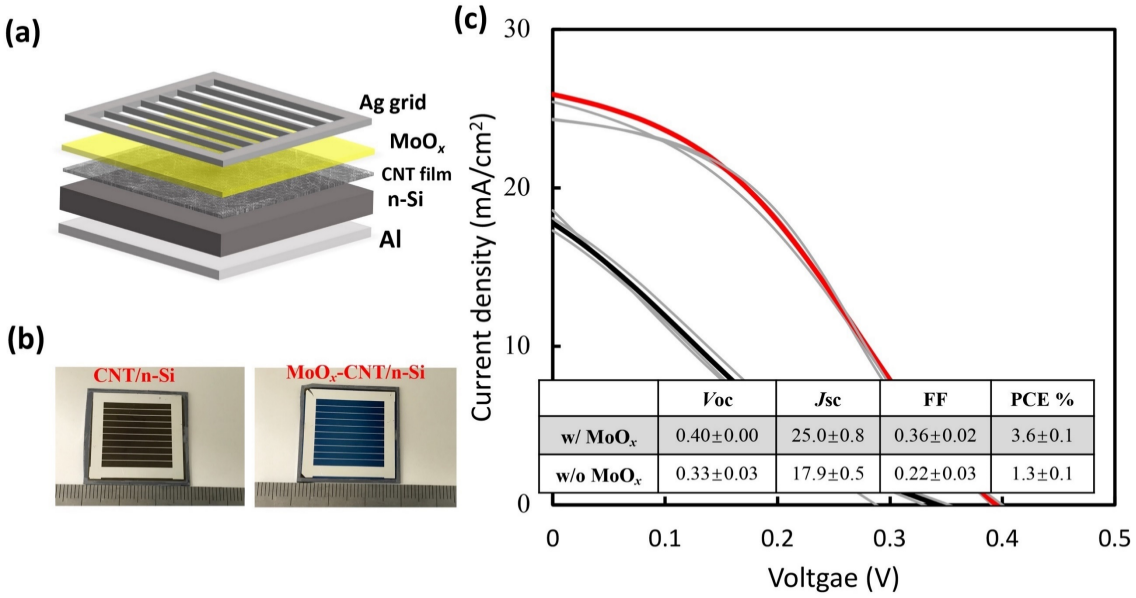

Fig. 3.5. (a) Schematic diagram of the structure of MoO_x–CNT/n-Si solar cell (4.0 cm^2). (b) Digital image of solar cells with and without MoO_x. (c) *J–V* curves of the solar cells with and without MoO_x layer; inset table shows the detailed parameters of the pristine CNT/n-Si solar cells and the MoO_x–CNT/n-Si solar cells with standard deviation.

3.3.4 Rate analysis of the MoO_x deposition via rapid vapor deposition

The synthesized MoO_x on Mo boat was evaporated completely in 15 s at 1200 ℃ under pressure of 10^{-4} Pa. The MoO_x layer thickness mainly depends on the amount of evaporated MoO_x from the pre-oxidized Mo boat. Therefore, the rate of the MoO_x deposition is carefully

analyzed to make accurate control of the MoO_x thickness. The relationship of vapor pressure and temperature is given by Antoine Equation (1) [9]:

$$log_{10}(p) = A - \frac{B}{C+T}, \quad (1)$$

Where the p is the vapor pressure, T is temperature, and A, B, and C are Antoine coefficients specific to the substance. In the case of substance (MoO_x), the values of 2.6, 2137.4 and -616.5 are obtained for A, B, and C, respectively, from reference [10]. The minimum evaporation temperature of MoO_x is estimated to be 938 K (665 ℃) under vacuum of 10^{-4} Pa. Therefore, the pre-oxidated Mo boat was resistively heated at 700 ℃ under pressure of 10^{-4} Pa for depositing MoO_x layer and recorded the color change and weight change of the Mo boat over time (Appendix, Fig. S3.6). The weight change was about 93% of its original value in the initial 20 s (Fig. 3.6a) and the whole deposition process was almost finished in the initial 10 s even at the minimum evaporation temperature of 700 ℃. The estimated MoO_x deposition rate was about 6.5 nm/s at the initial stage (10 s) and then rapidly reduced to below 0.2 nm/s (Fig. 3.6c). There results demonstrated that the method presented in this work is too fast to make careful control over the thickness in the batch process. But in future, this difficulty can be solved by integrating the rapid vapor deposition of MoO_x layer with roll-to-roll technology, where the MoO_x thickness would be accurately controlled by the sample carrying speed, as shown in Fig. 3.6c.

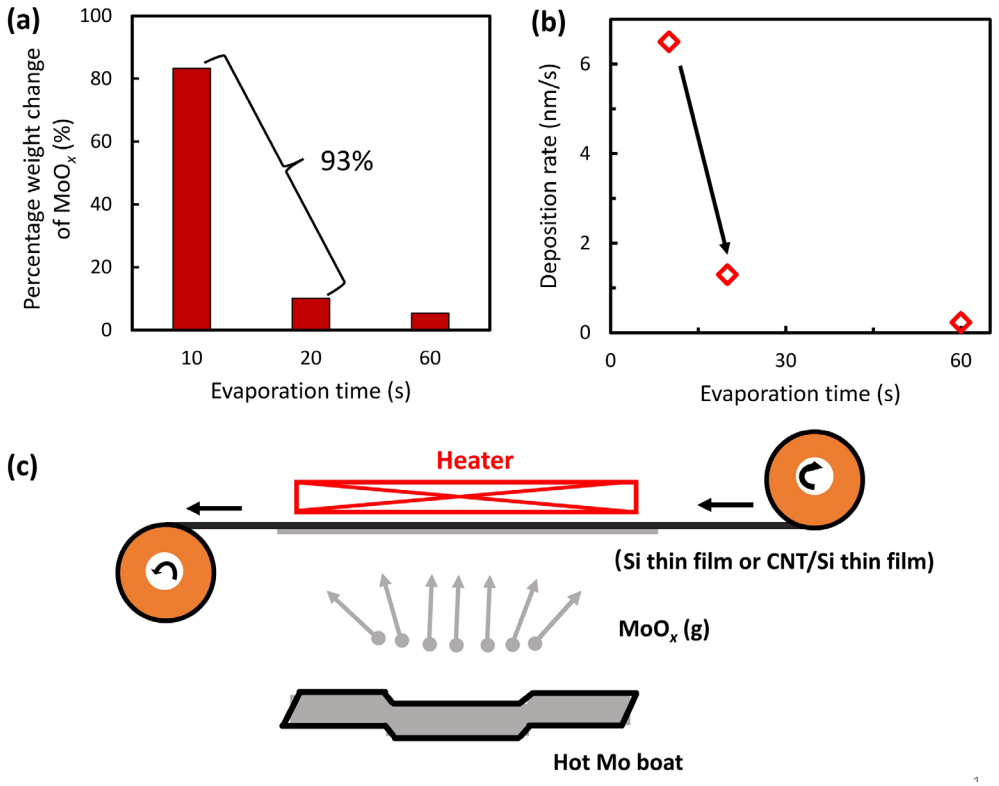

Fig. 3.6. (a) Percentage of weight change of MoO_x over the time. (b) Average deposition rate of MoO_x layer over the time. (c) Schematic diagram of the rapid vapor deposition of MoO_x layer with roll-to-roll technology for Si thin film or CNT/Si thin film.

3.4 Conclusions

In this chapter, a new method was developed to deposit the MoO_x layer, where a pre-oxidized Mo boat was resistively heated at 1200 °C under vacuum of 10^{-4} Pa for thermal evaporation of MoO_x layer. Such method is advantageous in comparison with the previous vapor deposition method using MoO_3 powder because of the well-controlled surface area and compatibility with the substrate heating during MoO_x deposition, which may skip the long-time post-thermal annealing process. The as-deposited MoO_x layer significantly enhanced the PV performance of the small- (0.0314 cm^2) and large-sized (4.0 cm^2) solar cells. The MoO_x–CNT/n-Si solar cells with active areas of 0.0314 and 4.0 cm^2 showed PCE of 11.1 % and 3.6 %, respectively. Moreover, the rate of MoO_x deposition via rapid vapor deposition was analyzed and it was found that the whole evaporation process was too fast to make careful control over the MoO_x

thickness in the batch process. But in future, this difficulty could be solved by integrating with the rapid vapor deposition of MoO_x layer with roll-to-roll technology, where the MoO_x thickness would be accurately controlled by the sample carrying speed.

Appendix

Table. S3.1. The detail PV parameters of MoO_x–CNT/n-Si solar cells fabricated using the MoO_x layer with different thickness.

Thickness (nm)	J_{SC} (mA/cm^2)	V_{OC} (V)	FF (-)	PCE (%)
0	26.7 ± 1.3	0.53 ± 0.01	0.50 ± 0.01	7.1 ± 0.3
10	26.7 ± 1.2	0.53 ± 0.01	0.57 ± 0.03	8.1 ± 0.1
30	27.4 ± 0.5	0.53 ± 0.01	0.61 ± 0.01	9.0 ± 0.1
60	26.0 ± 0.6	0.53 ± 0.01	0.60 ± 0.01	8.2 ± 0.3

Table. S3.2. The detail PV parameters of the MoO_x–CNT/n-Si solar cells fabricated using the MoO_x layer deposited at various CNT/n-Si substrate temperature.

Temperature (°C)	J_{SC} (mA/cm^2)	V_{OC} (V)	FF (-)	PCE (%)
RT	27.4 ± 0.5	0.53 ± 0.01	0.61 ± 0.01	9.0 ± 0.1
100	27.4 ± 0.5	0.54 ± 0.00	0.62 ± 0.01	9.2 ± 0.2
200	31.8 ± 1.1	0.55 ± 0.02	0.58 ± 0.02	10.1 ± 0.2
300	34.8 ± 0.4	0.50 ± 0.02	0.64 ± 0.02	11.1 ± 0.2
400	26.5 ± 2.0	0.27 ± 0.01	0.21 ± 0.01	2.5 ± 0.2

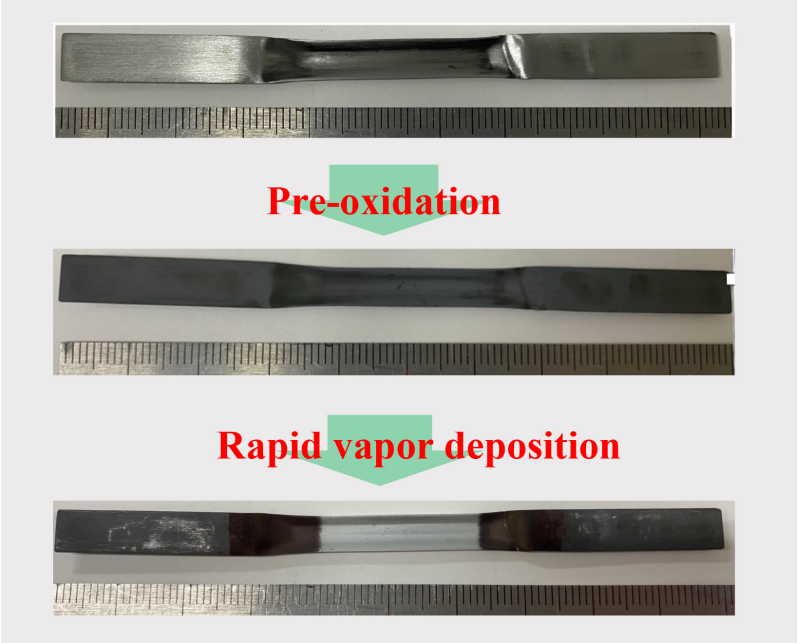

Fig. S3.1. Digital images of purity Mo boat, pre-oxidized Mo boat and rapid vapor deposited Mo boat.

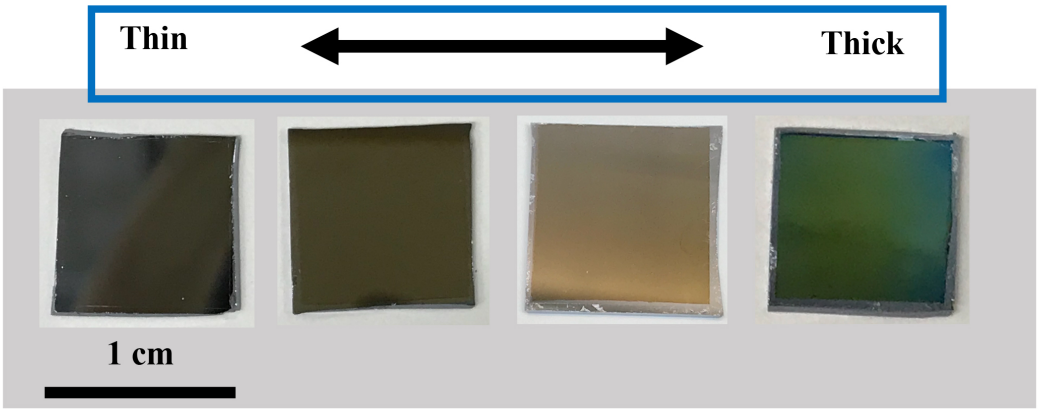

Fig. S3.2. As-deposited MoO_x layer with various thickness on SiO_2/Si substrate.

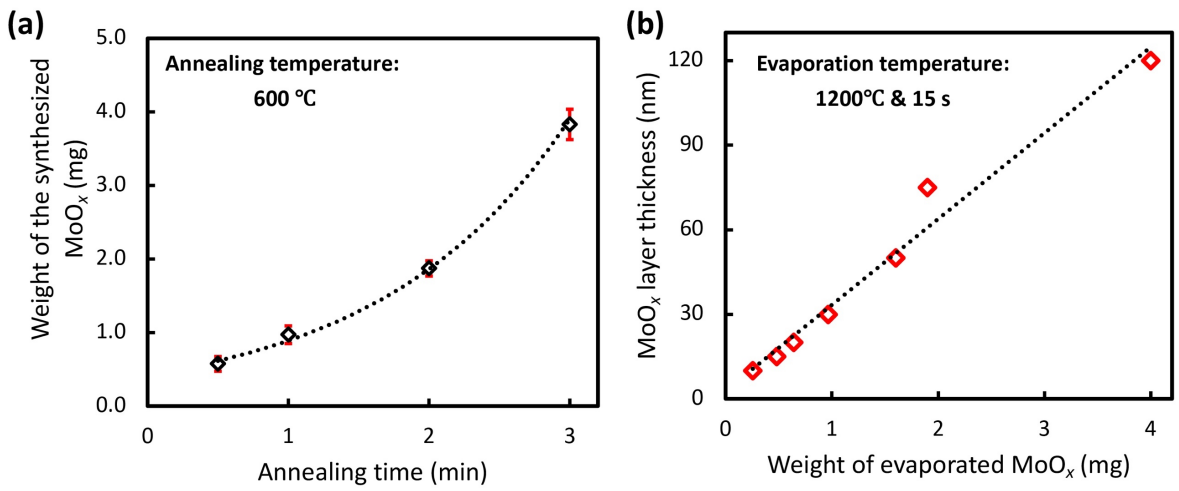

Fig. S3.3. (a) The relationship between the weight of the synthesized MoO_x with the thermally annealing time at 600 °C in air. (b) The relationship between the MoO_x layer thickness and the weight of the evaporated MoO_x.

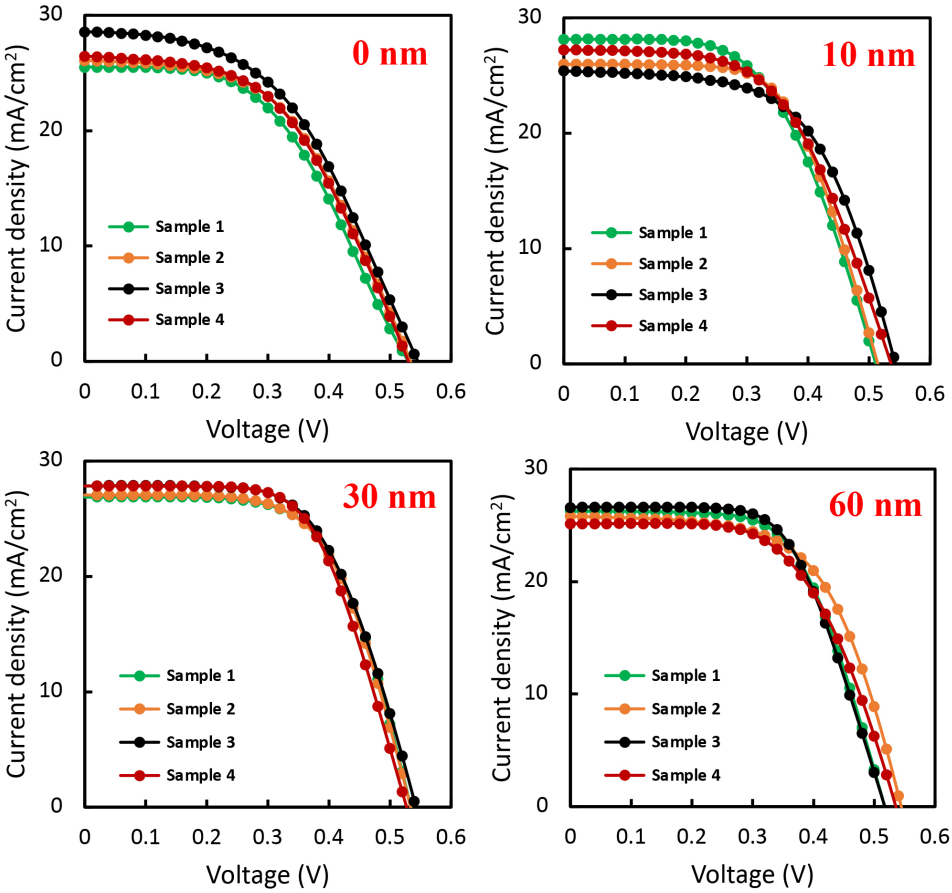

Fig. S3.4. *J–V* curves of the CNT/n-Si heterojunction solar cells fabricated using MoO_x layer with various thickness.

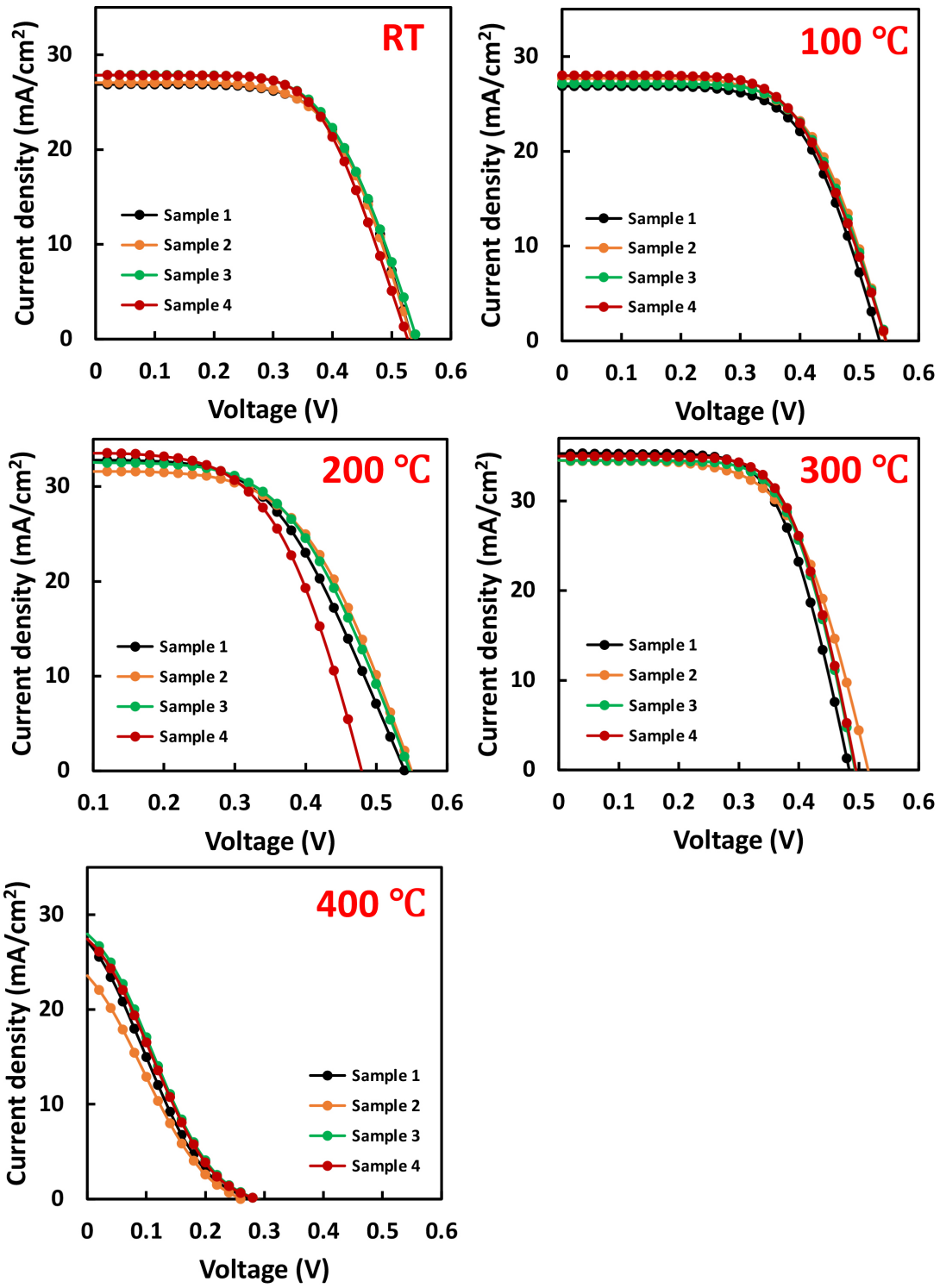

Fig. S3.5. ***J–V*** **curves of the MoO_x–CNT/n-Si heterojunction solar cells heat treated at various substrate temperatures, where the CNT/n-Si substrate was heated during the MoO_x deposition process.**

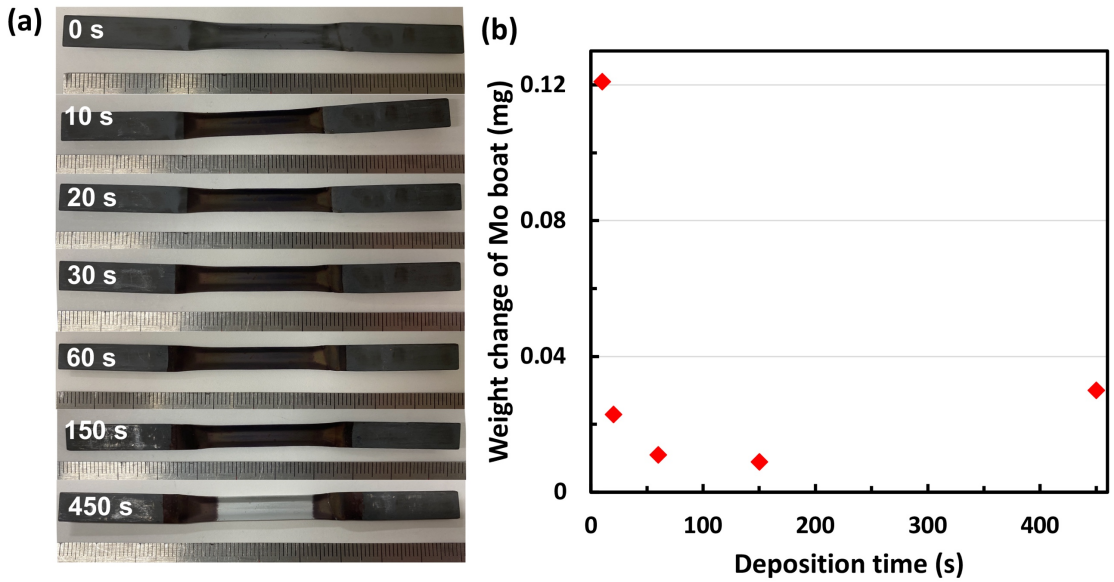

Fig. S3.6. (a) Digital image of color change of the pre-oxidized Mo boat with the deposition time. (b) Weight change of pre-oxidized Mo boat with the deposition time.

References

[1] Hellstrom, S. L.; Vosgueritchian, M.; Stoltenberg, R. M.; Irfan, I.; Hammock, M.; Wang, Y. B.; Jia, C.; Guo, X.; Gao, Y.; Bao, Z., Strong and stable doping of carbon nanotubes and graphene by MoOx for transparent electrodes. *Nano Lett* **2012,** *12*, 3574–80.

[2] Jeon, I.; Cui, K.; Chiba, T.; Anisimov, A.; Nasibulin, A. G.; Kauppinen, E. I.; Maruyama, S.; Matsuo, Y., Direct and Dry Deposited Single-Walled Carbon Nanotube Films Doped with MoOx as Electron-Blocking Transparent Electrodes for Flexible Organic Solar Cells. *J Am Chem Soc* **2015,** *137*, 7982–7985.

[3] Esconjauregui, S.; D'Arsie, L.; Guo, Y. Z.; Yang, J. W.; Sugime, H.; Caneva, S., Efficient Transfer Doping of Carbon Nanotube Forests by MoO3. *ACS Nano* **2015,** *9*, 10422-10430.

[4] Chastain, J.; King Jr, R. C., Handbook of X-ray photoelectron spectroscopy. *Perkin-Elmer Corporation* **1992,** *40*, 221.

[5] Han, B.; Gao, M.; Wan, Y.; Li, Y.; Song, W.; Ma, Z., Effect of post-annealing on the properties of thermally evaporated molybdenum oxide films: Interdependence of work function and oxygen to molybdenum ratio. *Mater Sci Semicond Process* **2018,** *75*, 166–172.

[6] Wilkes, G.C. Gupta, M.C.., Laser Annealing of Carrier-Selective MoOx Layers for Silicon Solar Cells. *2020 47th IEEE Photovoltaic Specialists Conference (PVSC)* **2020,** 2453–2455**.**

[7] Scirè, D.; Procel, P.; Gulino, A.; Isabella, O.; Zeman, M.; Crupi, I., Sub-gap defect density characterization of molybdenum oxide: An annealing study for solar cell applications. *Nano Research* **2020,** *13*, 3416–3424.

[8] Wang, W.; Huan, X.; Wang, C., Temperature-induced degradation of bilayer MoOx-based solar absorbers under air annealing conditions. *Surf. Interfaces* **2020,** *21*. 100654.

[9] Thomson, G. W., The Antoine equation for vapor-pressure data. *Chem Rev* **1946,** *38*, 1-39.

[10] Stull, D. R., Vapor pressure of pure substances. Organic and inorganic compounds. *Ind Eng Chem* **1947,** *39*, 517–540.

Chapter 4 Carbon nanotube/silicon heterojunction solar cell with an active area of 4 cm^2 realized using a multifunctional MoO_x layer

The part of the content of this Chapter has been published by Xiaoxu HUANG, et al., Carbon nanotube/silicon heterojunction solar cell with an active area of 4 cm^2 realized using a multifunctional MoO_x layer, Carbon, 185, 215–223 (2021).

4.1 Introduction

In this chapter, a CNT/Si solar cell with improved efficiency and an enlarged size was developed using MoO_x as a multifunctional layer, which provided the efficient p-type doping of the CNTs, the enhanced AR effect of the CNT layer, and the essential role as the blocking layer between the Si substrate and the metal grid electrode. The hot-wire oxidation–sublimation deposition method [1] was adopted for the deposition of MoO_x onto the CNT film, which proceeded by resistively heating a Mo wire in a low-pressure O_2/Ar gas mixture. By combining the MoO_x layer with a Ag grid electrode, a 4 cm^2-sized CNT/n-Si heterojunction solar cell was fabricated. The MoO_x layer can block the direct contact between Ag and Si while allowing the electrical contact between Ag and the CNTs. The MoO_x layer thickness was carefully optimized, and a PCE of 5.2% was realized. Heat treatment was then applied to the MoO_x–CNT/n-Si heterojunction, which enhanced the PCE to 9.1%. Finally, the PCE was improved to 10.0% by adding an AR layer of polymethyl methacrylate (PMMA). The possible mechanism of performance enhancement was also investigated.

4.2 Experiments

CNT films were prepared following the method described in experimental section in Chapter 2. The MoO_x layer deposited on the substrate following the method below (Fig. 4.1).

The whole fabrication process for solar cell is summarized in Fig. 4.1. n-Type, (100)-oriented Si wafers (Czochralski method, 1–2 Ω cm) with thicknesses of 625±10 μm were used to fabricate the solar cell. The Si wafers were etched in a 4.7 wt% aqueous solution of HF for 5 min to remove the native SiO_2 layer. The CNT/n-Si heterojunction was formed by carefully removing the CNT film from the water surface with the n-Si wafer and then drying it in a vacuum oven (100 °C, 3 min). Subsequently, the MoO_x thin film was deposited onto the CNT film in the CNT/n-Si heterojunction using a Mo wire (purity of 99.99%, diameter of 0.5 mm) via the hot-wire oxidation–sublimation deposition method [1], which proceeded by resistively heating the Mo wire to 927 ± 20 °C under a 5 vol% O_2/Ar gas mixture at 1 Pa and 10 sccm. Then, a rear Ag cathode (500 nm in thickness) was formed by thermal evaporation, while a top Ag anode (300 nm in thickness, 21×2 fingers connected to a busbar, Fig. 4.1a) was formed by thermal evaporation using a lithography-made Ni foil mask. A shadow mask made of Cu foil (Fig. 4.1b) was used during the PCE measurements to precisely define the illumination area (409 mm^2, Fig. 4.1c). For some cells, an AR layer of PMMA was formed on top of the MoO_x layer. PMMA powder (Wako, Tokyo, Japan) was dissolved in toluene (Wako, Tokyo, Japan) by stirring for >30 min at 75 °C, and the resulting PMMA solution (1–4 wt%) was spin-coated onto the MoO_x-CNT/n-Si cells at 6,000 rpm for 60 s. The cells were then dried at 120 °C under vacuum for approximately 1 h. n-Type Si (n-Si) (100) wafers of resistance (1–5 Ω cm) with a circular opening (diameter of 2 mm, defined by 500 nm SiO_2 layer) were used to fabricate the small-sized solar cells. A rear full contact Ag cathode (500 nm in thickness) and a top Ag anode (300 nm in thickness) was formed by thermal evaporation.

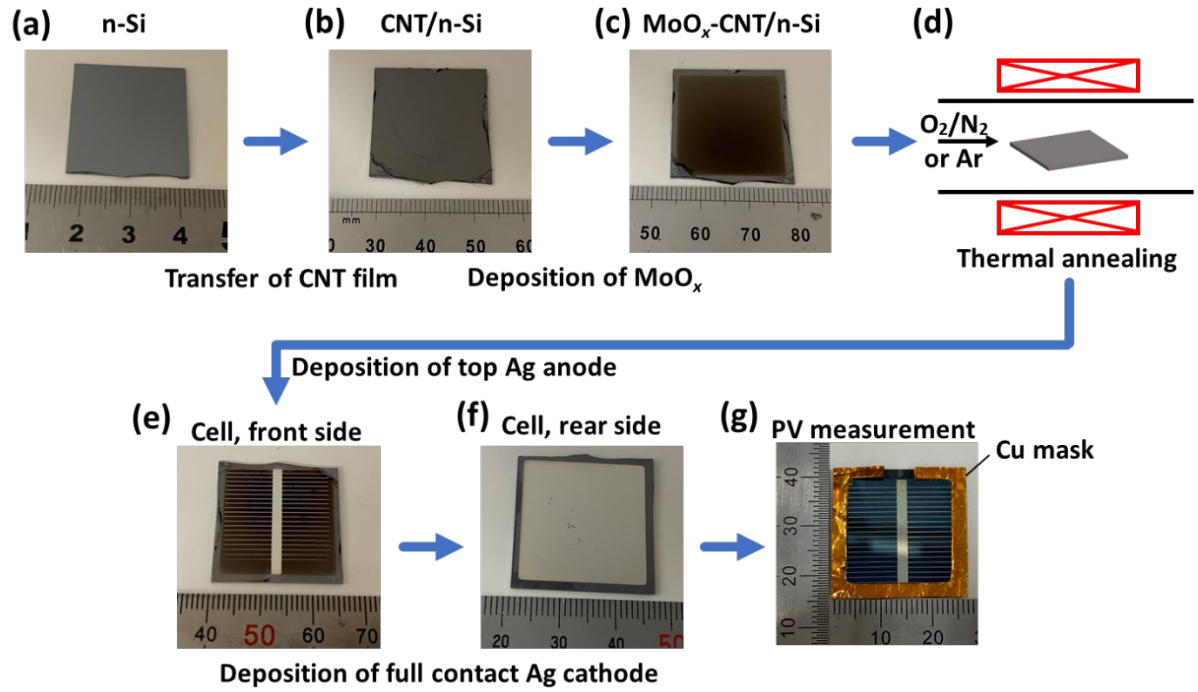

Fig. 4.1. Entire fabrication process of the MoO_x–CNT/n-Si solar cell. (a)–(b) Transfer of the CNT film onto the bare n-Si wafer. (b)–(c) Deposition of the MoO_x layer onto CNT/n-Si. (c)–(d) Thermally annealing of MoO_x–CNT/n-Si. (d)–(f) Evaporation of the top Ag grid anode and rear Ag full-contact cathode. (g) PV measurements using a Cu mask that defines the illumination area.

All of the solar cells were evaluated by *J*–*V* curves using a solar cell evaluation system (JASCO YQ-2000, Tokyo, Japan) under standard test conditions of AM 1.5 (P_{input}=100 mW cm^{-2}) and 25 °C. The external quantum efficiency (EQE) measurements were performed using a CEP-2000 integrated system (Bunko-Keiki, Tokyo, Japan) with a Xe lamp attached to a monochromator (300–1200 nm). The microstructures of the CNT film and the MoO_x-CNT film on the Si substrate with a native oxide layer were characterized by scanning electron microscopy (SEM; Hitachi S-4800, Tokyo, Japan) alongside energy dispersive X-ray spectrometry (EDS; AMETEK EDAX Genesis, Berwyn, PA, USA). Atomic force microscopy (AFM; SPM-9600, Shimadzu, Kyoto, Japan) was also employed, which used a Si cantilever with a sharpened tetrahedral tip (tip radius of 7 ± 3 nm) (Olympus OMCL-AC240TS-C3,

Tokyo, Japan), a resonant frequency of 70 kHz, and a spring constant of 2 N/m. X-ray photoelectron spectroscopy (XPS; JEOL JPS-9010TR, Akishima, Japan) with an Al Kα source (1486.6 eV) and ultraviolet photoelectron spectrometer (UPS, ULVAC-PHI, VersaProbe2) with a resolution of ~0.1 eV were used to respectively analyze the chemical state and work function of the CNT, MoO_x, and MoO_x–CNT films. The binding energy was calibrated by fixing the C 1s signal that represented ambient contaminants to 284.6 eV. Ultraviolet-visible (UV-Vis) spectrophotometry (JASCO V-630, Tokyo, Japan) and the four-point probe method were used to measure the optical transmittance and sheet resistance, respectively, of the MoO_x, MoO_x–CNT, and CNT films prepared on quartz glass substrates (0.5 mm in thickness). The deposition rate of MoO_x was determined by depositing MoO_x on SiO_2/Si substates and measuring the thickness using a stylus profiling system (Dektak XT-S, Bruker, Billerica, MA, USA). Surface reflectivity measurements were conducted for bare n-Si, CNT/n-Si, MoO_x–CNT/n-Si, and PMMA/MoO_x–CNT/n-Si using a UV-Vis spectrophotometer (Perkin Elmer Lambda 650, Waltham, MA, USA). The crystal structure of the as-prepared MoO_x thin film on a SiO_2/Si substrate was analyzed by X-ray diffraction (XRD; Rigaku RINT-Ultima III, Akishima, Japan) with a Cu Kα source.

4.3 Results and discussion

4.3.1 Preparation and characteristics of MoO_x layer.

Previous works [2–3] used MoO_3 powder as the source for the thermal evaporation of MoO_x and for MoO_3 deposition, but the repeatability was found poor owing to the uncontrollable surface area of the powder. Recently, Li et al. reported an alternative method, the hot-wire oxidation–sublimation deposition method, in which a Mo wire was resistively heated and reacted with O_2 to generate MoO_x vapor [1]. This method enables the control of the MoO_x deposition rate through the regulation of the feed rate of O_2; furthermore, it can be scaled up

by using multiple Mo wires. Thus, this method was adopted for the present study. The MoO_x layer deposited at a rate of ~3 nm/min on a SiO_2/Si substrate using the apparatus shown in Fig. 4.2a had high thickness uniformity over a large area (> 4 cm^2) (Fig. S4.1). The MoO_x films showed uniform color within each sample, with optical transmittances decreasing with thickness (Fig. 4.2b). The Mo 3d core level XPS data showed two oxidation states for Mo (Fig. 4.2c), where the major components, Mo^{6+} $3d_{5/2}$ and Mo^{6+} $3d_{3/2}$, were noted at 232.6 eV and 235.8 eV and the minor components, Mo^{5+} $3d_{5/2}$ and Mo^{5+} $3d_{3/2}$, were observed at 231.7 eV and 234.9 eV [4]. The MoO_x film showed an O/Mo atomic ratio of 2.74, which demonstrated that the MoO_x thin film was a sub-stoichiometric molybdenum trioxide (MoO_x, x<3). Thus, MoO_x (x<3) was used as the as-prepared molybdenum oxide in this study. The XRD pattern showed only broad halo patterns, indicating that the deposited MoO_x was amorphous (Fig. 4.2d). The annealing has negligible effect on the phase of as-deposited MoO_x layer (Appendix, Fig, S4.5e).

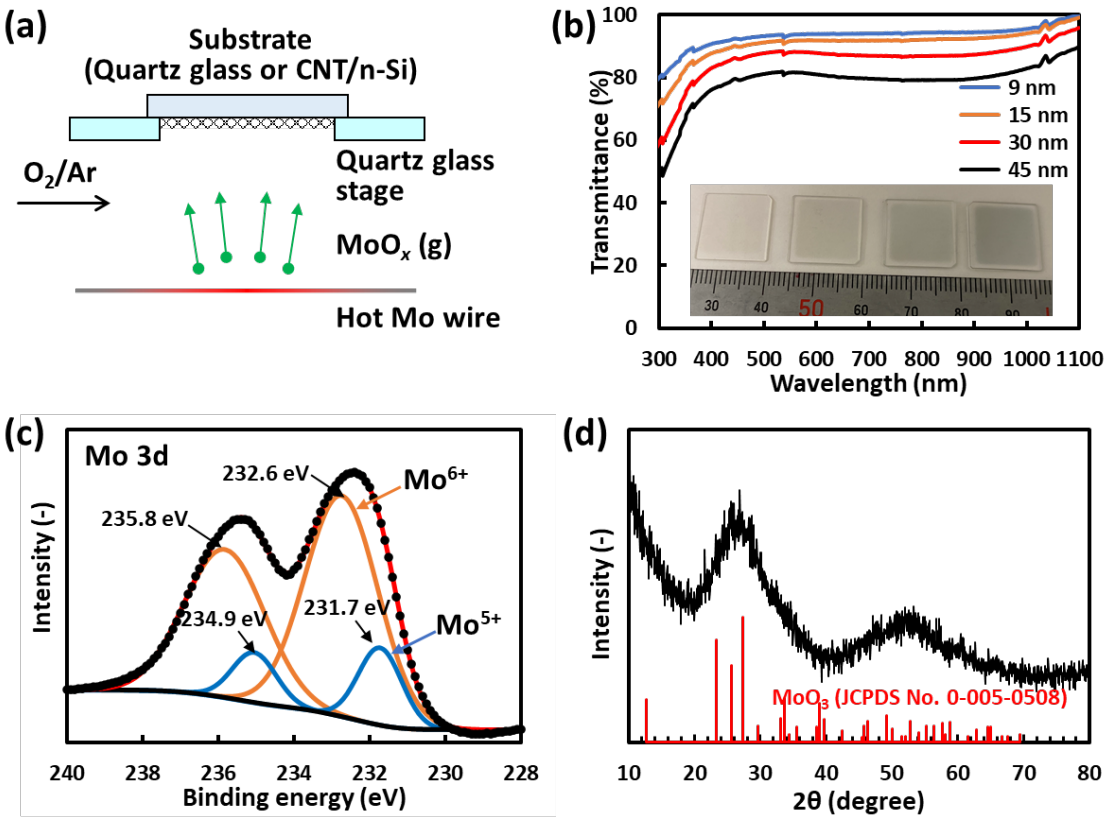

Fig. 4.2. (a) Schematic representing the reactive vapor deposition of the MoO_x layer using a Mo hot wire and low-pressure O_2/Ar gas. (b) Optical transmission spectra of MoO_x layer of various thicknesses deposited on quartz glass substrates. The inset shows a digital image of the substrates. (c) X-ray photoelectron spectroscopy (XPS) spectrum and (d) X-ray diffraction (XRD) pattern of an as-deposited MoO_x film (thickness of ~30 nm deposited on a SiO_2/Si substrate).

4.3.2 Structure of the CNT/n-Si and MoO_x–CNT/n-Si solar cells

Fig. 4.3a, b exhibited the top-view digital images and schematics of the CNT/n-Si and MoO_x–CNT/n-Si heterojunction solar cells. The pristine CNT film exhibited a loose structure with void space (Fig. 4.3c, d), and the CNT film retained its morphology at low magnification after the deposition of MoO_x at a rate of ~3 nm/min for 10 min (Fig. 4.3e, f). Some differences between the MoO_x–CNT structure and the CNT film were found upon analyzing the top-view high-magnification image; the void space was filled with MoO_x (Fig. S4.3a). The dense MoO_x–CNT composite film will help in enhancing the charge transfer between MoO_x and CNTs [5].

The dense MoO_x–CNT composite film will also be benefit in preventing the Ag grids and Si from coming into direct contact. The EDS elemental maps show the uniform distribution of O and Mo in the MoO_x–CNT film (Appendix, Fig. S4.3b, c). Fig. 4.3g, h shows the AFM images of the CNT films without and with MoO_x. The root-mean-square (RMS) roughness of the sample surfaces slightly decreased from 14.5 to 11.7 nm after MoO_x deposition, indicating that the MoO_x–CNT film was smoother than the pristine CNT film.

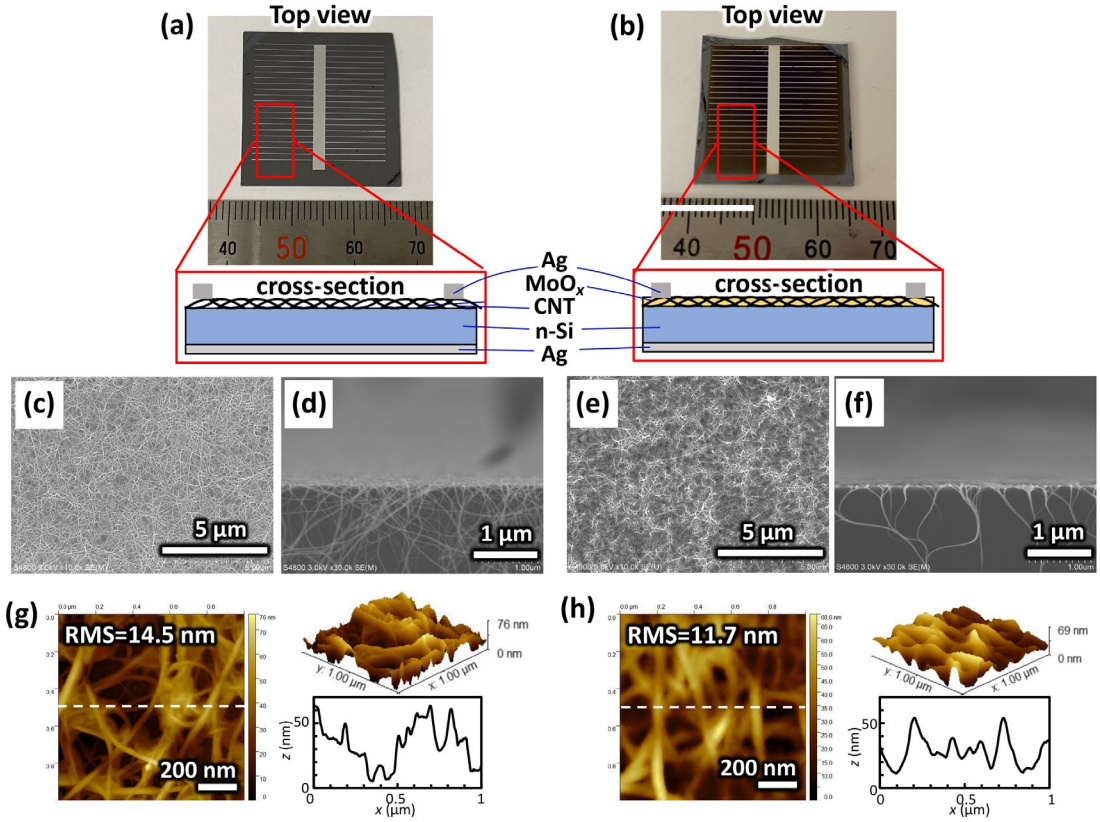

Fig. 4.3. (a,b) Top-view digital images with cross-sectional schematics of the carbon nanotube (CNT)/n-type Si (n-Si) (a) and MoO_x–CNT/n-Si (b) heterojunction solar cells. (c–f) Top view (c,e) and cross-sectional (d,f) scanning electron microscopy (SEM) images of the pristine CNT film (c,d) and the MoO_x–CNT film (e,f) on the SiO_2/Si substrate. The CNTs adhered to the cross-sections of the n-Si wafers when preparing the cross-sectional samples, as shown in (d,f). (g,h) Atomic force microscopy (AFM) images of the pristine CNT film (g) and the MoO_x–CNT film (h) on the SiO_2/Si substrate. Line profiles at the positions marked with white broken lines in the AFM images are also shown. All the samples had a CNT film possessing ~84% transmittance. The MoO_x layer was ~30 nm thick.

4.3.3 Effect of MoO_x thickness on the PV performance of the solar cells

The thickness dependence of the MoO_x layer on PV performance of MoO_x–CNT/n-Si solar cells was investigated by varying the deposition time of MoO_x (Fig. 4.4). The PV performance first improved when increasing the MoO_x thickness from 15 to 30 nm, which resulted in a significant increase in short-circuit current density (J_{sc}) value from 17.7 to 21.7 mA/cm^2, open circuit voltage (V_{oc}) value from 0.33 to 0.52 V, FF value from 0.22 to 0.46, and PCE from 1.3 to 5.2%. This is mainly due to the contact between Ag and n-Si being more suppressed by the thicker films, and because the p-type doping of the CNTs and/or the antireflection effect of the MoO_x–CNT layer was enhanced. Further increasing the MoO_x thickness from 30 to 60 nm resulted in a significant reduction in J_{sc} value from 21.7 to 16.5 mA/cm^2 and PCE from 5.2 to 3.1% (Fig. 4.4). In summary, thinner MoO_x layer resulted in low V_{oc} and high current leakage, while thicker MoO_x layer led to an increased series resistance and, consequently, decreased J_{sc} and FF. This could be ascribed to the decreased optical transmittance (Appendix, Fig. S4.5a) and increased sheet resistance (Appendix, Fig. S4.5d) for the MoO_x–CNT layer with thicker MoO_x.

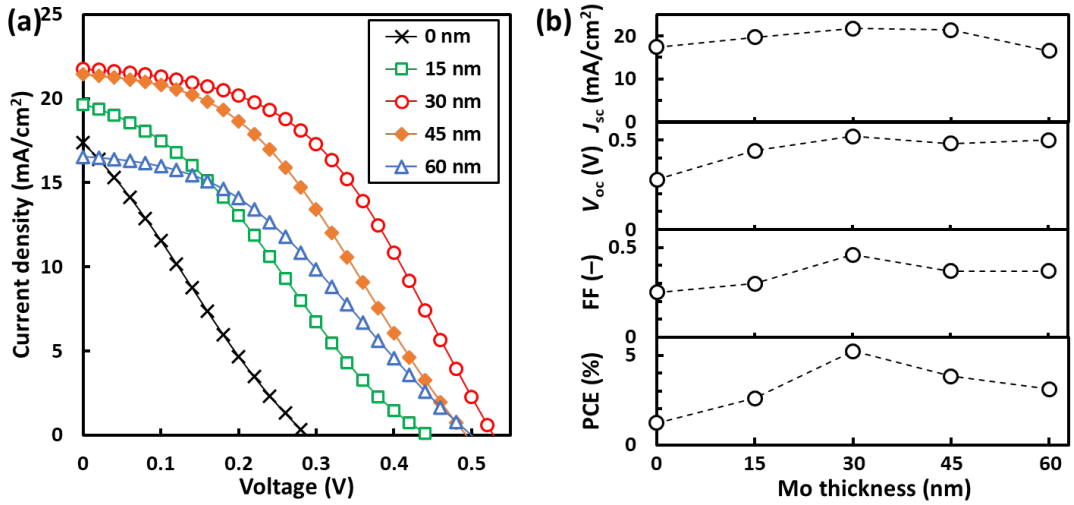

Fig. 4.4. (a) *J–V* curves of the MoO_x–CNT/n-Si solar cells with various MoO_x-layer thicknesses. (b) PV parameters as a function of the MoO_x layer thickness.

4.3.4 Analysis of the junction between MoO_x and n-Si or CNT and n-Si

Measurements were further carried out to examine the contribution of the CNTs layer and as-deposited MoO_x layer to the formation of heterojunction with underlying n-Si (Fig. 4.5). Three type structures of cells of the MoO_x–CNT/n-Si, MoO_x–CNT-MoO_x/n-Si and CNT–MoO_x/n-Si were fabricated by changing the deposition order of MoO_x and CNT (as shown in Fig. 4.5). The MoO_x–CNT/n-Si solar cell exhibited the best PV performance (PCE: 9.3%) owing to the high J_{sc}, FF, and V_{oc}. The CNT–MoO_x/n-Si solar cells showed the worst PV performance (0.3%), probably due to the high sheet resistance of as-deposited MoO_x layer. The MoO_x–CNT-MoO_x/n-Si solar cell presented a PCE of 2.4%. It is confirmed that the CNT layer plays a more important role than as-deposited MoO_x layer in forming the heterojunction with n-Si.

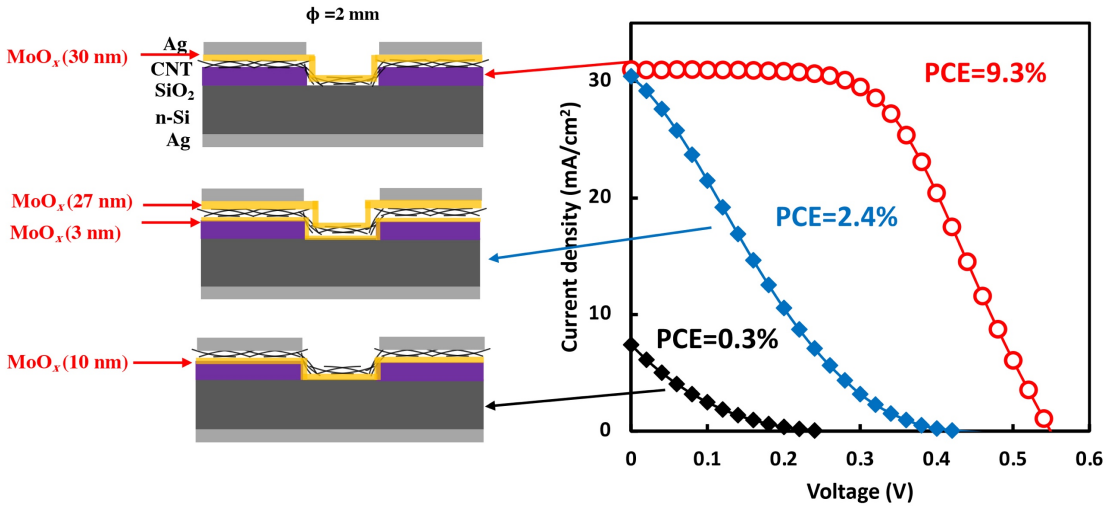

Fig. 4.5. The device structure and *J–V* curves of the solar cells with different heterojunctions of 30 nm MoO_x–CNT/n-Si, 27 nm MoO_x–CNT-3 nm MoO_x/n-Si, and CNT–10 nm MoO_x/n-Si heterojunction. All the cells were evaluated without treating by thermal annealing.

4.3.5 Effect of thermally annealing on the PV performance of the solar cells

It has been reported that the electrical conduction of the MoO_x–CNT film can be improved by thermally annealing, which enhances the charge transfer between MoO_x and the CNTs [5].

Therefore, the thermally annealing was applied to my MoO_x–CNT/n-Si solar cells. First, the MoO_x layer was deposited onto CNT/n-Si at different substrate temperatures. The slight increase from room temperature to 100 °C resulted in a significant decrease in PCE from 5.2% to 3.8% (Fig. 4.6d). This was ascribed to the V_{oc} value significantly decreasing from 0.52 to 0.40 V (Fig. 4.6b) and the FF value decreasing from 0.46 to 0.40 (Fig. 4.6c), which occurred despite the slight increase in the J_{sc} value (Fig. 4.6a). The O_2 gas used during MoO_x deposition could have possibly reached and oxidized the n-Si surface. To proof this hypothesis, the n-Si surface heated at 200 °C in 5 vol% O_2/Ar was characterized using XPS. As shown in Fig. S4.5f in Appendix, a Si-O peak was observed from the XPS spectrum of the n-Si wafer. Next, I examined the thermally annealing of the MoO_x–CNT/n-Si solar cell in Ar and 20 vol% O_2/N_2 gaseous environments. The cell showed considerable improvement in its PV performance, with its PCE increasing from 5.2% to 6.7% and 7.9% via annealing at 200 °C in Ar gas and 20 vol% O_2/N_2 gas, respectively (Fig. 4.6d). The PCE enhancement was attributed to the increase in both FF and J_{sc} (Fig. 4.6a, c), indicating that post-thermal annealing can effectively promote the charge transfer between MoO_x and CNTs for enhanced charge separation at the heterojunction and electric conduction through the MoO_x–CNT composite film. The PV performance was enhanced more significantly when post-annealing was conducted in O_2/Ar rather than Ar, which is possibly due to O atoms filling the oxygen vacancies contained in the as-deposited MoO_x film, as discussed above (Fig. 4.2). The MoO_x–CNT/n-Si surfaces were then analyzed by XPS and UPS (Appendix, Fig. S4.4) to present more scientific proofs to support above discussion. The O/Mo ratio and the work function remained small when annealed in Ar (2.63 and 4.85 eV) while increased when annealed in 20 vol% O_2/N_2 (2.86 and 5.33 eV). The MoO_x as-deposited by the hot-wire oxidation–sublimation deposition method contained the O vacancy; therefore, it is effective to add oxygen to the MoO_x layer via heat treatment with O_2 supply.

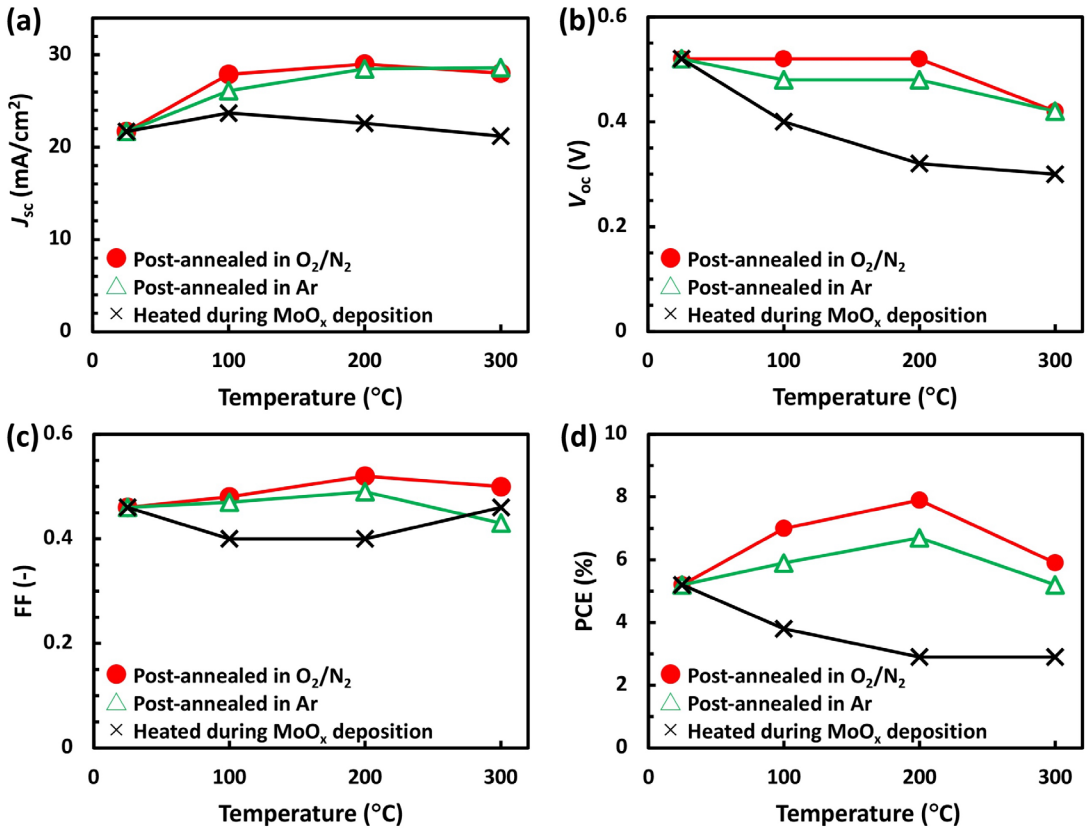

Fig. 4.6. Photovoltaic (PV) performance of the MoO_x–CNT/n-Si heterojunction solar cell heat treated under various conditions. Plots of (a) short-circuit current density (J_{sc}), (b) open circuit voltage (V_{oc}), (c) fill factor (FF), and (d) power conversion efficiency (PCE) under the different conditions. Three different thermal treatments were applied: (i,ii) MoO_x was deposited onto CNT/n-Si without substrate heating, and was then thermally annealed under 20 vol% O_2/N_2 (i) or Ar (ii) for 10 min; or (iii) MoO_x was deposited on CNT/n-Si with substrate heating. The MoO_x layer was deposited at a rate of ~3 nm/min for 10 min.

The post-annealing conditions of the MoO_x–CNT/n-Si solar cell was further optimized by changing the temperature and time more carefully. Increasing the temperature from room temperature (RT) to 200 °C increased the J_{sc} value from 22.2 to 29.5 mA/cm^2 (Fig. 4.7 a,b, Table. S4.1), which was possibly owing in part to the enhanced anti-reflection effect of the MoO_x–CNT film that resulted from the increased film density. Meanwhile, further increase in temperature, from 200 to 300 °C, resulted in V_{oc} value decreasing from 0.50 to 0.41 V (Fig. 4.7a, b and Table S4.1). The optimum temperature was approximately 200 °C, which resulted

in a PCE of 7.8 ± 0.1%. The annealing time was then optimized at 200 °C (Fig. 4.7c, d and Appendix, Table S4.2). The FF gradually increased with annealing time to reach a maximum of 0.59 at 90 min, yielding the highest PCE of 9.1%. The effect of post-annealing on the optical transmittance, optical surface reflectance, and sheet resistance of the MoO_x–CNT layer was studied on quartz glass substrates. The 0.0314 cm^2-sized small solar cell annealed under the optimum condition (90 min, 200 °C) showed a slightly higher PCE of 10.6% (Appendix, Fig. S4.6) owing mainly to the shadow-less structure. The optical transmittance at 550 nm increased from 72.7% to 78.0% (Appendix, Fig. S4.5b) and the sheet resistance decreased from 216 to 144 Ω/sq (Appendix, Fig. S4.5d), which contributed to the enhancement of the PV performance of the MoO_x–CNT/n-Si solar cell.

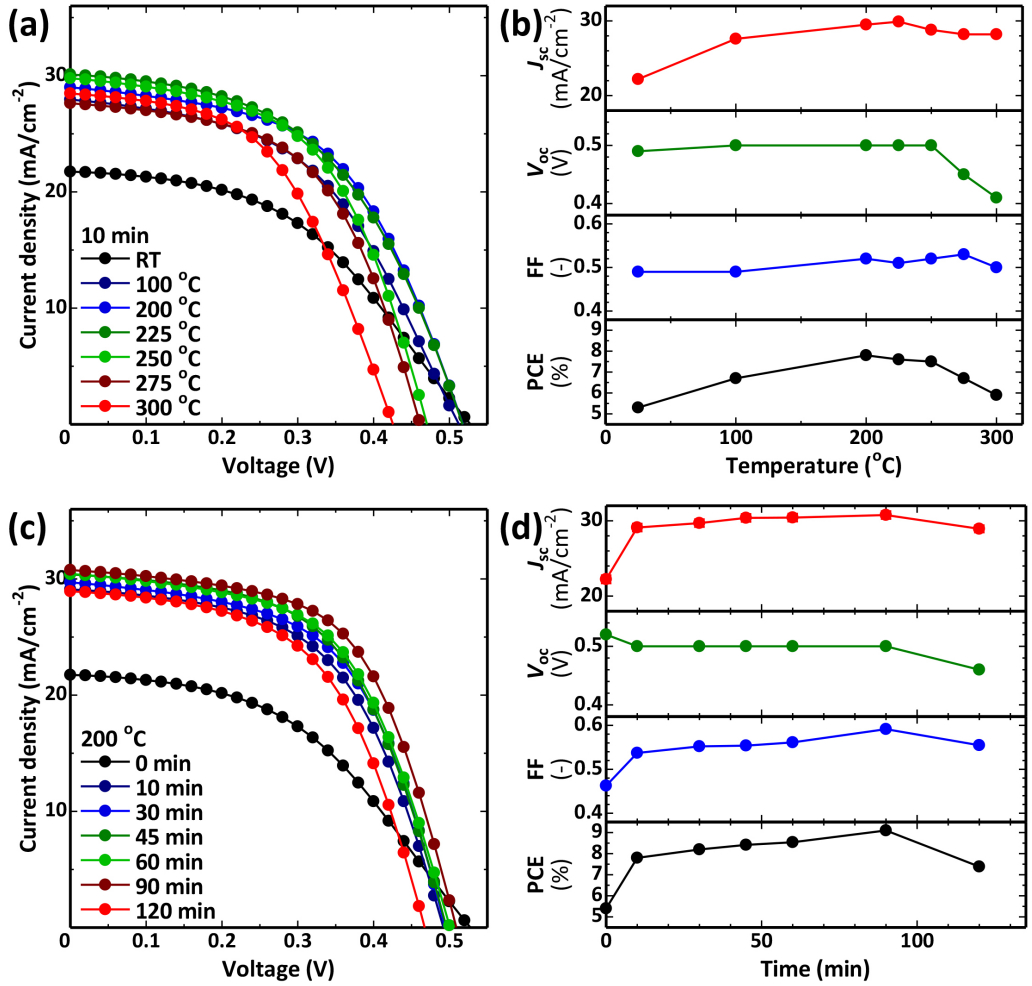

Fig. 4.7. PV performance of the MoO_x–CNT/n-Si heterojunction solar cells heat treated in 20 vol% O_2/N_2. (a,c) *J–V* curves and (b,d) PV parameters of the MoO_x–CNT/n-Si solar cells annealed at various temperatures for 10 min (a,b) and at 200 °C for various time periods (c,d).

4.3.6 Mechanism of thermally annealing for MoO_x–CNT/n-Si

The mechanism of thermally annealing for MoO_x–CNT/n-Si for enhancement of the PV performance of MoO_x–CNT/n-Si solar cells was then studied by XPS and UPS analyses. XPS Mo 3d profiles had Mo^{6+} and Mo^{5+} components with decreasing Mo^{5+} fraction from 17%, 12%, to 9% with increasing annealing temperature from pristine (Fig. 4.8a), 100 °C, to 200 °C, showing the addition of O to the O^{2-} vacancy in the MoO_x. Further increase in annealing temperature to 300 °C resulted in the increasing Mo^{5+} fraction to 20%, surprisingly. The O/Mo atomic ratio and the work function showed consistent results; O/Mo ratio first increased and

then decreased while the work function first increased and then decreased from the pristine MoO_x–CNT, that annealed at 200 °C, to that annealed at 300 °C (Fig. S4.8c). All these results show that MoO_x is oxidized at 100–200 °C while reduced at 300 °C. B. Han et al. reported the same change for their MoO_x/Si sample [6]. I then examined the Gibbs energy of reaction ($\Delta_r G$) of the reaction of $MoO_{2.75}(cr) + 0.125O_2(g) \rightarrow MoO_3(cr)$. Fig. 4.8d shows that this reaction has $\Delta_r G° < 0$ for the temperature range of 0–300 °C that increases and approaches to 0 with increasing temperature. In addition, for the experimental condition with p_{O2} = 20 kPa, $\Delta_r G$ increases and approaches 0 further. Although $\Delta_r G$ still remains negative (–25.2 kJ/mol) at 327 °C, considering the deviation of the standard Gibbs energy of formation $\Delta_f G°$ of the actual disordered MoO_x thin layers from those of bulk crystals of $MoO_{2.75}$ and MoO_3, MoO_x may release O_2 at elevated temperatures. In summary, MoO_x had the largest x and the highest work function when annealed at 200 °C.

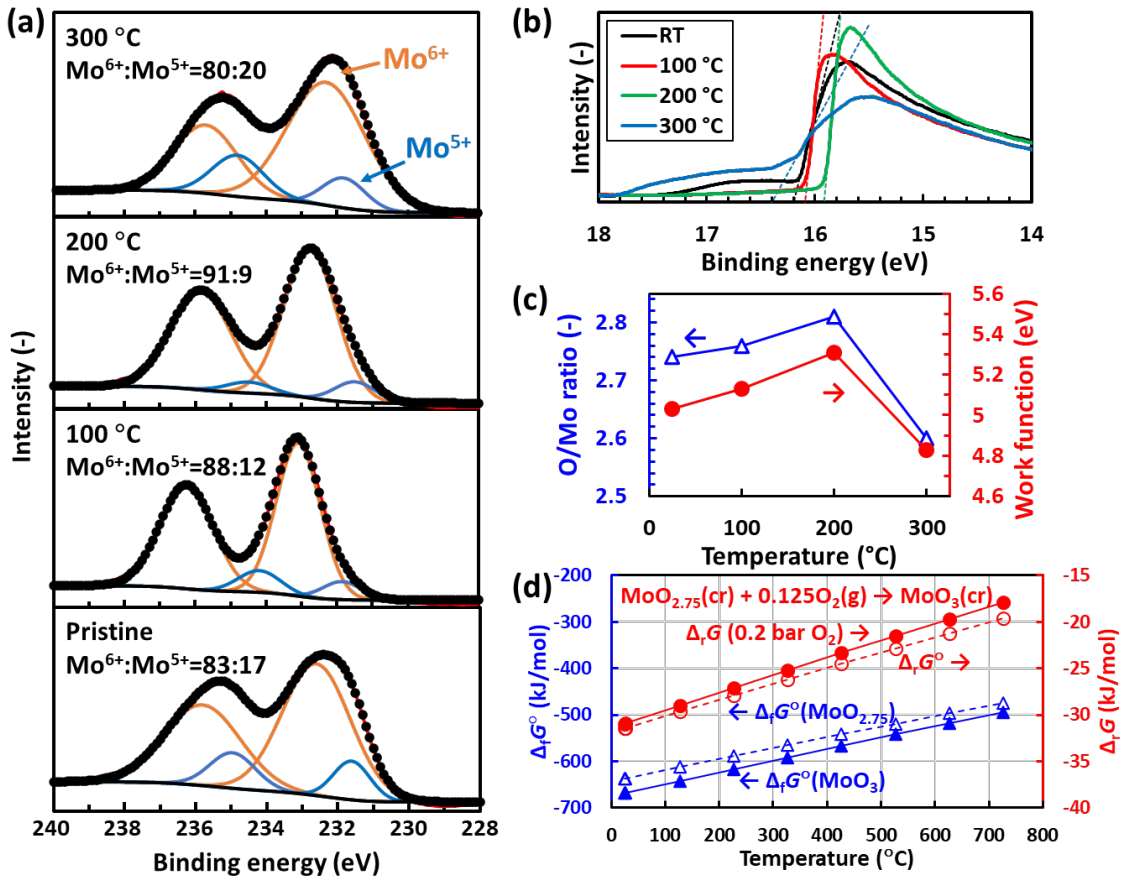

Fig. 4.8. XPS and UPS analyses of the as-deposited MoO_x–CNT/n-Si and the MoO_x–CNT/n-Si heat treated in 20 vol% O_2/N_2 for 10 min. (a) XPS Mo 3d profiles. (b) UPS profiles. (c) O/Mo atomic ratio estimated by XPS, and work function estimated by UPS. (d) Standard Gibbs energy of formation ($\Delta_f G°$) of $MoO_{2.75}$ and MoO_3 with (standard) Gibbs energy of reaction ($\Delta_r G°$, $\Delta_r G$) of $MoO_{2.75}(cr) + 0.125O_2(g) \rightarrow MoO_3(cr)$ calculated from $\Delta_f G°$ and $\Delta_r G = \Delta_r G° – RT\ln\{(p_{O2}/p°)^{0.125}\}$. $\Delta_f G°$ values are from the NIST-JANAF Thermochemical Tables (https://janaf.nist.gov/).

The PV performance enhancement with the time at 200 °C in 20 vol% O_2/N_2 is mainly attributed to the oxidation of MoO_x; the Mo^{5+} fraction decreased from 17% to 4%, the O/Mo atomic ratio increased from 2.74 to 2.86, and work function increased from 5.03 to 5.32 eV with increasing annealing time to 90 min (Fig. 4.9). MoO_x got somewhat reduced after 120 min although the mechanism remained unclear.

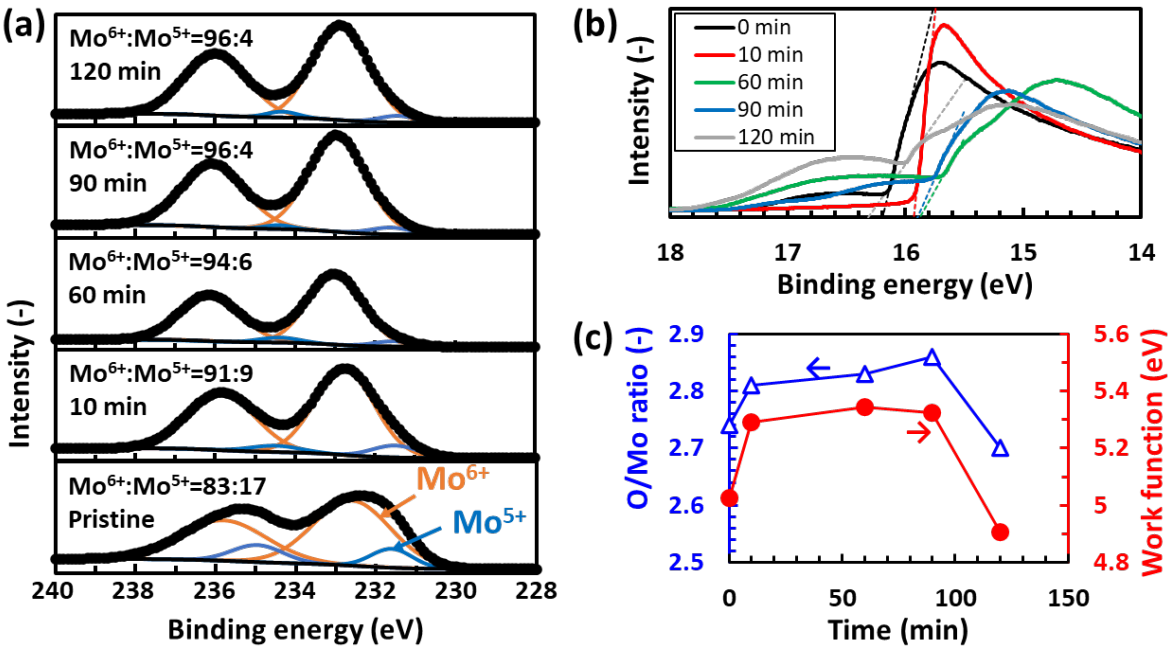

Fig. 4.9. XPS and UPS analyses of the as-deposited MoO_x–CNT/n-Si and the MoO_x–CNT/n-Si heat treated in 20 vol% O_2/N_2 at 200 °C. (a) XPS Mo 3d profiles. (b) UPS profiles. (c) O/Mo atomic ratio estimated by XPS, and work function estimated by UPS.

4.3.7 Role of MoO_x in the enhancement of the PV performance of the solar cell

The possible mechanism of PV performance enhancement was evaluated by comparing the CNT/n-Si solar cells with and without MoO_x. As represented in Fig. 4.5a and Table 4.1, the CNT/n-Si solar cell without MoO_x exhibited poor PV performance (J_{sc}: 17.7 mA/cm^2, V_{oc}: 0.33 V, FF: 0.22, PCE: 1.3 %). This is mainly due to the severe current leakage caused by the direct contact between the top Ag anode and the n-Si substrate and high internal series resistance, as can be seen in the low shunt resistance of R_{sh}=21 Ω and the high series resistance of R_s= 29.9 Ω/cm^2. Compared to the CNT/n-Si solar cell without MoO_x, the MoO_x–CNT/n-Si solar cell had a significantly improved PCE of 8.8% with a high J_{sc} value of 30.6 mA/cm^2, a V_{oc} value of 0.50 V, and an FF value of 0.58. Its R_{sh} value also increased to 1.1×10^3 Ω owing to MoO_x that filled the pores in the CNT films and prevented the Ag grid and n-Si from coming into direct contact. Fig. S4.7a confirms that the current leakage is significant in the Ag/CNT/n-Si structure while suppressed in the Ag/MoO_x/n-Si and Ag/MoO_x–CNT/n-Si structures. In addition, the R_s value

decreased to 4.3 Ω/cm^2, showing that MoO_x served as a dopant for the CNT film and allowed for efficient charge separation at the CNT/n-Si heterojunction. MoO_x also enabled efficient charge transport through the CNT without disturbing the electrical conduction between the CNT film and Ag grid. Moreover, the surface reflectance of the cell at 550 nm decreased from 29.5% (CNT/n-Si) to 7.6% (MoO_x–CNT/n-Si) (Fig. 4.10b), suggesting that MoO_x also works as an effective AR layer that increased the J_{sc} value from 17.7 to 30.6 mA/cm^2. The device fabricated using the MoO_x film alone exhibited a PCE of approximately 0.7% due to the high sheet resistance of the MoO_x thin film (Appendix, Fig. S4.9).

As discussed in the previous works [7–8], the CNT/n-Si heterojunction is complex and is not yet fully understood. The *J–V* characterization was performed for the solar cells under different light intensities and the ideality factor *n* was estimated using Equation (1) [9].

$$V_{oc} = \frac{nk_BT}{q}\ln\left(\frac{J_{sc}}{J_0}\right), \quad (1)$$

where k_B is the Boltzmann constant, T is the temperature, q is the elementary charge, and J_0 is the saturation current density. From the V_{oc} vs ln J_{sc} plot (Fig. 4.10c) using the V_{oc} and J_{sc} values obtained from the *J-V* curves at different light intensities (Appendix, Fig. S4.7b, c), the *n* value of 2.1 and 1.9 was gained for the CNT/n-Si and MoO_x–CNT/n-Si, respectively. The ideal p–n junction has a diode ideality factor of $n<2$, and both cells showed $n\approx2$. The diode ideality factor was better for the cell with MoO_x but the difference was not obvious. Then the dark log dark *J–V* curves of the CNT/n-Si solar cells with and without MoO_x were analyzed to understand the carrier transport mechanism of the solar cells (Appendix, Fig. S4.7d) using Equations (2) and (3) [10,11].

$$J = J_0[\exp(\frac{qV}{nk_BT}) - 1], \quad (2)$$

$$\varphi_B = \frac{k_B T}{q} \ln\left(\frac{A^* T^2}{J_0}\right), \quad (3)$$

where φ_B is the Schottky barrier height and A^* is the Richardson constant. J_0 is obtained by fitting the dark *J-V* curve (Appendix, Fig. S4.7d) using Equation (2), and then φ_B values were calculated to be 0.64 eV (CNT/n-Si) and 0.73 eV (MoO_x–CNT/n-Si) using J_0 and Equation (3). The possible band alignment is schematically shown in Fig. 4.10d. The work function was evaluated as 5.32 eV (MoO_x–CNT) and 4.48 eV (CNT) by the UPS measurement (Appendix, Fig. S4.7e), respectively. Therefore, a MoO_x–CNT film with a high work function would yield a large built-in potential (V_{bi}), that is proportional to the work function difference at the heterojunction with n-Si. The MoO_x–CNT/n-Si heterojunction with a smaller *n*, larger φ_B, and larger V_{bi} enables more efficient separation of the electron–hole pairs with suppressed diffusion recombination [12–13] than the pristine CNT/n-Si heterojunction, resulting in the FF value increasing from 0.22 to 0.58 and V_{oc} value increasing from 0.33 to 0.50 V (Table4.1).

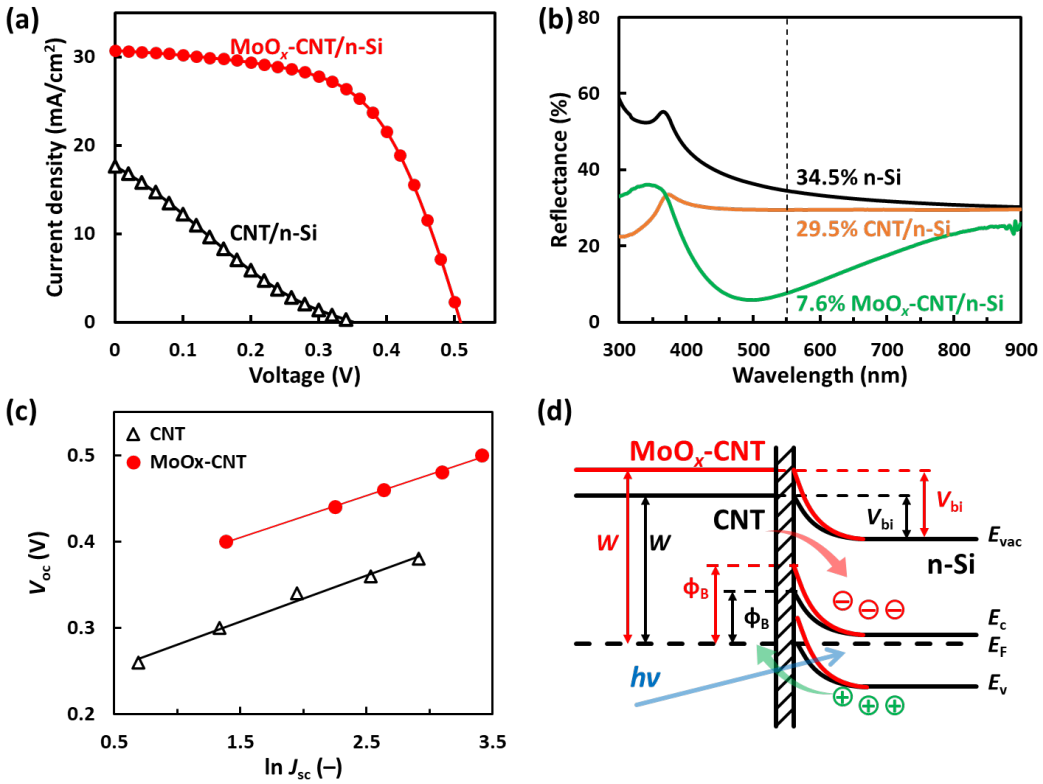

Fig. 4.10. Comparison of the CNT/n-Si and the MoO_x–CNT/n-Si solar cells. (a) *J*–*V* curves. (b) Optical reflection spectra of a bare n-Si wafer, CNT/n-Si, and MoO_x–CNT/n-Si. (c) *V*-ln *J* plots obtained from *J*–*V* curves under different light intensities in Fig. S11b, c. (d) Predicted band alignment at the CNT/n-Si and MoO_x–CNT/n-Si interfaces.

Table 4.1. PV parameters of the CNT/n-Si and MoO_x–CNT/n-Si solar cells under AM1.5G one-sun illumination. Standard deviations are also shown for the four cells fabricated and evaluated.

	J_{SC} (mA/cm^2)	V_{OC} (V)	FF	R_s (Ω/cm^2)	R_{sh} (Ω/cm^2)	PCE (%)
CNT /n-Si	17.7 ± 0.4	0.33 ± 0.03	0.22 ± 0.03	29.9 ± 6.2	21	1.3 ± 0.1
MoO_x-CNT /n-Si	30.6 ± 0.4	0.50 ± 0.02	0.58 ± 0.02	4.3 ± 0.1	1.1 x10^3	8.8 ± 0.3

4.3.8 Further enhancement of the PV performance of the MoO_x–CNT/n-Si solar cell

The PV performance of the MoO_x–CNT/n-Si solar cells was further improved by adding a PMMA AR layer. The optical reflection spectra changed with PMMA concentration, and the

reflection was significantly suppressed at wavelengths >500 nm for a 2 wt% PMMA solution (Fig. 4.11a). Four cells were fabricated and evaluated for the annealed MoO_x–CNT/n-Si solar cell without PMMA (Table S4.3, Fig. S4.10) and with PMMA (Table S4.4, Fig. S4.11). The color of the solar cell changed from violet to dark-blue violet after spin-coating the 2 wt% PMMA solution (Fig. 4.10b), indicating the enhancement of light absorption. The PCE increased from 8.8±0.2% to 9.7±0.3% with the AR layer that was made using the 2 wt% PMMA solution, which was mainly owing to the J_{sc} value increasing from 30.6±0.4 to 33.2±0.4 mA/cm^2. The best device exhibited a PCE of 10.0% (Fig. 4.10b, Table S4.4). Fig. 4.10c presents the corresponding EQE spectra of the device with and without PMMA, showing a significantly improved EQE for the wavelength range of 500–900 nm. I used a simple mask-sputtering technique that yielded a large shadow (65.4 mm^2 and 16.0%) owing to the wide busbar and fingers (Fig. 4.1). By simply decreasing the shadow, a maximum PCE of ~12% is expected.

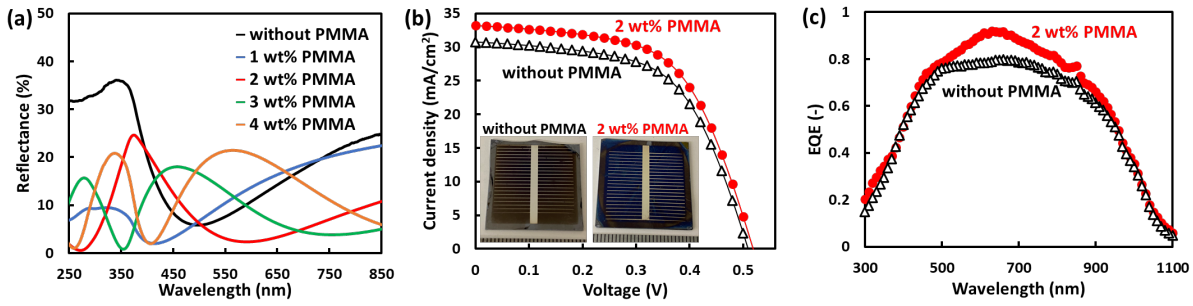

Fig. 4.11. MoO_x–CNT/n-Si solar cells with and without the polymethyl methacrylate (PMMA) anti-reflective (AR) layer. (a) Optical reflectance spectra of the MoO_x–CNT/n-Si with and without the AR layer spin-coated using various PMMA solutions. (b) *J–V* curves with inset digital images of the solar cells. (c) External quantum efficiency (EQE) spectra.

4.4 Conclusions

In summary, a MoO_x multifunctional layer was proposed for the size and performance enhancement of CNT/n-Si heterojunction solar cells. A 4 cm^2-sized PMMA/MoO_x–CNT/n-Si

solar cell with a PCE of 10.0% was realized via a simple process: a dispersion–filtration–transfer process for the CNT layer, hot-wire oxidation–sublimation deposition for the MoO_x layer, mask-deposition for the Ag grid electrodes, and spin coating for the PMMA AR layer. The MoO_x layer played an essential role as a blocking layer preventing direct contact and current leakage between Ag and n-Si. This layer also served as a p-type dopant for the CNTs to enhance the electrical conduction and separation of electron–hole pairs at the heterojunction, and an enhancer for the AR effect of the MoO_x–CNT layer. The as-deposited MoO_x was sub-stoichiometric (x<3) and amorphous, and MoO_x with an optimum thickness of ~30 nm enhanced the PCE from 1.3% to 5.2%. Then, heat treatments of the MoO_x–CNT/n-Si were carefully investigated, and post-thermal annealing in 20 vol% O_2/N_2 at 200 °C for 90 min effectively enhanced the PCE to 9.1%. This was due to the increased O/Mo ratio and the increased work function of the MoO_x–CNT layer. The dark J–V characteristics were analyzed, and band energy alignment was discussed to understand the carrier transport mechanism of the solar cells with the MoO_x layer. The MoO_x layer reduced the diode ideality factor and increased the Schottky barrier height, leading to suppressed carrier recombination and improved V_{oc} and FF values. Finally, the PMMA AR layer was adopted for the MoO_x–CNT/n-Si solar cell, and the highest PCE of 10.0% was achieved for a 409-mm^2 active area. The top Ag grid electrode obtained by simple mask-sputtering yielded a large shadow (65.4 mm^2 and 16.0% of the active area) in the present device, which, when decreased, is expected to give a maximum PCE of ~12%. The presented method would also work with various other oxides, such as WO_x and VO_x, that have similar characteristics to those of MoO_x. I demonstration of a multifunctional oxide layer enabling size and performance enhancements via a simple and scalable deposition method will advance the practical applications of CNT/Si heterojunction solar cells.

Appendix

Table S4.1. Photovoltaic (PV) parameters of the MoO_x–carbon nanotube (CNT)/n-type Si (n-Si) solar cells post-annealed for 10 min in 20 vol% O_2/N_2 at various temperatures. Four solar cells were fabricated for each temperature.

Temperature (°C)	J_{sc} (mA/cm^2)	V_{oc} (V)	FF	Efficiency (%)
RT	22.2 ± 0.7	0.49 ± 0.04	0.49 ± 0.03	5.3 ± 0.2
100	27.6 ± 0.8	0.50 ± 0.02	0.49 ± 0.01	6.7 ± 0.2
200	29.5± 0.5	0.50 ± 0.02	0.52 ± 0.02	7.8 ± 0.1
225	29.9± 0.2	0.50 ± 0.02	0.51 ± 0.03	7.6 ± 0.2
250	28.8± 0.8	0.50 ± 0.02	0.52 ± 0.01	7.5 ± 0.1
275	28.2± 0.8	0.45 ± 0.01	0.53 ± 0.01	6.7 ± 0.2
300	28.2± 0.2	0.41 ± 0.01	0.50 ± 0.01	5.9 ± 0.2

Table S4.2. PV parameters of the MoO_x–CNT/n-Si solar cells post-annealed in 20 vol% O_2/N_2 at 200 °C for different time periods.

Time (min)	J_{sc} (mA/cm^2)	V_{oc} (V)	FF	Efficiency (%)
RT	21.7	0.52	0.46	5.2
10	29.1	0.50	0.54	7.8
30	29.7	0.50	0.55	8.2
45	30.4	0.50	0.55	8.4
60	30.4	0.50	0.56	8.5
90	30.8	0.50	0.59	9.1
120	28.9	0.46	0.56	7.4

Table S4.3. PV parameters of the MoO_x–CNT/n-Si solar cells. Four cells were fabricated using the CNT films exhibiting ~84% transmittance by depositing the MoO_x layer at a rate of ~3 nm/min for 10 min.

Cells number	J_{sc} (mA/cm^2)	V_{oc} (V)	FF	PCE (%)
# 1	30.8	0.50	0.59	9.1
# 2	30.8	0.52	0.56	8.9
# 3	29.9	0.50	0.58	8.7
# 4	30.8	0.50	0.56	8.6
AVE	30.6 ± 0.4	0.50 ± 0.01	0.57 ± 0.02	8.8 ± 0.2

Table S4.4. PV parameters of the PMMA/MoO_x–CNT/n-Si solar cells. Four cells were fabricated using the CNT films exhibiting ~84% transmittance by depositing the MoO_x layer at a rate of ~3 nm/min for 10 min and pin-coating a 2 wt% toluene solution of PMMA.

cells number	J_{sc} (mA/cm^2)	V_{oc} (V)	FF	Efficiency (%)
# 1	33.3	0.50	0.57	9.4
# 2	32.7	0.52	0.57	9.7
# 3	33.6	0.50	0.58	9.7
# 4	33.2	0.50	0.58	10.0
AVE	33.2 ± 0.4	0.51 ± 0.01	0.57 ± 0.01	9.7 ± 0.3

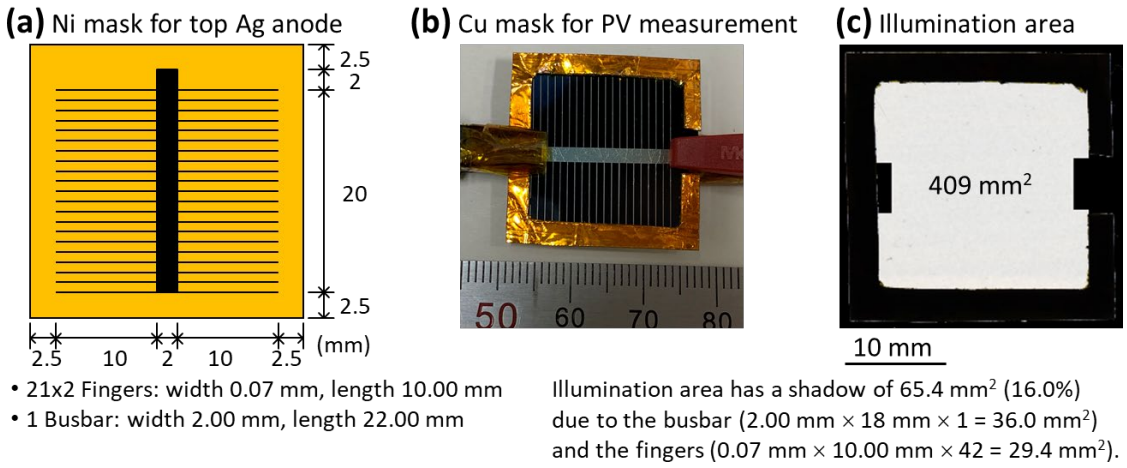

Fig. 4.1. Design of the masks used in fabricating and evaluating the solar cells. (a) The lithography-based Ni foil mask for the top Ag anode (thickness of 50 µm; fingers of 0.07 mm in width, 21×2 lines at 1.00 mm pitch, two 20.00×10.00 mm^2 region separated by a 22.00×2.00 mm^2 busbar). (b) The Cu foil mask used for limiting the illumination area during PV measurement. (c) Optically scanned image of the Cu mask. The illumination area was determined using Image J software.

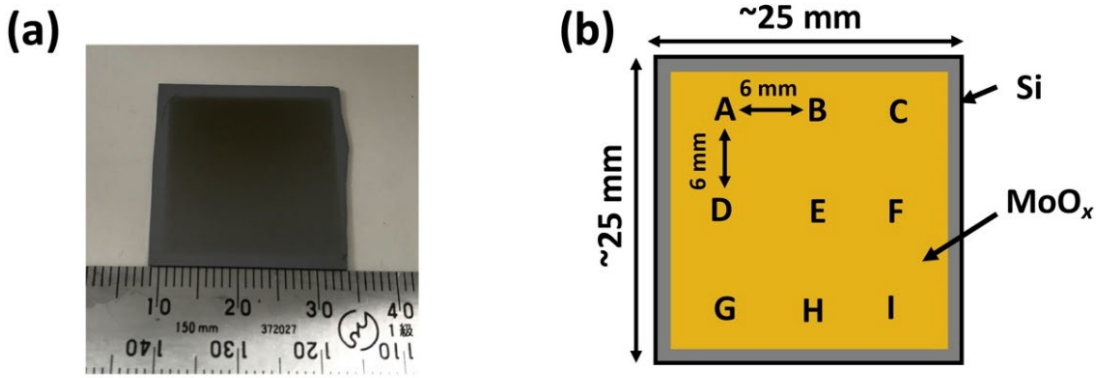

(c) (nm)

Position	A	B	C	D	E	F	G	H	I	Average
# 1	32	29	27	25	36	25	36	26	28	30 ± 4
# 2	30	32	33	28	34	26	25	25	29	29 ± 3
# 3	27	25	26	34	30	35	28	31	26	29 ± 4

Fig. S4.2. (a) Digital image of MoO_x thin film deposited on a SiO_2/Si substrate at a rate of ~3 nm/min for 10 min. (b) Schematic explaining the evaluation of the thickness distribution. (c) Thickness values in nm evaluated by a stylus profiler (three times each, giving 9 different points).

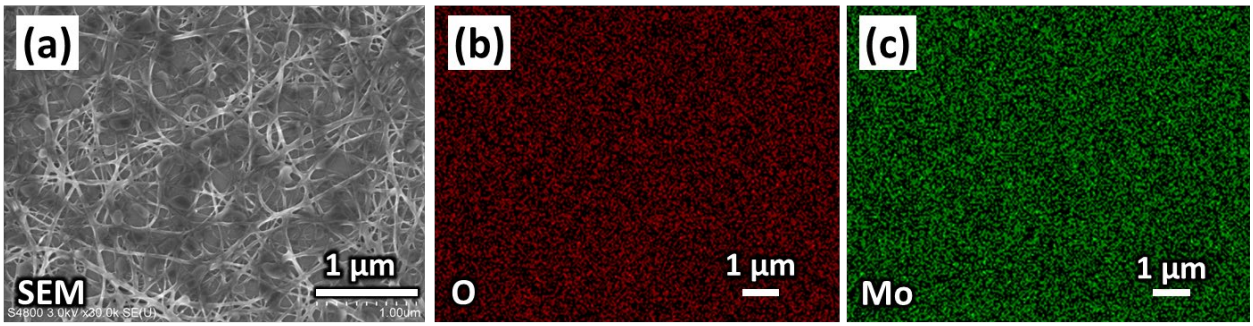

Fig. S4.3. (a) Top-view SEM image of the MoO_x–CNT film on a SiO_2/Si substrate. (b,c) EDS elemental maps of O (b) and Mo (c).

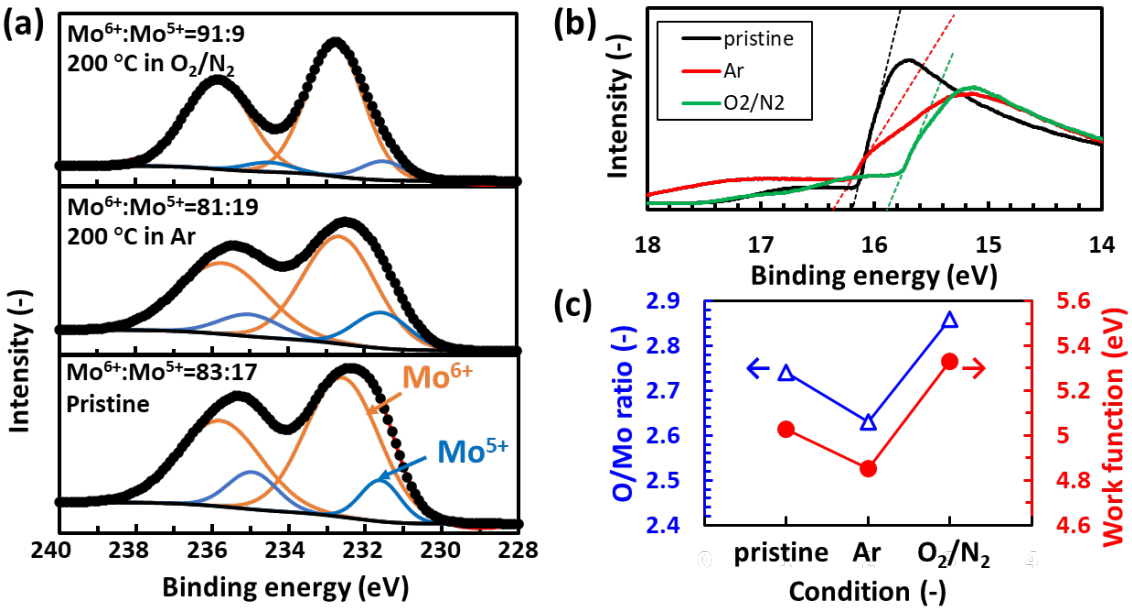

Fig. S4.4. XPS and ultraviolet photoelectron spectronmeter (UPS) analyses of the as-deposited MoO_x–CNT/n-Si and the MoO_x–CNT/n-Si heat treated for 10 min at 200 °C in Ar and 20 vol% O_2/N_2. (a) XPS Mo 3d profiles. (b) UPS profiles. (c) O/Mo atomic ratio estimated by XPS, and work function estimated by UPS.

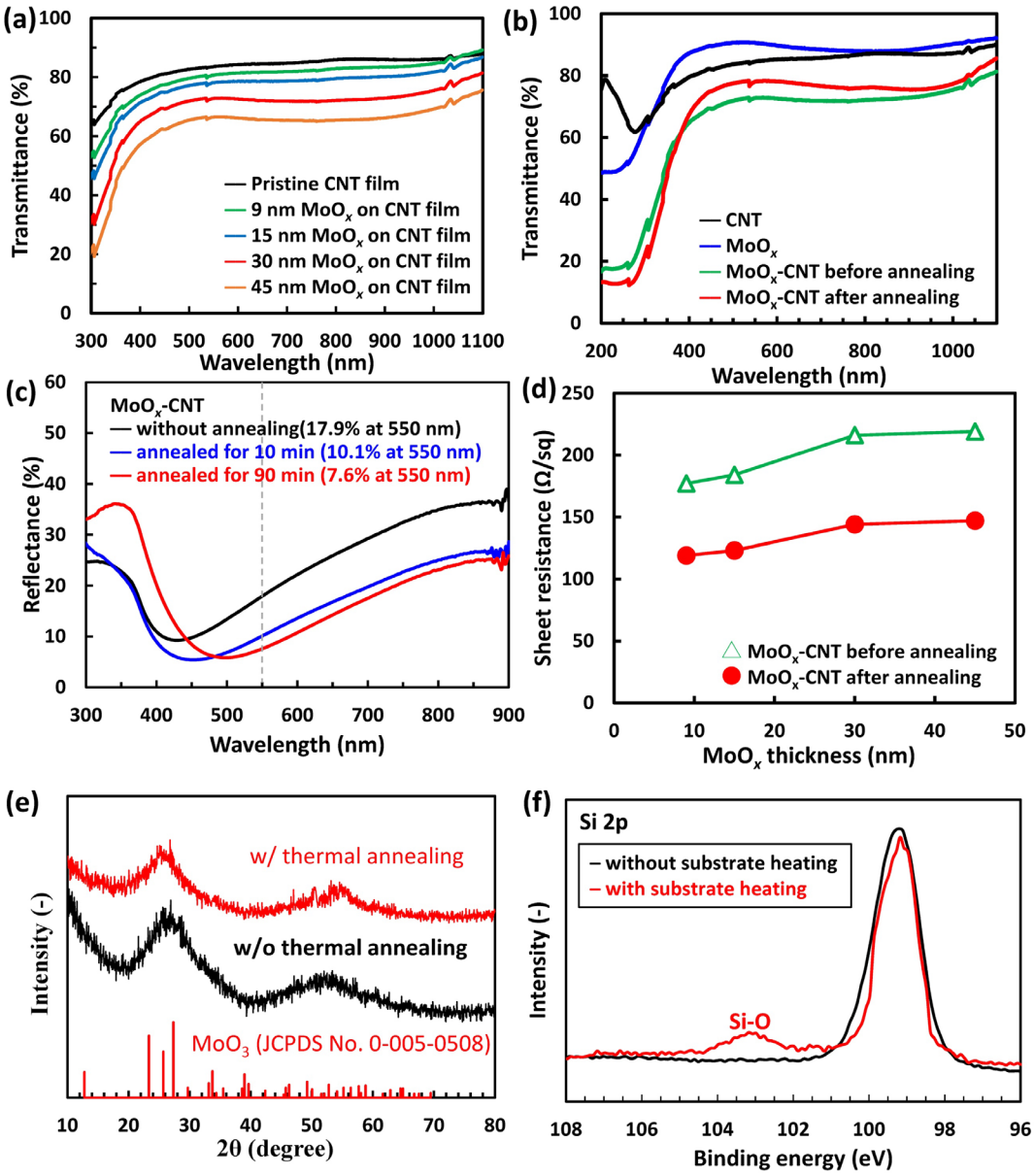

Fig. S4.5. (a) Optical transmission spectra of the CNT film with MoO_x of various thicknesses. (b) Optical transmission spectra of the CNT film, the MoO_x film, the MoO_x–CNT layer before annealing, and the MoO_x–CNT layer after annealing. (c) Optical surface reflection spectra of 30 nm MoO_x–CNT/n-Si without and with thermally annealing in 20 vol% O_2/N_2 at 200 °C for 10 min and 90 min. (d) Sheet resistance of the MoO_x–CNT layer before and after annealing. (e) XRD pattern of an as-deposited MoO_x film (thickness of ~30 nm deposited on a SiO_2/Si substrate) with and without thermally annealing at 200 °C in 20 vol% O_2/N_2 for 90 min. (f) XPS Si 2p spectra of the n-Si surfaces exposed to a 5 vol% O_2/Ar gas mixture at 1 Pa and 10 sccm without and with heating of the n-Si substrate to 200 °C in the hot-wire oxidation–sublimation deposition apparatus. To avoid the deposition of MoO_x, a Cu wire was used instead of the Mo wire. The native

oxide on the n-Si substrates were removed using a 4.7wt% HF aqueous solution prior to the exposure to O_2. All samples were prepared on quartz glass substrates in (a–c). Annealing was performed in 20 vol% O_2/N_2 at 200 °C for 90 min in (b,c). The CNT films with ~84% transmittance was used.

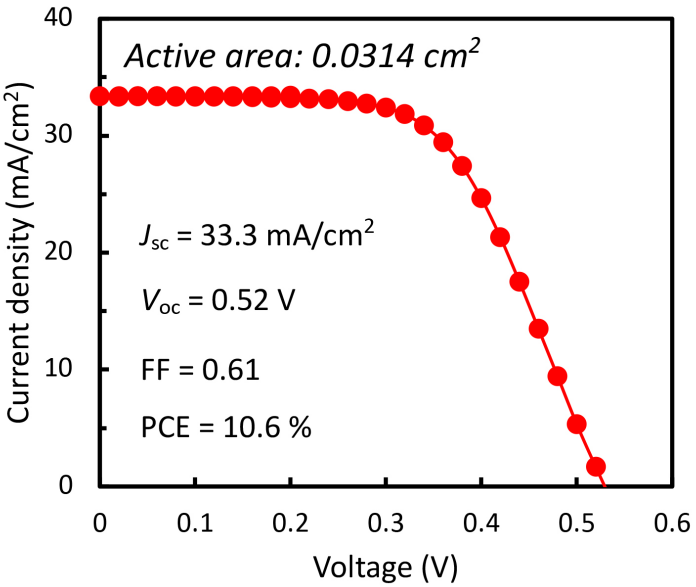

Fig. S4.6. *J-V* curve of the small MoO_x–CNT/n-Si solar cell. The thickness of the MoO_x layer was ~30 nm. The MoO_x–CNT/n-Si heterojunction was annealed under the optimum condition (20 vol% O_2/N_2 at 200 °C for 90 min).

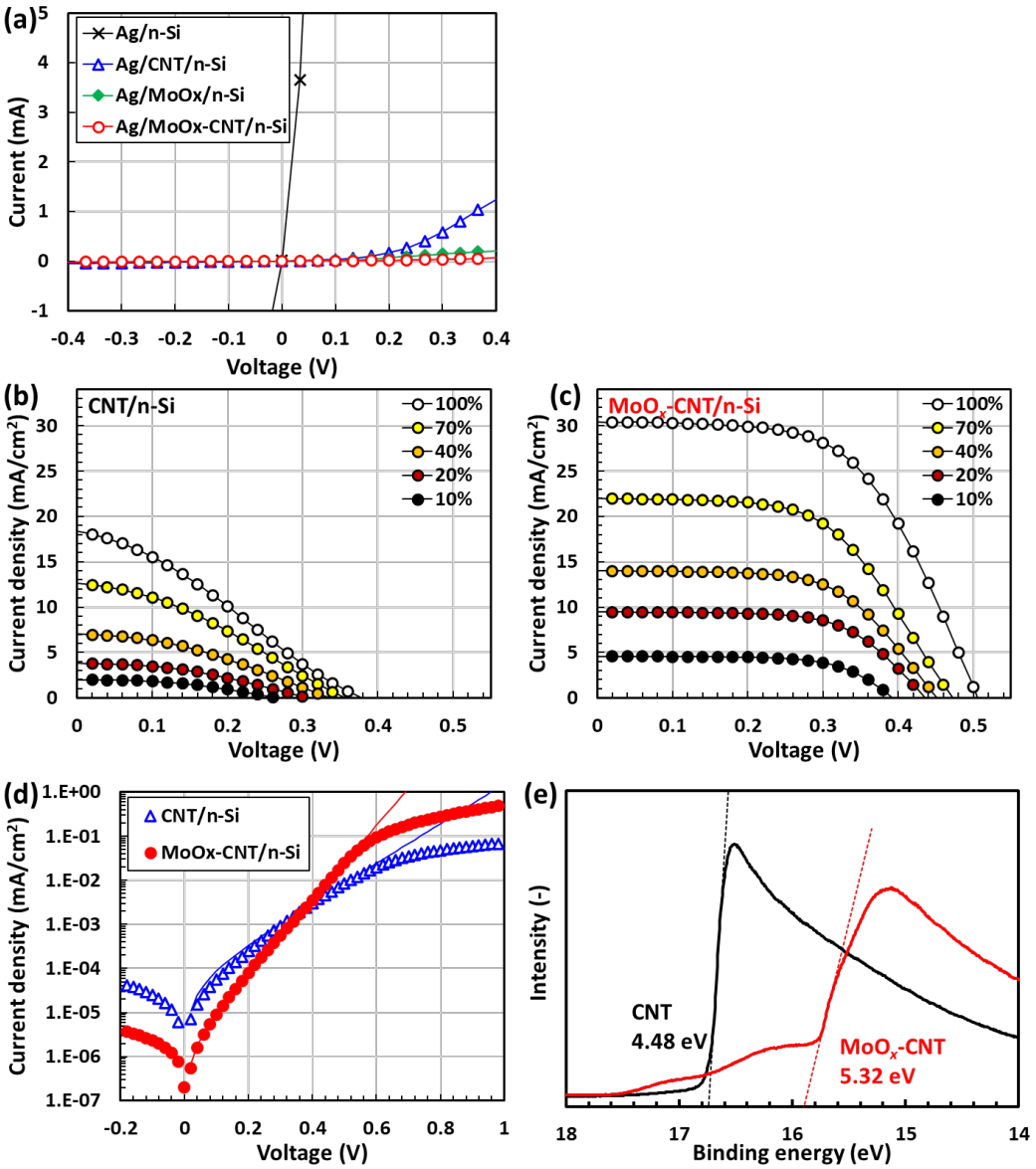

Fig. S4.7. (a) Leakage current evaluation for the various interfaces. Contacts were taken for the top Ag electrode and the rear of the n-Si substrate using an Ag paste. (b,c) *J-V* curves of the CNT/n-Si and MoO_x–CNT/n-Si solar cells with different light intensities. (d) The dark *J-V* curves of the CNT/n-Si and MoO_x–CNT/n-Si solar cells. (e) UPS analysis of CNT and MoO_x–CNT on n-Si. MoO_x-CNT of the optimum condition (30 nm MoO_x heat treated in 20 vol% O_2/N_2 at 200 °C for 90 min) was used.

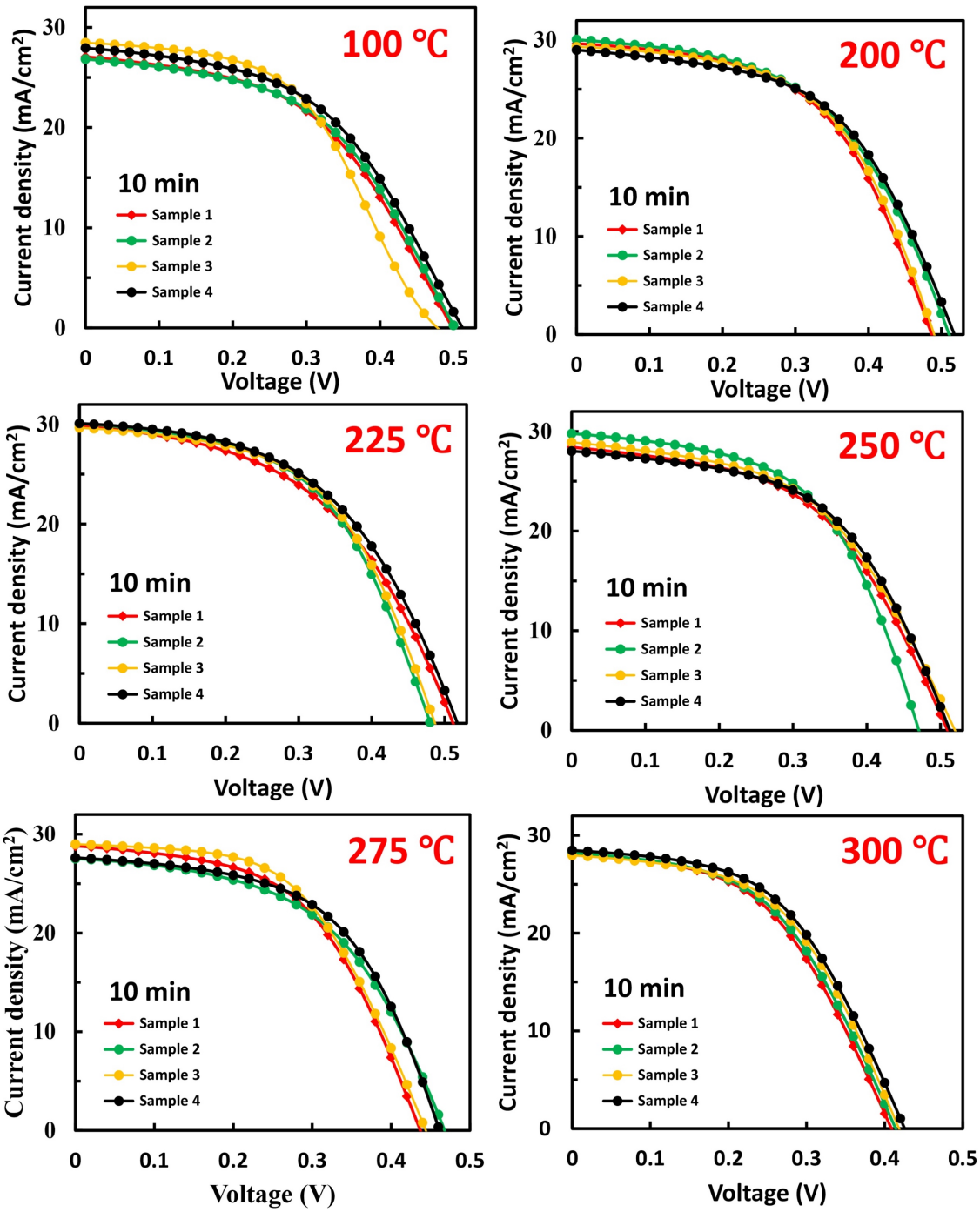

Fig. S4.8. ***J–V*** **curves of MoO_x–CNT/n-Si solar cells fabricated using the post-thermal annealed MoO_x-CNT/n-Si heterojunction at various temperature**

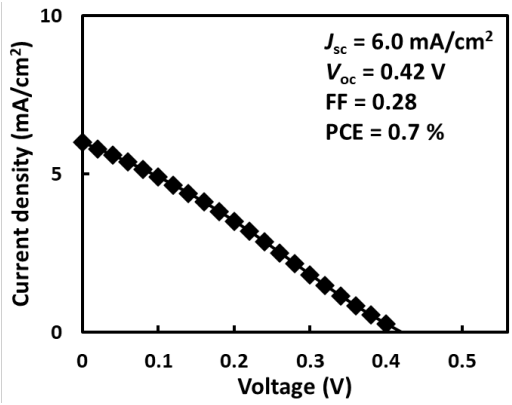

Fig. S4.9. *J–V* curve of the MoO_x/n-Si solar cell. The thickness of the MoO_x layer was ~30 nm. The MoO_x/n-Si solar cell was post-annealed under the optimum conditions of 20 vol% O_2/N_2 at 200 °C for 90 min.

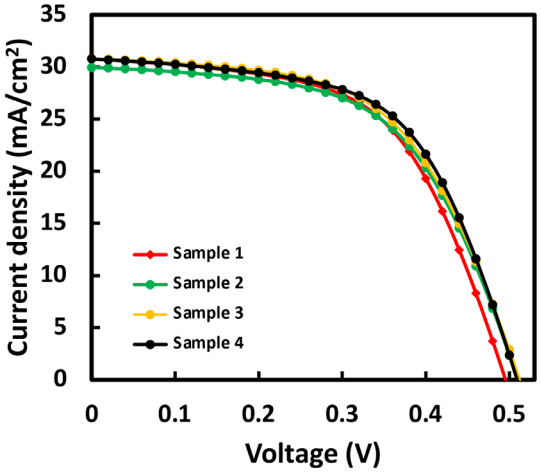

Fig. S4.10. *J–V* curves of the MoO_x–CNT/n-Si solar cells. Four solar cells were fabricated under identical conditions.

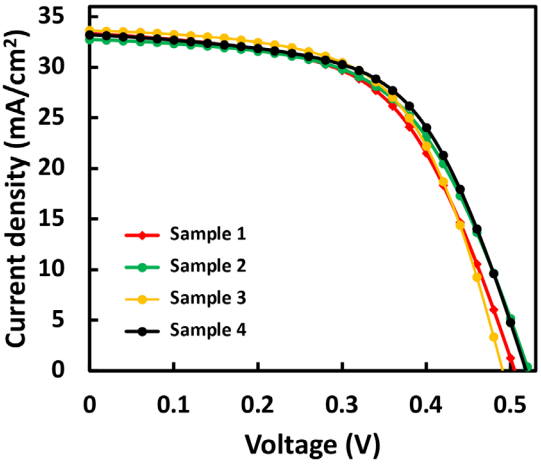

Fig. S4.11. *J–V* curves of the MoO_x–CNT/n-Si solar cells spin-coated with a 2 wt% PMMA solution. Four solar cells were fabricated under identical conditions.

References

[1] Li, F.; Zhou, Y.; Yang, Y.; Dong, G.; Zhou, Y.; Liu, F.; Yu, D., Silicon Heterojunction Solar Cells with MoOxHole-Selective Layer by Hot Wire Oxidation–Sublimation Deposition. *Solar RRL* **2020,** *4*, 1900514.

[2] Wang, F.; Kozawa, D.; Miyauchi, Y.; Hiraoka, K.; Mouri, S.; Ohno, Y.; Matsuda, K., Considerably improved photovoltaic performance of carbon nanotube-based solar cells using metal oxide layers. *Nat Commun* **2015,** *6*, 6305.

[3] Esconjauregui, S.; D'Arsie´, L.; Guo, Y.; Yang, J.; Sugime, H.; Caneva, S.; Cepek, C.; John R., Efficient Transfer Doping of Carbon Nanotube Forests by MoO_3. *ACS nano* **2015,** *9*, 10422–10430.

[4] Chastain, J.; King Jr, R. C., Handbook of X-ray photoelectron spectroscopy, Perkin-Elmer Corporation **1992,** 40, 221.

[5] Hellstrom, S. L.; Vosgueritchian, M.; Stoltenberg, R. M.; Irfan, I.; Hammock, M.; Wang, Y., Strong and stable doping of carbon nanotubes and graphene by MoO_x for transparent electrodes, *Nano Lett.* **2012**, 12, 3574–80.

[6] Han, B.; Gao, M.; Wan, Y.; Li, Y.; Song, W.; Ma, Z.; Effect of post-annealing on the properties of thermally evaporated molybdenum oxide films: Interdependence of work function and oxygen to molybdenum ratio, *Mater. Sci. Semicond. Process.* **2018,** 75, 166–172.

[7] Tune, D. D.; Flavel, B. S., Advances in Carbon Nanotube-Silicon Heterojunction Solar Cells. *Adv. Energy Mater.* **2018,** *8*, 1703241.

[8] Harris, J. M.; Semler, M. R.; May, S.; Fagan, J. A.; Hobbie, E. K., Nature of Record Efficiency Fluid-Processed Nanotube-Silicon Heterojunctions. *J Phys Chem C* **2015,** *119*, 10295–10303.

[9] Kim, H.; Ohkita, H.; Potential improvement in fill factor of lead-halide perovskite solar cells, *Solar RRL* **2017,** 1, 1700027.

[10] Yeganeh, M.A.; Rahmatollahpur, S. H.; Barrier height and ideality factor dependency on identically produced small Au/p-Si Schottky barrier diodes, *J. Semicond.* **2010,** 31, 074001.

[11] Cheung, S. K.; Cheung, N. W.; Extraction of Schottky diode parameters from forward current-voltage characteristics, *Appl. Phys. Lett.* **1986,** 49, 85–87.

[12] Franciosi, A.; Van de Walle, C. G.; Heterojunction band offset engineering, *Surf Sci Rep.* **1996,** 25, 1–140.

[13] Rakhshani, A. E.; Heterojunction properties of electrodeposited CdTe/CdS solar cells, *J. Appl. Phys.* **2001,** 90, 4265-–4271.

Chapter 5 Conclusions and Perspective

5.1 Comparison of the three processes for MoO_x deposition

The preparation methods strongly influence the structure of as-prepared MoO_x, and the structure factors can alter the chemical and electronic properties of MoO_x. Here, the three processes for the MoO_x deposition examined in Chapters 2–4 are compared and discussed in the viewpoints of the MoO_x structure, PV performance, and process/device scalability.

The XRD pattern of the MoO_x thin film prepared using the MoO_x precursor solution and that using the hot Mo wire showed only broad halo pattern, suggesting that the prepared MoO_x was amorphous (Fig. 5.1a, c). Weak crystal peaks appeared in the MoO_x thin film prepared by rapid vapor deposition using the pre-oxidized Mo boat (Fig. 5.1b). This is probably because the MoO_x thin film prepared by rapid vapor deposition led to partial crystallization of molybdenum oxide due to the radiation from the pre-oxidized Mo boat heated at 1200 °C. The Mo 3d core level XPS data presented only oxidation state for Mo of Mo^{6+} in the MoO_x layer prepared from the MoO_x precursor solution (Fig. 5.1d), but two oxidation states for Mo in the MoO_x layers prepared by the rapid vapor deposition of pre-oxidized Mo boat and the by hot-wire oxidation–sublimation deposition method (Fig. 5.1e,f). This is because the MoO_x as-deposited by rapid vapor deposition of pre-oxidized Mo boat and that by the hot-wire oxidation–sublimation deposition method contained the O vacancy.

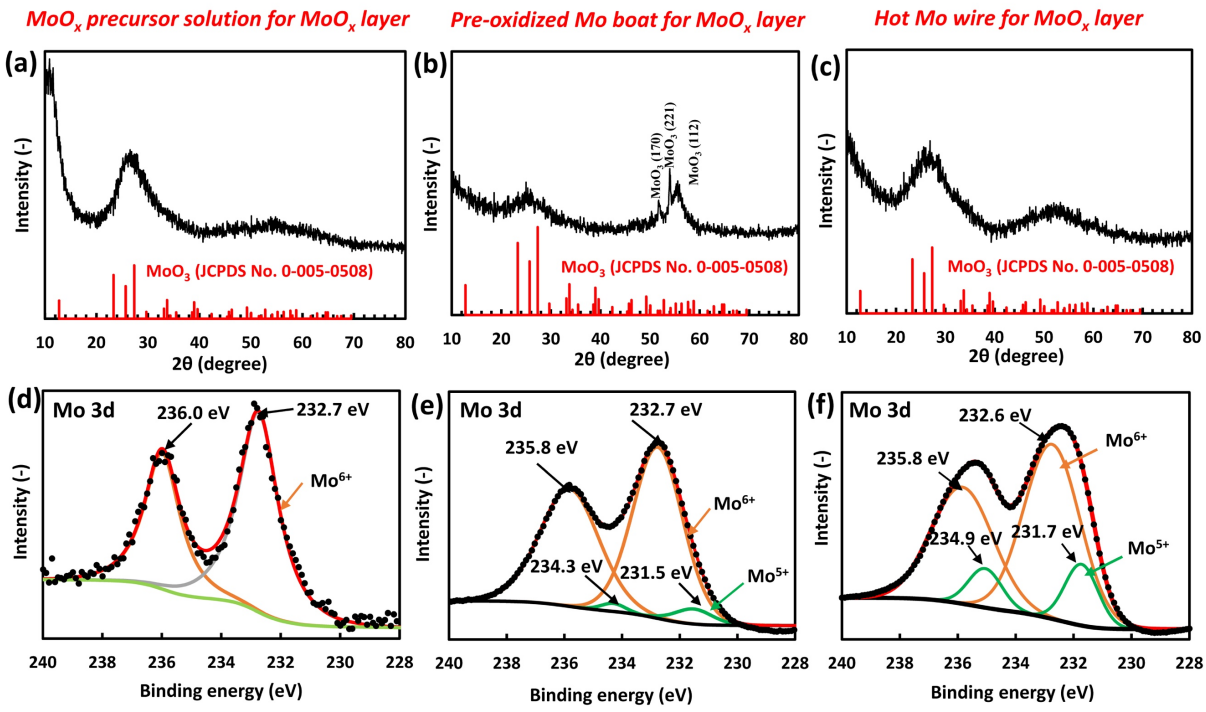

Fig. 5.1. X-ray diffraction (XRD) patterns and X-ray photoelectron spectroscopy (XPS) spectra of MoO_x layer on SiO_2/Si prepared by (a,d) spin-coating the 0.4 wt% MoO_x precursor solution, (b,e) rapid vapor deposition using the pre-oxidized Mo boat and (c,f) hot-wire oxidation–sublimation deposition method.

Then the PV performances of the MoO_x–CNT/n-Si solar cells were compared (Fig. 5.2). The device fabricated via the rapid vapor deposition method using the pre-oxidized Mo boat and that fabricated via the hot-wire oxidation–sublimation deposition method had similar PCEs of 11.3 % (red plots and lines) and 10.6% (green plots and lines), respectively. This is because the MoO_x layers prepared by these two methods had the similar crystal phase and the oxidation state for Mo (Fig. 5.1). The cells fabricating using the MoO_x precursor solution showed a relatively lower PCE of 10.1% owing to the lower J_{sc} values, probably due to the absence of the annealing process of the MoO_x layer. It is worth noting that the MoO_x–CNT/n-Si fabricated using the MoO_x precursor showed highest V_{oc} value. This is because the MoO_x layer prepared from MoO_x precursor has lower O vacancy, leading to lower recombination by defect.

Although all devices have almost similar PCE, dry process (hot-wire oxidation–sublimation deposition method) is better in the scalability for solar cells. Because the dry process can avoid the non-uniform distribution of MoO_x layer in large area CNT films that is caused in case of coating process of the MoO_x precursor solution due to the highly hydrophobic properties of the surface of the CNT films.

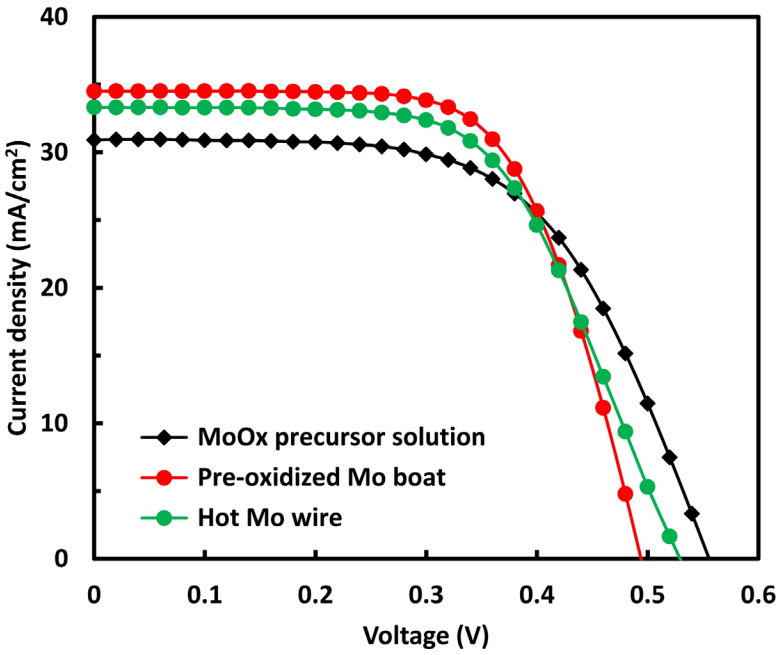

Fig. 5.2 *J–V* curves of the MoO_x–CNT/n-Si solar cells fabricated using the MoO_x layers prepared by the three different methods; spin-coating of the MoO_x precursor solution, the rapid vapor deposition method using the pre-oxidized Mo boat, and the hot-wire oxidation–sublimation deposition method.

5.2 Conclusions of the thesis

This study discussed the scale-up and performance enhancement of the CNT/n-Si heterojunction solar cell using the MoO_x layer. Three simple methods were adopted to prepare MoO_x layer for achieving this goal, including spin-coating of MoO_x precursor solution, rapid vapor deposition (<1 min) using pre-oxidized Mo boat, and hot-wire oxidation-sublimation deposition method.

Simple spin-coating of the MoO_x precursor solution for coating the cell with MoO_x significantly enhanced the efficiency and air stability of the CNT/n-Si solar cell (active area of 0.0314 cm^2). The MoO_x–CNT/n-Si solar cell with PCE of more than 10% was achieved, which is about 39% improvement compared with the pristine CNT/n-Si solar cell (7.2%). The cell with MoO_x coating showed a considerable air stability, maintaining its 80% of original PCE when it is exposed to air without any pretention layer for more than 1400 h. However, the PCE was poor for large-sized CNT/Si solar cell (active area of 4 cm^2) due to the non-uniform distribution MoO_x layer on the CNT film due to the poor wetting of the MoO_x precursor solution on the highly hydrophobic surface of the CNT films.

Rapid vapor deposition (<1 min) of MoO_x layer using pre-oxidized Mo boat onto the CNT film in the CNT/n-Si solar cells was developed, targeting more uniform MoO_x. This resulted in a PCE of 11.1% (active area: 0.0314 cm^2) and 3.6% (active area: 4.0 cm^2) by optimizing the experimental conditions. The rate of MoO_x deposition via rapid vapor deposition was analyzed and it was found that the whole evaporation process was too fast to make careful control over the MoO_x thickness in the batch process. But in future, this problem will be solved by integrating the rapid vapor deposition of MoO_x layer with roll-to-roll technology, where the MoO_x thickness will be accurately controlled by the sample carrying speed.

Then, a 4 cm^2-sized PMMA–MoO_x–CNT/n-Si solar cell with a PCE of 10.0% was realized via simple processes: the dispersion-filtration-transfer process for the CNT film, hot-wire oxidation-sublimation deposition for the MoO_x layer, mask-deposition for the Ag grid electrodes, and spin-coating for the PMMA anti-reflective layer.

Finally, I investigated the influence of MoO_x structure on PV performance of MoO_x–CNT/n-Si solar cells by varying the preparation methods of the MoO_x layer production. Although all devices have almost similar PCE, dry process (hot-wire oxidation–sublimation deposition method) is better in the scalability.

5.3 Perspective

A future goal will be the simple production of CNT/Si heterojunction flexible solar cells. As provided in Fig. 5.3, by integrating the rapid vapor deposition of 10 μm-thick crystalline Si film previously developed in our group with the dispersion-filtration-transfer process for the CNT film, hot-wire oxidation-sublimation deposition for the MoO_x layer, mark-deposition for the Ag grid electrodes, and spin-coating for the PMMA anti-reflective layer, high performance/cost ratio will be achieved with the MoO_x–CNT/n-Si heterojunction flexible solar cells.

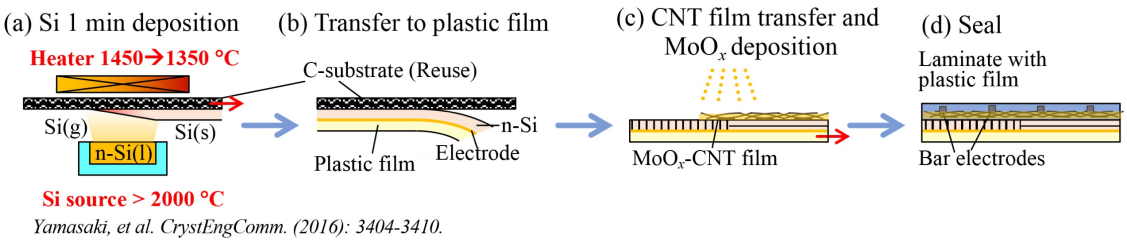

Fig. 5.3 Schematic of final research objective—large-sized MoO_x–CNT/Si flexible thin film solar cell

Copyright Permission

ELSEVIER

About Elsevier Products & Solutions Services Shop & Discc

Home > About > Policies > Copyright

Copyright

Overview Author rights Institution rights Government rights Find out more

Overview

In order for Elsevier to publish and disseminate research articles, we need certain publishing rights from authors, which are determined by a publishing agreement between the author and Elsevier.

For articles published open access, the authors license exclusive rights in their article to Elsevier.

For articles published under the subscription model, the authors transfer copyright to Elsevier.

Regardless of whether they choose to publish open access or subscription with Elsevier, authors have many of the same rights under our publishing agreement, which support their need to share, disseminate and maximize the impact of their research.

For open access articles, authors will also have additional rights, depending on the Creative Commons end user license that they select. This Creative Commons license sets out the rights that readers (as well as the authors) have to re-use and share the article: please see here for more information on how articles can be re-used and shared under these licenses.

This page aims to summarise authors' rights when publishing with Elsevier; these are explained in more detail in the ↓ publishing agreement between the author and Elsevier.

Irrespective of how an article is published, Elsevier is committed to protect and defend authors' works and their reputation. We take allegations of infringement, plagiarism, ethical disputes, and fraud very seriously.

Author rights

The below table explains the rights that authors have when they publish with Elsevier, for authors who choose to publish either open access or subscription. These apply to the corresponding author and all co-authors.

Author rights in Elsevier's proprietary journals	Published open access	Published subscription
Retain patent and trademark rights	√	√
Retain the rights to use their research data freely without any restriction	√	√
Receive proper attribution and credit for their published work	√	√
Re-use their own material in new works without permission or payment (with full acknowledgement of the original article): 1. Extend an article to book length 2. Include an article in a subsequent compilation of their own work 3. Re-use portions, excerpts, and their own figures or tables in other works.	√	√
Use and share their works for scholarly purposes (with full acknowledgement of the original article): 1. In their own classroom teaching. Electronic and physical distribution of copies is permitted 2. If an author is speaking at a conference, they can present the article and distribute copies to the attendees 3. Distribute the article, including by email, to their students and to research colleagues who they know for their personal use 4. Share and publicize the article via Share Links, which offers 50 days' free access for anyone, without signup or registration 5. Include in a thesis or dissertation (provided this is not published commercially) 6. Share copies of their article privately as part of an invitation-only work group on commercial sites with which the publisher has a hosting agreement	√	√
Publicly share the preprint on any website or repository at any time.	√	√
Publicly share the accepted manuscript on non-commercial sites	√	√ using a CC BY-NC-ND license and usually only after an embargo period (see Sharing Policy for more information)
Publicly share the final published article	√ in line with the author's choice of end user license	×
Retain copyright	√	×

Acknowledgements

Since coming to Waseda University in 2018 to pursue my doctor degree in Engineering. Prof. Suguru NODA has become my supervisor and I am so grateful to have him as my supervisor. I want to express my sincere gratitude to him for his guidance, useful advice and comments during my time here at Waseda University. What he said always encouraged me to continuedly pursue my career in research. I have learned and grown a lot from his guidance including the philosophy of the science, the ability to problems solving, logical thinking and careful working style in weekly group discussion. These qualities have been becoming a part of my life and will always benefit to me. I thank Mr. Emina Hara for help me use apparatus and make reservation for measurement in lab. I also really appreciate Dr. Hisashi Sugime, Dr Mochen Li and Dr. Rongbin Xie for their comments and discussion in my experiments and manuscript-writing. I thank Prof. Oyaiza's group at Waseda University for their support in the EQE measurement. I acknowledge Assistant Professor Nobuko Hanada, Dr. Heng Yi TEAH, Mr. Toshio Ohsawa, Mr. Tetsuro Sawada, Mr. Kotaro Yasui and Ms. Naoko Sato in the laboratory. I also want to express the appreciation for my family, my friends and the staffs in Waseda University for their supports to this research. Finally, I am grateful for the financial support from the China Scholarship Council (No. 201806380052).

List of research achievements

Paper

1. Xiaoxu Huang, Rongbin Xie, Hisashi Sugime, and Suguru Noda*, "Performance enhancement of carbon nanotube/silicon solar cell by solution processable MoO_x," Appl. Surf. Sci. 542, 148682 (2021).

2. Xiaoxu Huang, Emina Hara, Hisashi Sugime, and Suguru Noda*, "Carbon nanotube/silicon heterojunction solar cell with an active area of 4 cm^2 realized using a multifunctional MoO_x layer". Carbon, 185, 215–223 (2021).

Presentation

3. Xiaoxu Huang, Hisashi Sugime, and Suguru Noda*, "Performance enhancement of carbon nanotube/Si heterojunction solar cell by solution-processed MoO_3 layer," 18th Asian Pacific Confederation of Chemical Engineering Congress (APCChE 2019), PE322, Sapporo Convention Center, Sapporo, Japan, Sep. 25, 2019 (poster).

4. Xiaoxu Huang, Hisashi Sugime, and Suguru Noda*, "MoO_x layer with bar electrodes for enlarging active area and improving efficiency of carbon nanotube/n-Si heterojunction solar cells," 10th A3 Symposium on Emerging Materials: Nanomaterials for Electronics, Energy and Environment, P-16, Sungkyunkwan University, Korea, Oct. 27, 2019 (poster).